HOLOGRAPHY APPLICATION TO A GRATING X-RAY MASK

A thesis submitted to the Faculty of Engineering
at the University of Glasgow for
the degree of Doctor of
Philosophy
by

Remi, Henri, Marc DUMAS

November 1985

ACKNOWLEDGEMENTS.

I wish to express my gratitude to Professor J. LAMB for his encouragement to undertake a research work in his laboratories. The use of all the university facilities, academic support, technical assistance, computer access and recreational sport is greatly acknowledged.

I also wish to extend my thanks to my supervisor Professor P.J.R. LAYBOURN for he has always given good advice and been of great help whenever needed.

My warm appreciation also goes to Professor C.D.W. WILKINSON for numerous helpful conversations.

I am deeply indebted to my colleague Ray HUTCHINS for his moral support throughout my work and for his thorough advice on English literature as well as for numerous excellent criticism which allowed me to bring this thesis to its final version.

I would like to express my thanks to the technical team for constant help and availability with particular mention to M^{rs} Lois HOBBS, M^{r} George BOYLE, M^{r} Harry ANDERSON and M^{r} John CRIGHTON.

Many thanks are also due to my fellow research students for their concern about my well being and their assistance in everyday life.

My gratitude is also immense to all the members of GLASGOW UNIVERSITY Judo club who, under the aegis of M^{r} George McQUILLAN, helped me to harmonise my professional and social life.

C'est de plus un plaisir d'exprimer ma sincere reconnaissance a mes parents M^{r} and M^{me} BOISNON, ainsi qu'a mes freres et soeur,

Nathalie, Xavier et Thierry, pour leur soutien moral et leur frequentes visites.

A French scholarship, from the Centre National de la Recherche Scientifique, administrated by the Royal Society has been greatly appreciated.

TABLE OF PLATES

36: Micrograph of the 5 micron pinholes used with the 351.1 line.
37: Estimated light intensity profile after filtering.
38: View on the vacuum chuck holfer.
39: The front prism technique holder.
40: The holographic arrangement.
41: Computer simulation when Si_3N_4 thickness = 54.3 nm.
42: Computer simulation when Si_3N_4 thickness = 60.9 nm.
43: Computer simulation when Si_3N_4 thickness = 74.3 nm.
44: Typical geometry of an overexposed grating.
45: 0.3 micron grating micrograph.
46: The grooves are deeper but not cut down to the substrate.
47: Photoresist grating lines with undercut line profile.
48: The spaghetti-like effect on a 0.3 micron grating.
49: Exposure and development diagram.
50: Gold grating lines after lift-off.
51: Overview of a Au/Pd grating showing good uniformity.
52: Tunnelling effect after lift-off.
53: 0.29 micron grating.
54: Line profile showing overcut.
55: Computer simulation profile predicting an overcut.
56: 0.12 micron grating showing a patchy aspect and the spaghetti-like effect.
57: Geometry of gratings produced with the FPT and UV light.
58: 0.17 micron grating micrograph.
59: Moire pattern observed with FPT at normal incidence.
60: Fringes of equal thickness observed with a matching index fluid.
61: Protecting device for the metal grating during the window opening.

TABLE OF SYMBOLS

x, y, z	rectangular coordinates
θ	always denotes an angle
n	refractive indices
d	distance
ω	wave pulsation
β	spatial propagation constant
k	wave number
c	speed of light
E, H	scalar notation for electromagnetic field
E, u, r	vector notation
E, u, r	their corresponding modulus
λ	wavelength
ϱ	propagation constant in a continuum of modes
ϱ_{Nit}, ϱ_{Au}	density of nitride and gold respectively
μ	linear absorption coefficient
μ_m	linear absorption coefficient per unit mass
m	integer, mode number
$\varepsilon, \tilde{\varepsilon}$	dielectric constant
t	time
Λ	grating pitch
th	thickness
j	recurrence index
i	complex number such that $i^2=-1$
η	coupling coefficient between space harmonics
p	order of a Bragg interaction
o(x/z)	quantity of the 2^{nd} order in x/z where x/z<<1
l_j	thickness of layer j
J_o, J_1	Bessel functions
$\hat{}$	denotes a complex quantity
α	absorption coefficient
M	matrix of elements m_{ij}
u	undercut height
M(x,y)	remaining inhibitor fraction at coordinates x,y
I, I_o	luminous intensity
V_m	minimum accelerating voltage
K_α, K_β	lines in a X-ray spectrum

w_o, $w(x)$	waist of a laser beam at position 0 or x
R	radius of curvature of a spherical wave
r	radial coordinate
f	focal length
Ψ	amplitude ratio (ellipsometry)
Δ	phase difference (ellipsometry)
π	3.1415926.....
e	2.718.....

TABLE OF CONTENTS

PART II: THEORETICAL STUDY

PART III: EXPERIMENTAL WORK:

SUMMARY

This thesis reports the development of the holographic process towards the fabrication of a grating X-ray mask.

A general study is proposed which determines the design characteristics of a grating X-ray mask: a thin pattern of gold lines on a silicon nitride membrane. Such a mask can be used in contact X-ray lithography systems at the carbon K_α line.

The second part of the thesis deals with the theoretical aspects of the recording of holographic gratings in a layer of positive photoresist coating a silicon nitride/silicon substrate. A gaussian treatment of the holographic process is presented and shows that it is possible to dispense with the use of collimating lenses on the optical arrangement without noticeable contrast degradation.

A computer simulation of the grating recording process on multilayer substrates has been developed and was used to determine the thickness of silicon nitride for which the photoresist grating presents an undercut line profile, an indispensable feature before metal lift-off can be carried out successfully.

Finally the fabrication of gratings of various pitches was undertaken. 0.12 micron and 0.17 micron gratings were printed using the front prism technique with UV and blue light respectively. In some cases moire patterns were recorded and the gratings presented an overall patchy aspect and extended only over very small areas.

0.3 micron gratings were successfully fabricated and showed an undercut line profile as predicted by the computer simulation. A thin layer of gold or gold/palladium was evaporated under high vacuum and the grating pattern subsequently lifted-off by dissolution of the photoresist in acetone.

In some cases the lift-off was successful and gold gratings were obtained over large areas, But occasionaly the evaporated metal thickness was too high and a tunnelling effect was observed.

The fabrication of silicon nitride membranes was attempted but no reliable technique has yet been found of protecting the metal grating from the various etchants.

A discussion on the encountered difficulties is presented, solutions to these problems are suggested and a line of progress for future experiments is proposed.

GENERAL INTRODUCTION

Prompted by the discovery of the Laser in 1960 by T. MAIMAN, demonstrating a pulsed ruby laser, a new topic was to make the front line of progress. The INTEGRATED OPTICS sector, defined as the "control of light fluxes in optical waveguides and application of planar technology towards the creation of optical science and integrated optical and optoelectronics circuits" [Ref.1], has been rapidly expanding. Optoelectronics research alongside industrial production now encompasses many different branches such as: material study and fabrication, either for semiconductor applications or optical integration purposes; nonlinear optics, now very much in favour for its profusion of new applications (frequency doubling or tripling, phase conjugation mirrors, bistability etc...); and very high resolution patterning by electron beam lithography, photolithography, X-ray lithography, or holography.

A number of keywords can be heard or read here and there, E.Beam lithography, monolithic integration, active devices, modulation and coherent systems for example. Despite this great disparity of topics and areas of study, researchers across the world all reach towards the same ultimate goals:

-Make faster and smaller devices

-Integrate every module of one device on the same chip.

thus leading to the fabrication of INTEGRATED OPTICAL CIRCUITS [Ref.2,3] composed of lasers, modulators, passive devices such as filters, demultiplexers and others.

It was decided that research towards this trend, i.e. monolithic integration, should be undertaken. To be more specific, a reliable lithography procedure for the printing of laser structures onto a semiconductor chip without involving any destructive technique such as mirror cleaving was the object of the investigation. The fabrication of such monolithically

integrable lasers, distributed feedback (DFB) or distributed bragg reflector (DBR) lasers, where periodic patterns make the guiding layer a resonant structure [Ref.4], is now well established according to the extensive literature which can be found on the subject [Ref.5-9]. However the grating printing technique needs to be fast, reliable and cheap if the process is to be passed on to industry in the not so far distant future. At the present, Electron Beam lithography of such a structure is still in its infancy [Ref.10-12], and holography is the only acceptable alternative. The major problems encountered during the holographic printing of gratings are substrate dependence and poor repeatability. The answer to these problems has been to design and produce a grating mask which could be transferred onto substrates by X-ray lithography; the use of any optical wavelengths for the transfer would lead to noticeable diffraction and forbid proper replication of the mask. However, due to the inherent characterics of X-ray optics, X-ray lithography presents the property of not being substrate dependent.

The following thesis reports work on the design of the structure shown in figure 1. In order to achieve this aim, every single step of the process has to be mastered. Accordingly, the research undertaken includes:

-A general theoretical study in order to establish the mask characteristics (Part I).

-A detailed investigation of the holographic process followed by a computer simulation to improve the repeatability of the printing (Part II).

-Experimental work towards the fabrication of a grating X-ray mask (Part III).

The thesis will end by giving a layout for future experiments and suggestions for further improvement which could be added to the techniques described therein.

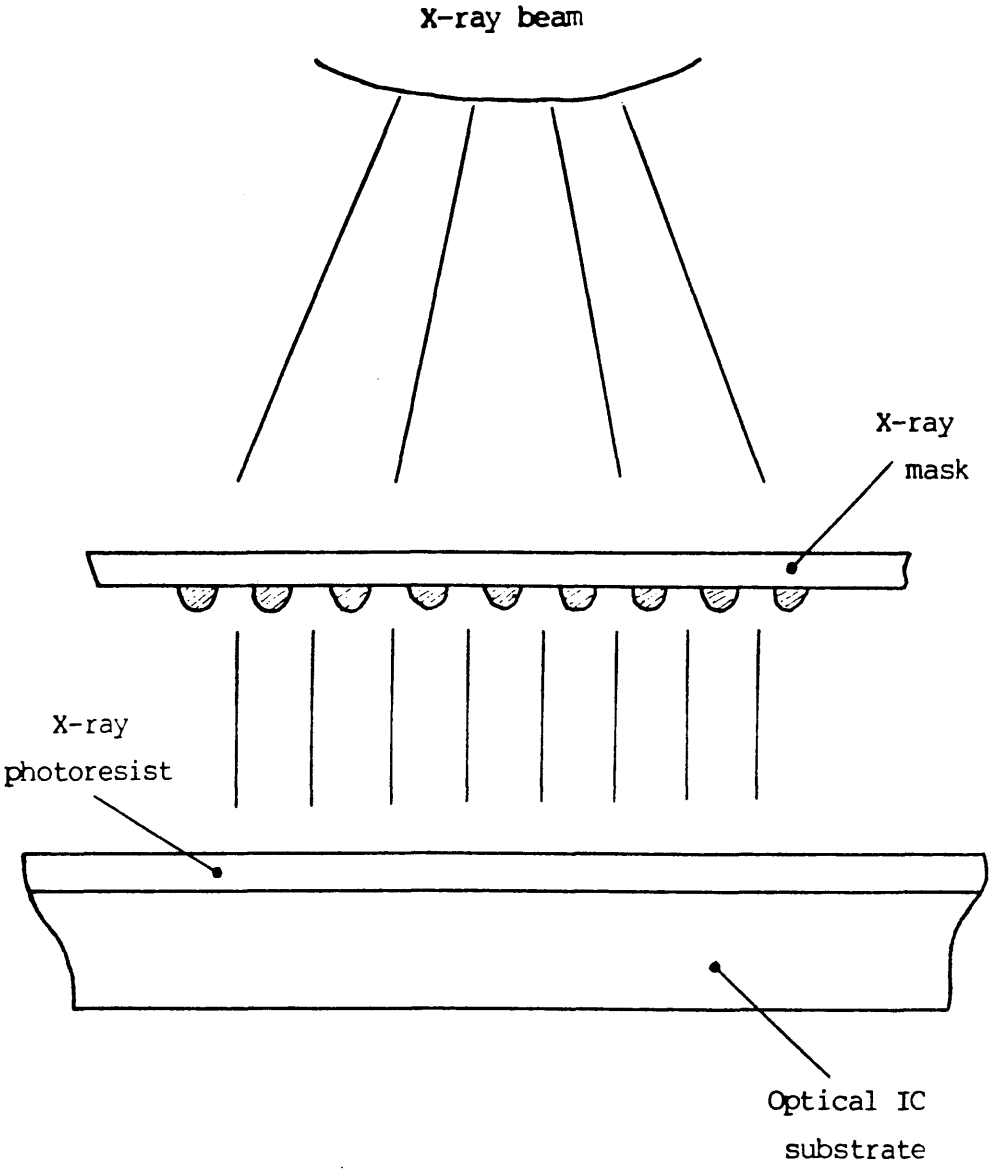

Figure 1: X-ray mask in its context.

Printing can be a step repeat process for industrial applications so that wafers of lasers could be produced rapidly.

PART I

GENERAL THEORETICAL BACKGROUND

Establishment of the mask characteristics.

INTRODUCTION

This part, "General theoretical background", leads to the characteristics of the grating structures involved in the process of integrated laser fabrication. It is divided into three sections.

-Section A deals with integrated optics theory, reviewing the guiding behaviour of a simple uniform waveguide structure, moving onto the description and modelling of grating interactions.

-Section B departs somewhat from the spirit of this part in that it is related to X-ray theory and generation, two topics of which a concise review is presented.

-Section C concludes this part by linking the two previous sections in order to, with the aid of relatively little data on today's optoelectronics trends , give the main design characteristics of a typical X-ray grating mask.

A: INTEGRATED OPTICS THEORY

The behaviour of uniform guiding structures is to be restated before the influence of grating patterns is described.

A.1) Uniform guiding structure:

The structure to be examined is shown in figure 2. For simplicity it is assumed that there is no dependence along the y-axis and, supposing the guiding film refractive index is higher than both the superstrate and the substrate indices, it is possible that an electromagnetic wave will be confined within the structure provided certain resonance conditions are satisfied.

It can be shown that any electromagnetic field in such a structure can be expressed as a linear expansion of two "modes":

-T.M. modes where the magnetic field H is transversal ($H_x=H_z=0$, $H=H_y$).

-and T.E. modes where the transversality applies to the electric field ($E_x=E_z=0$, $E=E_y$).

Once the wave equation in either the magnetic field (T.M. case) or the electric field (T.E. case) has been solved, the missing field can simply be derived from the known field using combined forms of MAXWELL's equations (Appendix 1).

The purpose of this section is to understand the phenomena occurring in grating interactions and not to develop the theory extensively , the T.E. assumption is taken for simplicity. This is not unreasonable however, since a fair number of the optical devices modelled, developed and produced to this day (particularly lasers) generally consider T.E. modes . Using this assumption, the following study only considers the electric field (E) equations.

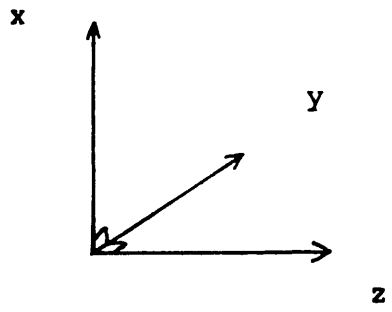

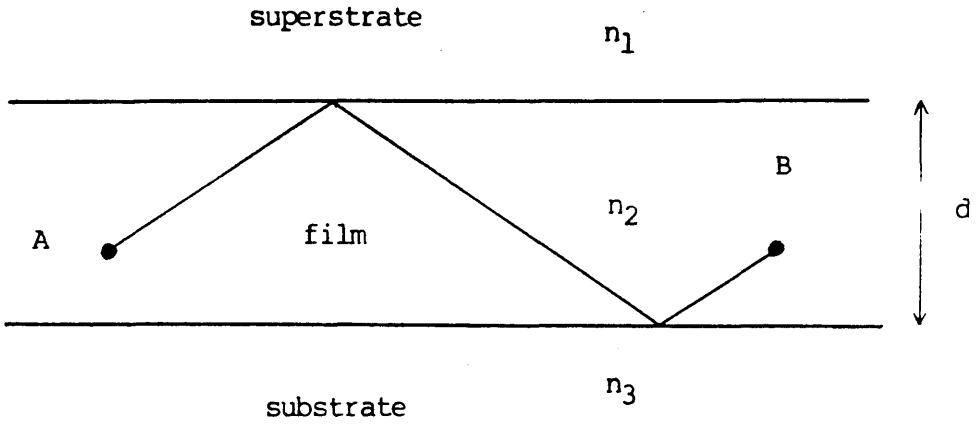

Figure 2: The uniform waveguide.

Using MAXWELL's laws, the following equation must be satisfied by the electric field (in a dielectric medium of index n, assuming a $e^{i\omega t}$ time dependence and a $e^{i\beta z}$ z dependence):

$$\partial^2/\partial x^2\, E + (k_0{}^2 n^2 - \beta^2)E = 0 \qquad (1)$$

where $k_o = \omega/c$.

In the case depicted in Figure 2, n can be either n_1, n_2 or n_3 leading to specific solutions for each layer. β is called the propagation constant of the electromagnetic wave along the z-axis. Depending on the sign of the quantity between brackets, either decaying or oscillating waves can take place within the considered layer. Plotting the quantity β versus k_o leads to dispersion diagrams as shown in figure 3. The guiding occurs with confinement of light in the "guiding layer" when β is within the shaded area, the wave decaying within substrate and superstrate whilst oscillating in the guiding film. If light is to be guided (β within the shaded area), it also has to comply with transverse resonance conditions (along the x-axis). This gives the guiding its discrete character and takes the form of a transcendental equation, called the mode equation, the eigenvalues of which depend upon the layers indices and thicknesses. The set of eigenvalues (β_j) gives a series of modes, represented by the A, B, C and D curves in figure 3. As an example, the ray approach to the resonance condition gives the following equation:

$$2m\pi = T1+T2+T3 \qquad (2)$$

with

$$T1 = 2d(k_0{}^2 n_2{}^2 - \beta^2)^{1/2} \qquad (2a)$$

$$T2 = 2\tan^{-1}\left[(\beta^2 - k_0{}^2 n_1{}^2)/(k_0{}^2 n_2{}^2 - \beta^2)\right]^{1/2} \qquad (2b)$$

$$T3 = 2\tan^{-1}\left[(\beta^2 - k_0{}^2 n_3{}^2)/(k_0{}^2 n_2{}^2 - \beta^2)\right]^{1/2} \qquad (2c)$$

This expresses the fact that, from point A to point B in Figure 2, the wave stays in phase, i.e. the optical path (T1) covered after two reflections, including phase shifts on the

A, B, C, D mode curves $\beta(k_0)$

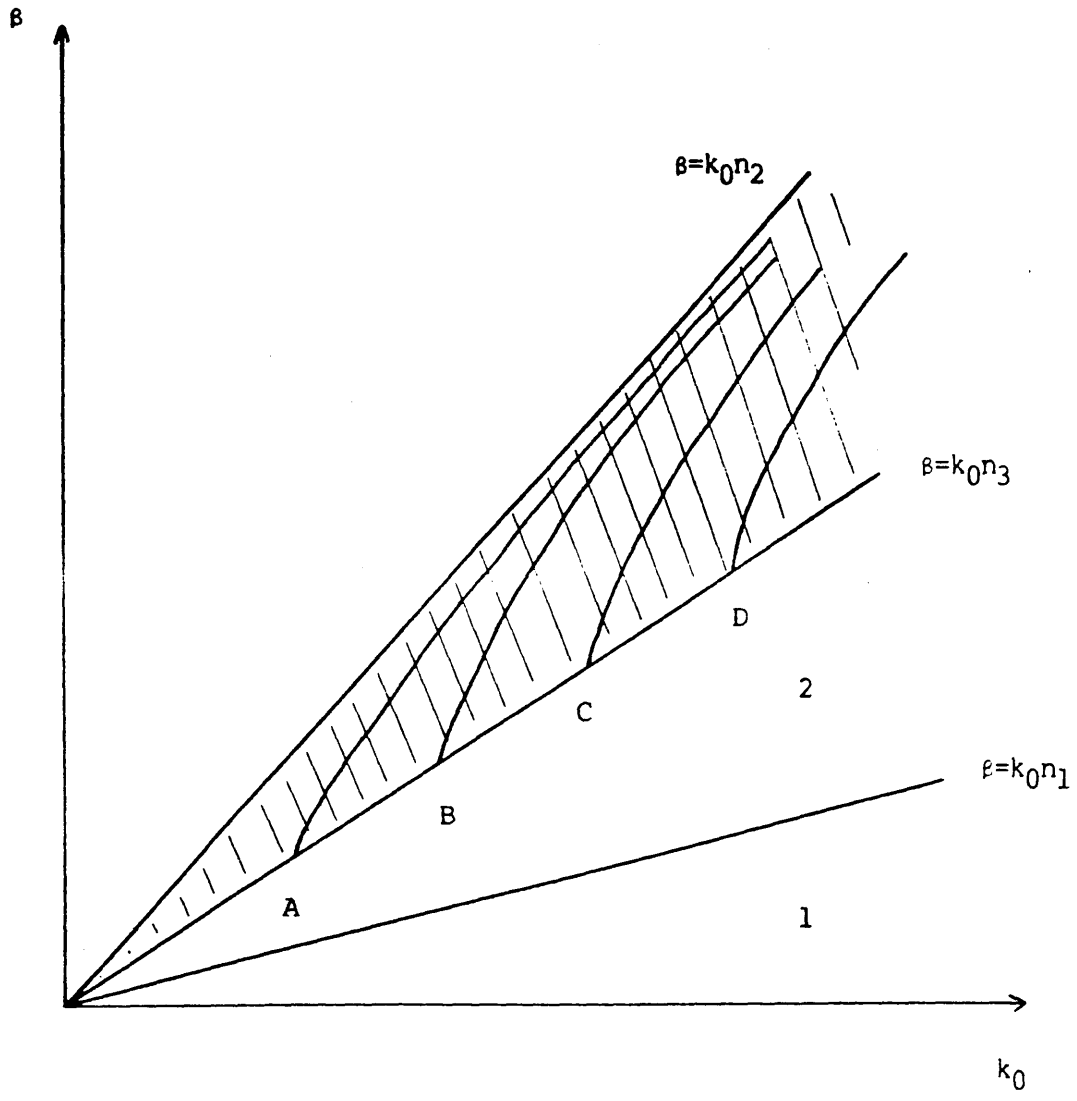

Figure 3: Dispersion diagram of a non symmetrical uniform waveguide.

superstrate (T2) and on the substrate (T3), is a multiple of 2π. For each value of m (mode number) there is a β-curve defined by equation (2) for that mode number.

In short, the properties of a uniform waveguide are as follows:

-The wave (E-field) satisfies a second order differential equation, derived from the more fundamental MAXWELL equations, in each layer of index n_j:

$$\partial^2/\partial x^2\, E + (k_0^2 n_j^2 - \beta_m^2)E = 0 \qquad (3)$$

-The propagation constant of the wave, β_m, is an eigenvalue of a transversal resonance condition giving a set of discrete guided modes $[\beta_m]$.

A closer look at the dispersion diagram shows, besides the existence of a set of discrete guided modes (E_m, β_m), the curves in the shaded area, a continuum of radiation modes, $(E(\rho),\rho)$, radiating in only one (area 2) or two layers (area 1). A uniform guiding structure can therefore be described as a system presenting a continuum of radiation modes and a set of discrete guided modes. All these modes, either from the continuum or from the discrete set, can be shown to be orthogonal with each other and form therefore a base for the E-field in the structure [Ref.13]:

$$E_{total} = \sum_n C_m(z) E_m + \int_0^\infty g(\rho,z)E(\rho)d\rho \qquad (4)$$

However, assuming there is no scattering from the interfaces and that the media are perfectly homogeneous, many modes (discrete or continuous) might coexist but will stay independent and are not coupled to each other [Ref.13].

A.2) Grating structure:

The need has arisen to provide coupling between the modes of the uniform waveguide. Whereas in a coupler one might want to couple a radiating mode from the continuum to a guided mode [Ref.14-18], coupling between forward and reverse guided modes is highly desirable in a laser [Ref.4,6,7,19]. As was pointed out earlier, the modes of a uniform waveguide form an orthogonal base for the electric field (equation 4); a change in the dielectric constant introduced by imperfections on the interfaces will give rise to additional source terms in the differential equation in E [Ref.13]. Due to these extra terms, the waveguide modes will be perturbed, they will not obey the original equation and will exchange energy as they propagate. If the change in dielectric constant consists of random imperfections on the interfaces, the guided modes will be slightly coupled to the radiating modes and the waveguide will leak. This scattering process can be put to use and made constructive by ordering the imperfections in a grating structure, and the differential equation to be satisfied by the electric field is:

$$\left(\partial^2/\partial x^2 + \partial^2/\partial z^2 + k_0^2 n^2(x,z) \right) E = 0 \qquad (5)$$

where the grating character appears in the geometrical dependence of the refractive index n(x,z). Two types of gratings are considered, the corrugated grating where the index dependence is in x and z and the phase grating where the index changes only along the propagation axis (z-axis). Both cases have been examined [Ref.13,17,20-25] and lead to the same type of phenomena. For simplicity, only the phase grating case is examined because the dielectric constant depends only on z (which means that the continuity of the electric field at the interfaces still leads to simple conditions).

The dielectric constant takes the form:

$$\varepsilon(z) = n^2(z) = \bar{\varepsilon}\left(1 - M\cos(2\pi z/\Lambda) \right) \qquad (6)$$

where Λ is the grating pitch.

coefficient of E in equation (5) depends upon z, the
can be written as follows:

$$\ldots)\exp(ik_t x) \qquad (7)$$

then easy to separate the variables and to obtain an
in $Z(k_t,z)$ called the MATTHIEU equation [Ref.24]:

$$\left[\ldots - (k_u\Lambda/\pi)^2 - 2q\cos(2z')\right] Z(k_t,z) = 0 \qquad (8)$$

$$\ldots - k_t^2 \qquad (8a) \qquad q = M(k_0 n\Lambda/\pi)^2/2 \qquad (8b)$$

$$\ldots \qquad (8c) \qquad x' = \pi x/\Lambda \qquad (8d)$$

The solutions of such an equation are usually written in the
form [Ref.24]:

$$\ldots z = P(k_t,z)\exp(i\beta z) \qquad (9)$$

where β is the longitudinal wave-number, characterising the
propagation along the z-axis, k_t is the transversal wave-number,
related to the propagation along x, and $P(k_t,z)$ is a function
periodic in z of periodicity Λ.

As $P(k_t,z)$ is periodic in z, it can be expanded in a Fourier
series:

$$P(k_t,z) = \sum_{-\infty}^{+\infty} {}_p a_p(k_t)\exp(2i\pi pz/\Lambda) \qquad (10)$$

where $a_p(k_t)$, the Fourier amplitudes are only functions of (k_t).

$$\beta_B = -\beta_A = \beta \qquad (13)$$

Equation (12) becomes the well-known Bragg equation:

$$\beta = \pi p/\Lambda \qquad \text{or} \qquad \Lambda = \pi p/\beta \qquad (14)$$

where p is the Bragg order of the interaction.

By solving the wave equation, numerically or analytically, an indication of the strength of the coupling between reverse and forward waves can be obtained. Rigorous calculations [Ref.20,22,23], perturbation techniques [Ref.17,32-34], or coupled mode theory [Ref.4,28] can be used by themselves or in combinations [Ref.34] and they all lead to results predicting the same phenomenological behaviour. D.L. JAGGAR [Ref.31] gives a particularly good intuitive view of what happens during Bragg interactions. Assuming that a phase grating acts as a small sinusoidal perturbation, the coupling coefficients between reverse and forward waves are derived at different Bragg orders. The original wave is scattered into the next two space harmonics $\pm 2\pi/\Lambda$, those space harmonics in turn scatter into their next opposite neighbours. If the coupling coefficient between two neighbouring space harmonics is η, after p scattering interactions the wave β is seen to have coupled some energy into the spatial harmonic $\beta - 2\pi p/\Lambda$ which is supposedly matching the reverse wave $-\beta$. It should be noted that such an interaction is proportional to η^p showing that high order Bragg coupling is less efficient and prone to more losses, due to several scattering processes, than the lower order coupling.

A.4) Qualitative study:

The effects described can be called p^{th} order Bragg interaction and only sinusoidal gratings were considered. Clarification needs to be made on what is commonly called a second or third order grating. An p^{th} order grating is a periodic structure presenting a pitch Λ satisfying equation (14). The following notation will be used hereafter. Λ or Λ_1 is used to denote the pitch of a first order grating (when p=1 pitch=π/β)

and Λ_p the pitch of a p^{th} order grating (when pitch=p*Λ). Assuming a grating (Λ_p) to have a sinusoidal profile, a constructive energy transfer between forward and reverse wave occurs by way of an p^{th} order Bragg interaction. However, if the grating presents any non-sinusoidal profile at all, another phenomenon occurs. The grating can , being of periodicity (Λ_p) be expressed as a superposition of sinusoidal sub-gratings ($\Lambda_{p/m}$) according to Fourier's theorem, the fourier components of each sub-grating depending on the grating shape. Take for example a fourth order grating, constructive interactions will arise between forward and reverse waves as follows:

4^{th} order Bragg interaction by Λ_4

2^{nd} order Bragg interaction by $\Lambda_{4/2}$

1^{st} order Bragg interaction by $\Lambda_{4/4}$

Assuming that a_1, a_2, a_4, are the Fourier components for the three sinusoidal gratings (Λ_1, Λ_2, Λ_4), the interaction from Λ_4 will be of the order of $a_4\eta^4$, from Λ_2 will be $a_2\eta^2$ and $a_1\eta$ for Λ_1. It must be born in mind that the three interactions may not add constructively but may well partially cancel.

A.5) Conclusion:

In conclusion, it appears that, qualitatively, research should be aimed towards the making of low order gratings of shapes presenting a high fourier component in the first Bragg order and ultimately towards the production of first order sinusoidal gratings, thus minimising scattering losses and making the coupling between reverse and forward waves more efficient allowing for smaller devices (the product "length of interaction by coupling coefficient" is important in the design of an integrated laser, a greater coupling coefficient allows for a shorter interaction [Ref.2,7]). The choice of the grating parameters for which fabrication was undertaken will be further defined at the end of this part. The first line of design is to produce first or second order gratings.

B: X-RAY LITHOGRAPHY

This section does not present a detailed study of X-ray lithography. Its purpose is to remind the reader of a few properties of X-rays which will be put to use in the determination of the absorbing characteristics of a grating mask to be transferred by X-ray lithography. The section starts with comments on X-ray physical properties, follows on with their generation and their limitations and concludes with guidelines for the fabrication of an X-ray mask.

B.1) Physical properties:

X-rays are electromagnetic waves of very short wavelengths ranging from tenths of angstroms (hard rays) to tens of angstroms (soft rays). Their electromagnetic properties differ somewhat from those of optical waves as the refractive indices at X-ray wavelengths are slightly less (about 10^{-4}) than unity. This results in very low reflections unless the X-ray incidence is very close to grazing angles so that the critical angle for total reflection can be reached. Because of their wavelength being of the order of interatomic dimensions, X-rays also interact strongly with crystals and scattering from every crystallographic site adds constructively due to their periodic arrangement. Thus crystallographic data can be found which in itself represents a whole field of research. Apart from the above case, the main property of X-rays lie in their ability to be absorbed by most materials.

B.1.1. Absorption law:

The X-ray absorption law takes the form of Beer-Lambert law, [Ref.35], and permits the determination of the adequate thickness of absorbing material to be lifted-off on the X-ray masks:

$$I = I_0 \exp(-\mu t) \qquad (15)$$

where I_0 is the initial intensity, t the material thickness and μ the linear absorption coefficient. The constant μ

characterises the absorption, only depending on Z the atomic number of the absorbing elements in the material, and on λ, the X-ray wavelength. The literature on X-ray physics offers a good range of tables giving the mass absorption coefficients for many elements at different wavelengths [Ref.35-40].

B.1.2. Half-value thickness:

A useful parameter is the half-value thickness $th_{1/2}$, thickness of a layer of material such that the incident X-ray intensity is halved during propagation through the medium. This parameter is linked to the linear absorption coefficient by a simple relation derived from Beer-Lambert law:

$$th_{1/2} = Ln(2)/\mu \qquad (16)$$

In order to have an idea of how fast X-rays are attenuated it is worth remembering that the half-value thickness is less than 10 microns if λ is more than 6 angstroms for every element of atomic weight higher than 12.

B.1.3 Absorption spectrum:

It is important to briefly describe the X-ray absorption behaviour of most materials and figure 5 is a typical presentation of X-ray absorption characteristics, where the absorption coefficient μ is plotted against the wavelength λ. A very important feature of X-ray absorption is the existence of absorption edges, characteristic to the material, where absorption drops sharply. X-ray wavelengths slightly higher than the edge wavelength are less absorbed than the smaller wavelengths, the material behaves as a high pass filter and such a property is put to use in filtering foils for X-ray sources when a relative degree of monochromatisation is desired.

B.2) X-ray generation:

X-rays can be generated by fast deceleration of electrons in an element in which the atomic structure determines the emitted spectrum. This phenomenon is put to use in X-ray lithography systems which involve the contact printing method. However it is

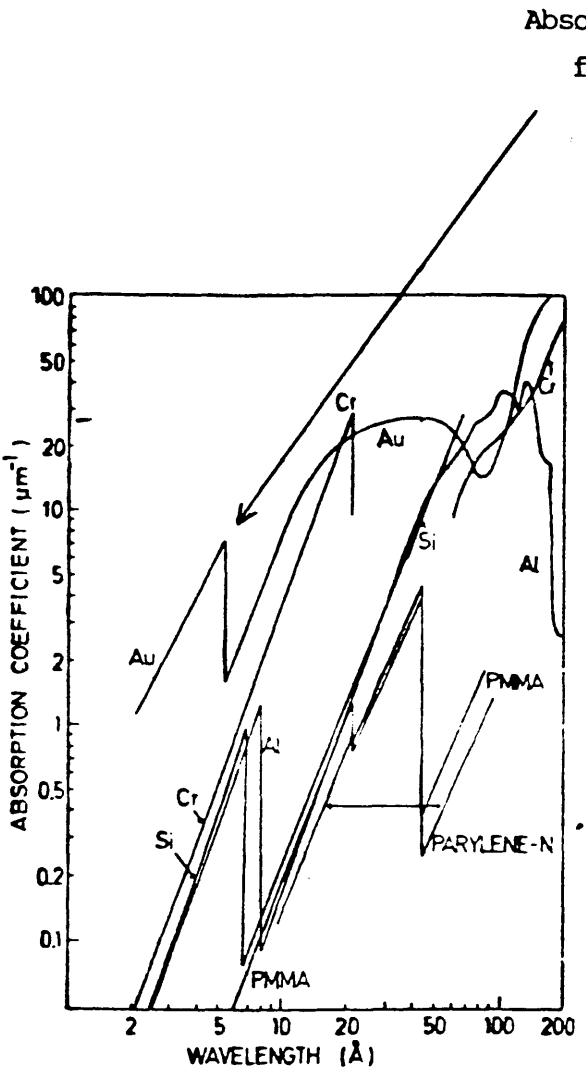

Figure 5: Absorption spectrum of various materials. [Ref.41]

desirable to use projection printing rather than contact printing (where the mask and substrate are no longer in contact) in order to extend the mask's lifetime. Such a system makes use of the fact that in a synchrotron a broad range of wavelengths (from microwaves to hard X-rays) is produced [Ref.42,43]. Before the two above systems are described in more detail, mention must be made of other devices which utilise the property of hot and dense plasmas to emit X-rays. Such plasmas can be induced by high-energy laser pulses focussed onto solid targets [Ref.45,46], or by energetic fast discharges under vacuum [Ref.44]. Although commercial versions of the earliest X-ray lithography systems (contact printing) are available, the setting up of such systems is very much part of a research project and is often a do-it-yourself adventure.

B.2.1 Contact printing systems:

Contact printing is by far the most popular due to its low price and easy set-up. The X-ray generator usually consists of an electron gun operating at an accelerating voltage about two to three times higher than the minimum voltage V_m required to produce photons of wavelength λ. V_m and λ are connected by the PLANCK's relation and, using kV and angstroms as units, one obtains the following formula for V_m:

$$V_m = 12.4/\lambda \qquad (17)$$

Once generated, the electron beam is focussed onto a target. The intensity of the electron beam will determine the intensity of the X-ray beam while the focal spot size will determine the area of the X-ray source. The material composing the target determines the emitted X-rays, [Ref.47-50], according to its emission spectrum, an example of which is given in figure 6. Two features can be observed; a continuous background spectrum of X-rays produced by bremsstrahlung effect and a discrete spectrum of lines characteristic to the target material. In theory one could choose the target material according to the desired wavelength, adjust the focus to be as strong as possible in order to make the source point-like and drive the electron gun at maximum intensity

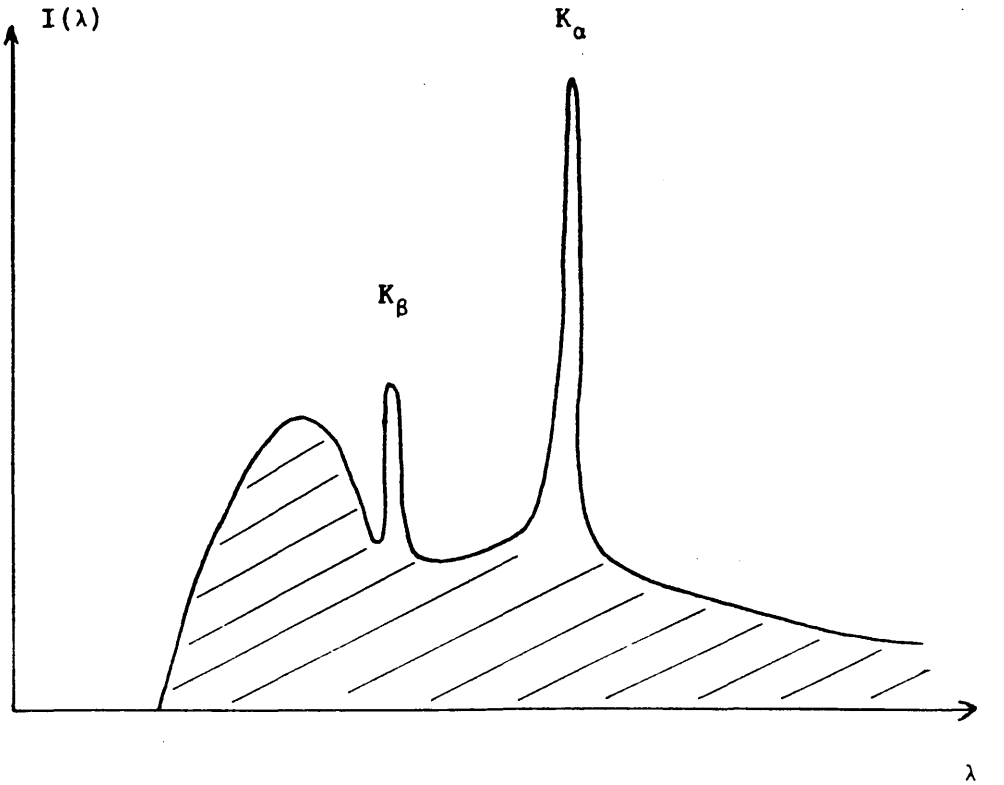

K_α and K_β are two of the characteristic lines of the material and the shaded area is the continuous spectrum.

Figure 6: X-ray emission spectrum by electron bombardment.

for a brighter source. However limitations are introduced by the target. For a fixed target the limitation is set by the fusion point of the material and cooling systems are carefully designed to keep the target temperature down [Ref.51]. In order to overcome the danger of melting the target at the focal point, rotating targets have been developed [Ref.52]. Again, limitations occur, due to the mechanical strains induced by the centrifugal force and the induced temperature gradient [Ref.52]. The X-ray beam is usually filtered by thin foils with adequate absorbing properties to reduce its bandwidth.

Figure 7 shows the contact printing set-up. As represented, the geometrical factors introduce limitations on the best resolution that can be obtained by contact X-ray printing systems. Three types of distortion occur as outlined in figure 7, these are the penumbrial distortion, due to the finite size of the source, the offset distortion, due to the thickness of the photoresist coating on the substrate, and the pattern shift due to the distance from mask to object. As an example, for a pattern size of 2 mm radius, a source size of 1 mm diameter and a distance source-mask of 300 mm, a resolution better than 0.01 micron requires the mask-object distance to be less than 3 microns and the resist thickness not greater than 2.5 microns. The pattern shift will then reach a value of 0.02 microns at the edges of the pattern. One will therefore have to half the mask-object distance and the resist thickness to obtain the desired resolution. Another way of reaching the same resolution is to double the mask to source distance. However the X-ray intensity will then be divided by a factor of 4 leading to very long exposure times, leaving more chance for the transfer to be affected by vibrations. It is obvious that a compromise has to found.

The limitations on the contact printing system led researchers to look for a system with reduced source size, with an increased source-mask distance (meters) and high intensity X-ray beams to keep exposure times low (seconds or less). Hence the projection printing systems were developed [Ref.41-43,53,54].

B.2.2. Projection printing systems:

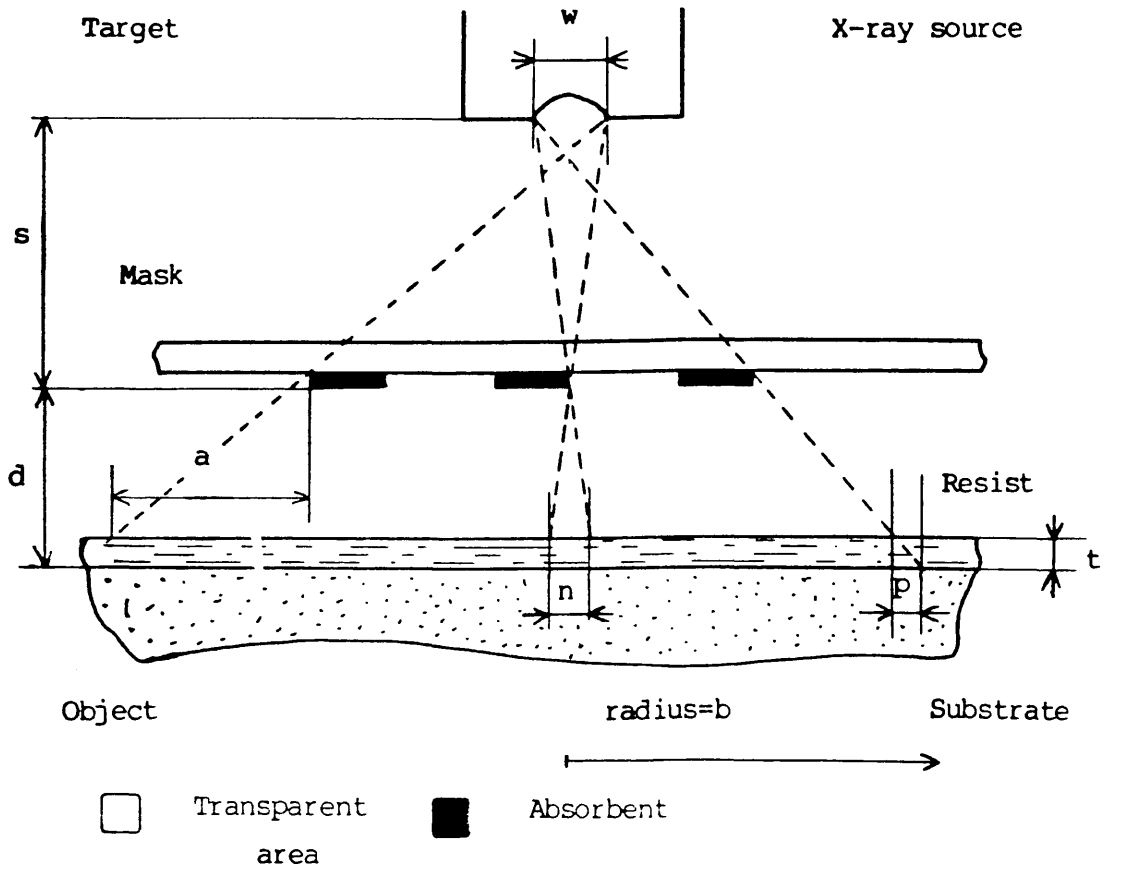

n penumbrial distortion (extended source): $n=w*d/s$

p offset distortion (resist thickness): $p_{max}=b*t/(s+d)$

a pattern shift (mask-object distance): $a_{max}=d*b/(s+d)$

Figure 7: The three types of distortions in contact printing systems.

The generator in such systems is usually a synchrotron. A wide range of X-ray wavelengths is emitted, from hard to soft rays, in a well-collimated beam. Wavelength selection can be arranged in the usual manner by gold mirrors, curved crystals or filtering foils. The resolution can be made very good with still manageable distances between mask and substrate (cms) [Ref.41,43]. Despite their size and their very high cost [Ref.41], and because they offer reliability [Ref.54], such systems are therefore very promising for industrial production. Many studies have been carried out on the feasibility of projection printing systems [Ref.41,43,54]. There are some in use, for example in JAPAN [REf.41] and GERMANY [Ref.43].

B.3) Conclusion:

At GLASGOW UNIVERSITY a contact printing system is available for use and although a projection printing system would be desirable, the design of X-ray masks has been governed by the limitations of a contact printing set-up so that the samples produced could eventually be tested. The design was settled along the following guidelines:

-The target material and the mask absorbent was chosen so as to match their respective emission or absorption characteristics, thereby minimising the absorbent thickness and allowing for a decent mask contrast.

-The mask must be mechanically strong in order to sustain repeated use and intimate contact with the substrate. This means that the absorbing pattern must be particularly well protected.

C: X-RAY MASK CHARACTERISTICS

Based on the principle laid down in the previous sections, the X-ray masks characteristics will be chosen. The characteristics are divided into three distinct parts. They are:

-The general design.

-Materials choice.

-Geometrical parameters.

C.1) General design:

The basic scheme of an X-ray mask is shown in figure 8. Following hints and suggestions from the literature [Ref.55-59], an improved design has been brought about. The mask consists of the following parts:

-Supporting material.

-X-ray transparent membrane.

-Absorbent pattern.

-Protective layer.

and is fabricated along the following steps:

-Cleaning procedure.

-Photoresist coating.

-Resist patterning.

-Metal lift-off.

-Window opening.

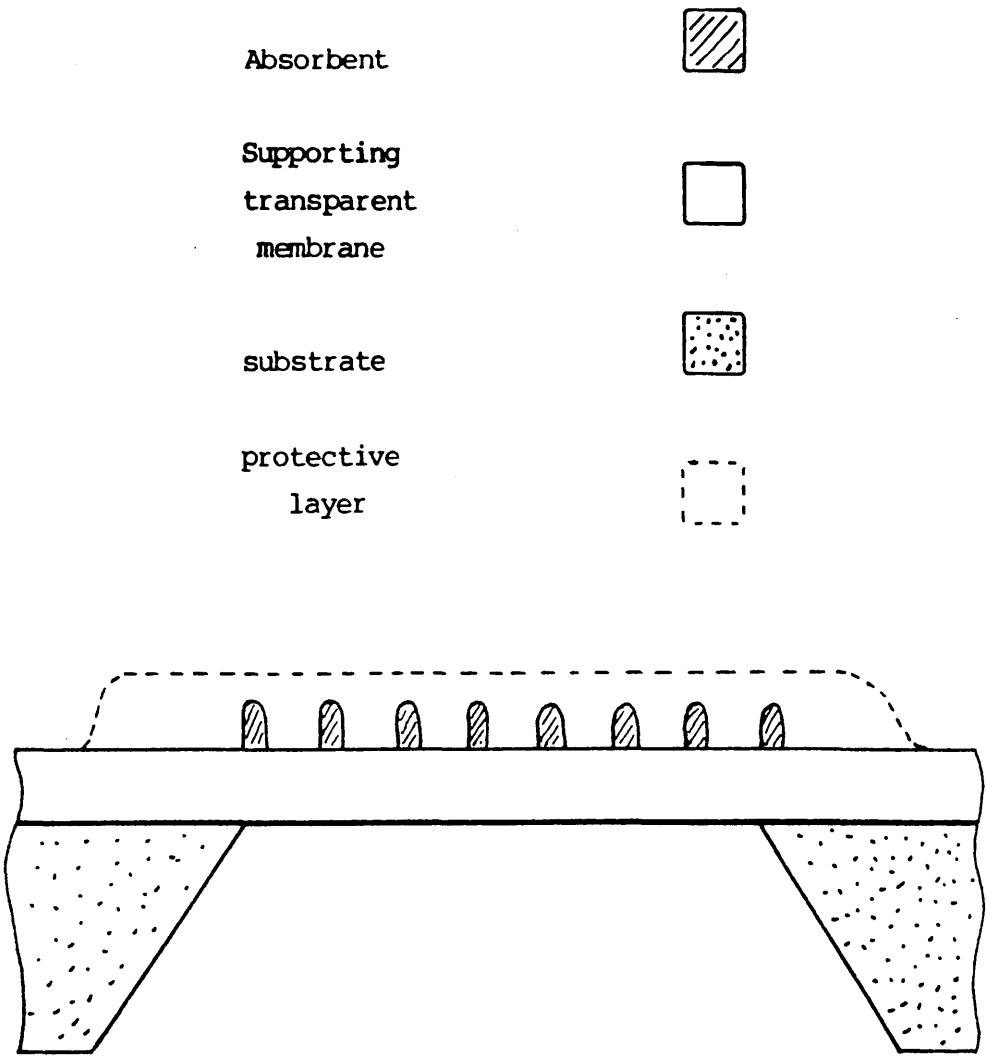

Figure 8: A typical X-ray mask.

-Protective layer deposition.

as shown in figure 9.

C.2) Choice of materials:

For the supporting material and the membrane, a silicon wafer coated with a silicon nitride layer was chosen. This choice is justified by the fact that silicon technology is now so well established and that the growing of layers such as silicon oxide or silicon nitride is now done as a matter of routine with exceedingly good reliability (C.V.D., M.B.E. and others). Moreover, silicon nitride membrane fabrication (excluding the growing procedure) is now a routine procedure [Ref.60] and it is rather fortunate that they are relatively transparent to X-rays. Concerning the absorbing material, a dense element is required (leading to strong X-ray absorption) which must be easy to lift-off (Figure 9c-d). For this purpose gold is very suitable and is often used in X-ray lithography. From tables provided by [Ref.37], calculated half-value lengths for gold and silicon nitride have been plotted versus wavelength (figure 10). Figure 11 presents theoretical values (derived from figure 10 results) for the contrast of a 100 nm thick gold-absorber mask at different wavelengths. For the best possible contrast the plot indicates a theoretical best value of 30 angstroms for X-ray wavelength. Unfortunately the choice is limited by the existence of materials emitting in this area of the spectrum. There only are two target materials available, either copper (1.34 nm) or carbon (4.48 nm) [Ref.54]. It was decided to use the K_α carbon line so that the contrast is fairly high allowing thin layers of gold to be used (around 100 nm) [Ref.61-63]. Moreover, the X-ray radiation will be well absorbed by the X-ray resist [Ref.53,64,65] on the substrate, due to the long wavelength of the X-rays, thus the thin layers of resist would minimise the offset distortion as described previously. The only drawback of such a choice, i.e. soft X-rays, is that they will be noticeably absorbed in the silicon nitride membrane which will result in fairly long exposure times. It must be noted that absorption in the membrane has no effect on the mask contrast which only

a) Cleaning and resist coating of the substrate.

b) Photoresist grating fabrication.

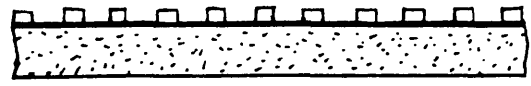

c) Absorbent material evaporation.

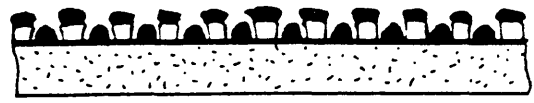

d) Removal of the photoresist (lift-off).

e) Opening of the back window.

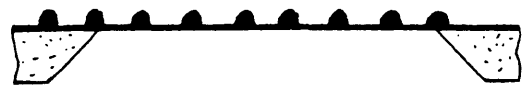

f) Deposition of a protective layer.

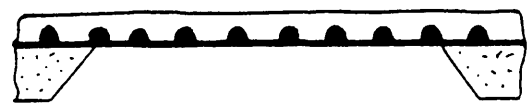

Figure 9: The six fabrication steps involved in the production of an X-ray mask.

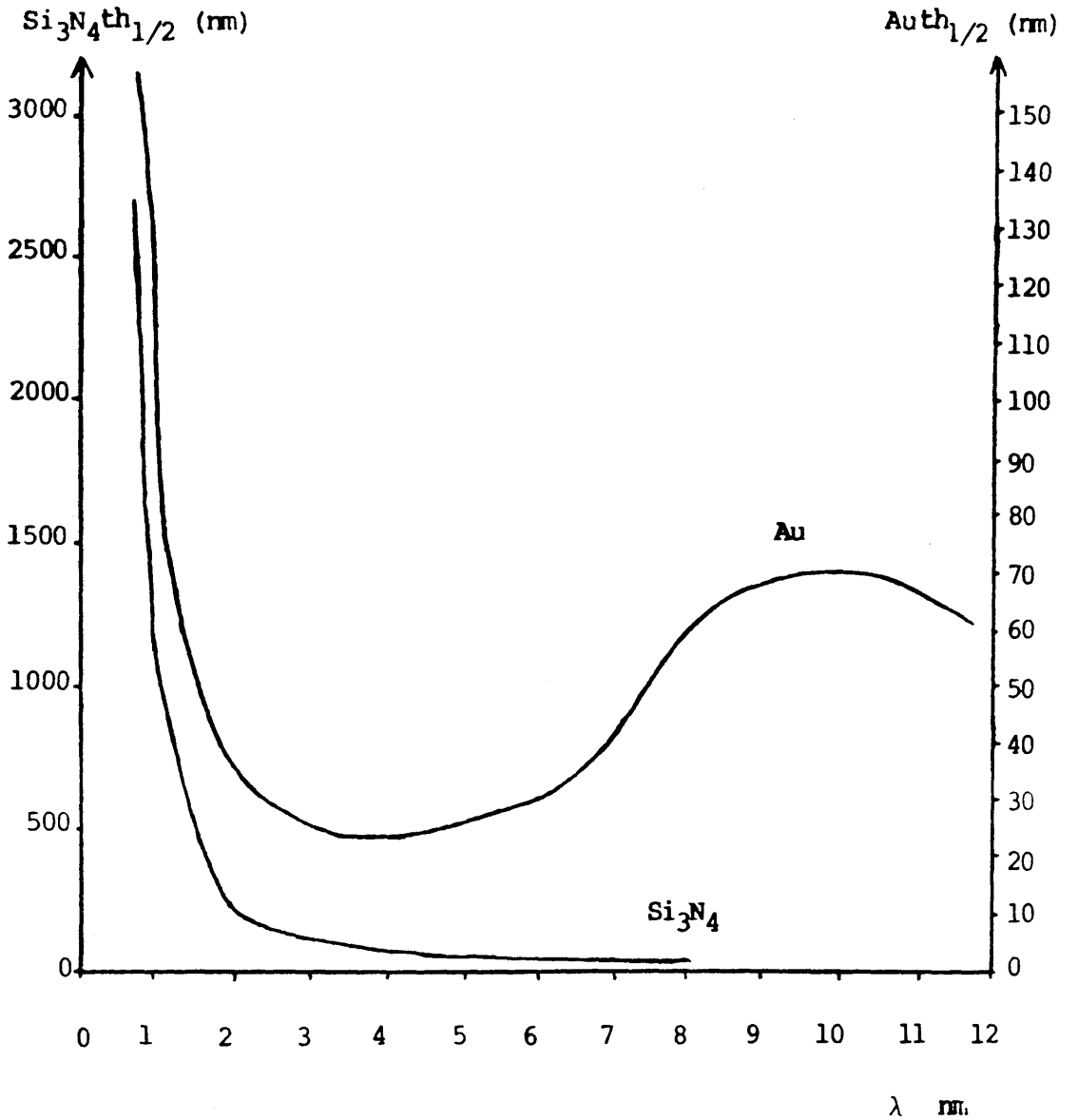

$\rho_{nit} = 3.44\ g/cm^3$ $\rho_{Au} = 19.3\ g/cm^3$ [Ref.66]

$th_{1/2}^{nit} = Ln(2)/\mu_m^{nit}\rho_{nit}$ $th_{1/2}^{Au} = Ln(2)/\mu_m^{Au}\rho_{Au}$

$$\mu_m^{nit} = 3m_{Si}\mu_{Si}/m_{nit} + 4m_N\mu_N/m_{nit}$$

Figure 10: Calculated half-value absorption lengths for gold and silicon nitride.

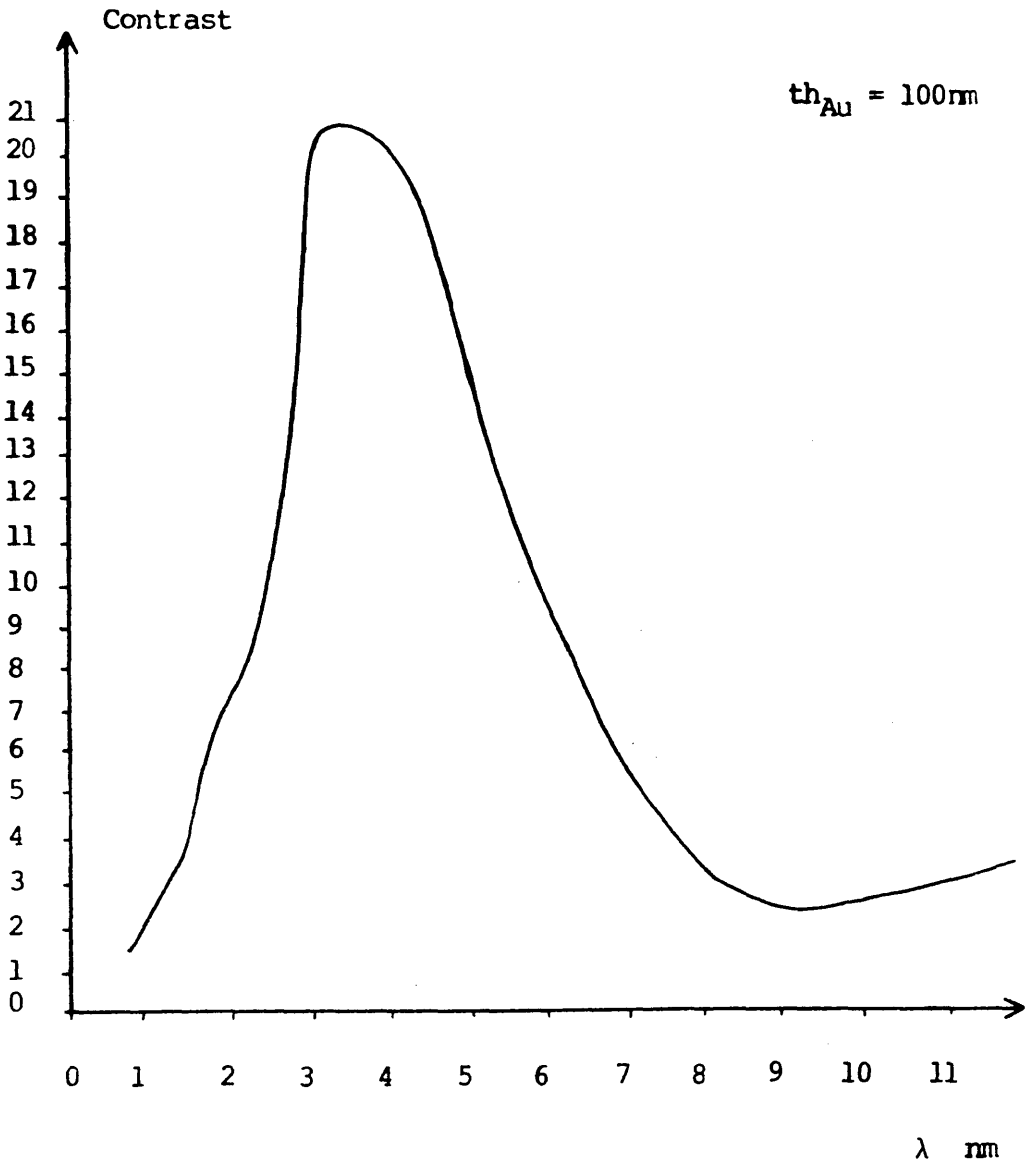

Contrast = I_{clear}/I_{dark}

Contrast only depends on the absorbent.

Figure 11: Contrast versus wavelength for a 100 nm thick gold film.

depends on its absorbent qualities.

As a conclusion to this paragraph, the characteristics of the X-ray masks are summarised. The X-ray mask is to be made of a gold pattern lifted-off onto a silicon nitride membrane supported by a silicon wafer designed for X-ray printing at the carbon K_α line 44.8 angstroms.

C.3) Geometrical factors:

The geometrical characteristics to be considered are:

-The grating pitch.

-The membrane area and thickness.

-The gold thickness.

The gold thickness must be chosen so that it is easy to lift-off and yet thick enough to provide a good contrast under X-ray exposure. As seen in section B, a thickness around 100 nm will give an acceptable contrast.

Although a thin membrane is desirable for good X-ray transmission, it must be sturdy enough so that the mask does not break at the first exposure. Membranes of thicknesses over 50 nm are now fabricated routinely with good reliability. The membrane thicknesses will be kept between 50 and 100 nm. A definite value is not yet given for it will be explained how, by judiciously choosing the silicon nitride thickness, the lift-off process can be made successful [Ref.67].

The grating pitch and membrane area (and therefore pattern area) are determined by the requirements of the optoelectronics industry. A thorough search through the past five years of research [Ref.8-11,68-96] shows a trend towards the use of semiconductor such as GaAs, InP, GaAlAs, GaInAsP, and other III-V tertiary or quaternary compounds, in the fabrication of integrated lasers. The grating dimensions required for the

production of DFB or DBR lasers range from a few hundreds to a thousand microns for the length and around tens of microns for the width. It was therefore decided to produce 1 mm^2 area membranes coated with a grating pattern in view of the fabrication of distributed feedback lasers operating at wavelengths in the range 0.8 to 1.7 microns in media of indices around 3.5 by first or second order Bragg interactions. Calculations, using the mode-matching formula (14), lead to grating pitches ranging from 0.12 to 0.45 microns.

This concludes the "General theoretical background" part of the thesis. The next two parts deal with the theoretical study and the fabrication of metal gratings in view of the production of a X-ray mask whose characteristics are summarised in figure 12.

Grating pitch ranging from 0.12 to 0.45 micron.

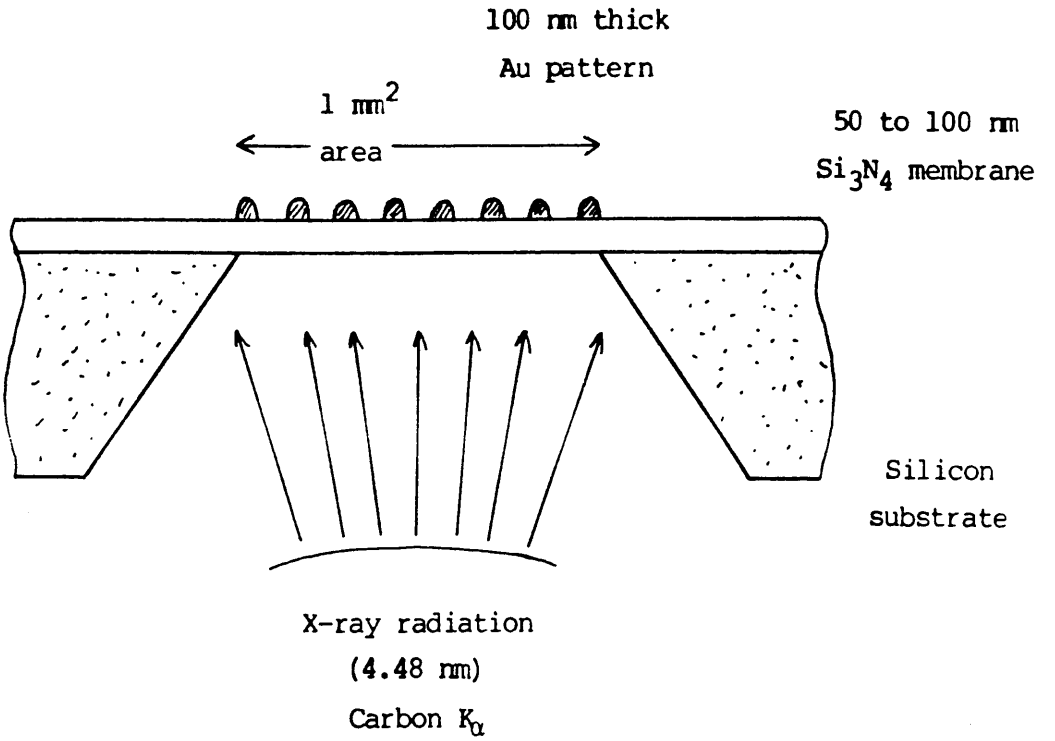

Figure 12: The characteristics of an X-ray mask and its environment.

PART II

THEORETICAL STUDY

Detailed investigation of the holographic process, computer simulation.

INTRODUCTION

The fabrication of 1 mm^2 gratings, of pitch ranging from 0.12 to 0.45 micron, has been undertaken. This part deals with the recording of such gratings in a photoresist layer coating a silicon nitride/silicon substrate.

There are two alternative ways of printing gratings. Electron beam lithography is the most sophisticated means of doing it [Ref.10,97]. It satisfies the very high resolution requirements and allows for great versatility particularly when making quarter-wave shifted [Ref.98,99], chirped gratings and any other unconventional structures or line profiles. However, although there obviously is great potential in today's E-Beam systems for grating generation, they cannot yet meet the overall size requirements. Pin-cushion or barrel distortions, due to inherent aberrations within the electron scanning system, limit the largest grating areas that can be obtained by electron beam lithography to less than 400 square microns [Ref.10]. Moreover, stitching errors occur when attempting to print larger gratings by mechanically moving the recording sample.

An alternative method has been in use for a long time. It takes advantage of the optical phenomenon arising when two beams of coherent light meet. As the interference arrangement clearly resembles a hologram generation bench, it is often referred to as holographic printing. If by holographic printing one designates the recording of interference fringes between object and reference beam the appellation is quite adequate. Holographic gratings have been made at GLASGOW UNIVERSITY since 1973 [Ref.100-102] and despite having been in use for such a long time, recording gratings on a holographic bench still requires a bit of "savoir-faire" and a lot of patience.

The work undertaken was two-fold. Apart from using the holographic process as a mean of generating gratings towards the design of an X-ray mask, the purpose of our work was also to

improve the reliability and predictability of the holographic process. To this end a theoretical study of the process was carried out. It includes the examination under gaussian optics formalism of a typical holographic arrangement (section A), it follows on with a theoretical formulation of the interference phenomenon within a multilayer system (sections B&C) and concludes with a computer simulation of the grating recording process in a photoresist layer (section D).

A: OPTICAL BENCH STUDY

After a brief review of the classical settings for a holographic bench, a gaussian analysis of a typical set-up is presented. The section concludes on a justification for the plane wave approximation often assumed when printing gratings.

A.1) The holographic arrangement:

Grating generation involves the recording of the interference pattern existing in the meeting area of two coherent beams. On a holographic bench, the two beams originate from the same laser unit and the division is done by a beam-splitter (in our case a half reflecting mirror). Both beams are then redirected onto the sample the interference pattern is to be recorded on. When a beam of laser light is generated, the fundamental optical line is surrounded by a pattern of speckles due to a scattering phenomenon and it is often necessary to "clean" such a beam, with a spatial filtering system which will remove the unwanted spatial frequencies, before gratings can be produced.

Components of a holographic arrangement:

- -Laser light generator
- -Beam splitter
- -Redirecting mirrors
- -Spatial filtering system
- -Sample holder

There are many ways of choosing and arranging these components together, each alternative having its own drawbacks and advantages [Ref.103,104].

The arrangement which was used in this work is shown in figure 13. A three-mirror arrangement [Ref.100-102] could have been used. Its main advantage over a two-mirror setup is that the enhancement of the beam defects caused by the lateral inversion phenomenon is prevented by the third reflection. However, adding a third mirror to the setup would:

- Complicate the alinement procedure
- Introduce further defects in the beam due to deformation of this extra optical surface, or to any speckle of dust lying on it.

- Destroy the symmetry of the beam's light intensity, thus degrading the interference fringes contrast.

A two-mirror arrangement was therefore chosen and the lateral inversion phenomenon circumvented by placing a spatial filter unit between each redirecting mirror and the sample holder. Collimating lenses are often used to transform the spherical gaussian waves issuing from the filtering units into plane gaussian waves. However, inclusions or bubbles in such lenses can also introduce perturbations in the optical wavefronts and this is why it was decided not to use them. Provision was also made for the front prism technique which consists in artificially lowering the light wavelength by the use of an "input medium" (a glass prism) of a higher refractive index than air [Ref.105,106].

A.2) Interference pattern:

Before going into more details on the theory of gaussian beam propagation and applying it to the optical set-up figure 13, the semi-quantitative reasoning below describes the behaviour of a typical holographic arrangement. A laser beam is divided by a beam splitter, of a design assuring a 50-50 split, into two beams of equal intensity. Both beams are made to converge on the recording medium by redirecting mirrors. Before they actually interfere they are spatially filtered. A pinhole placed at or near the focal point of a good quality short-focus converging lens (in our case f.l. of 20 mm) will remove unwanted noise and spatial frequencies (providing lens and pinhole are well adjusted). Sometimes a long focal length converging lens is placed so that it forms an afocal system with the short lens, the diverging beam coming from the pinhole becomes collimated (hence the name of collimating lens) into a parallel beam. It will be seen that such a combination of short lens-pinhole-long lens, not only carries out the filtering but also expands the beam in a ratio equal to the quantity long focal length/short focal length. Provided the two beams are of equal intensity and of symmetric incidence when they strike the recording sample, good quality gratings can be obtained [Ref.107]. If each beam is assumed to be a plane wave (justification is presented below) of vertical s-polarization as defined in figure 14, it can be shown

(Appendix.1) that a periodic pattern of vertical lines exists with a periodicity Λ, the grating pitch, satisfying the equation:

$$\Lambda = \lambda/(2n\sin\theta) \qquad (18)$$

where θ is the angle of incidence, λ the light wavelength (in a vacuum) and n the index of the "input medium". Leaving aside the front prism technique where n, the prism index, is greater than 1, equation (18) takes the simpler form:

$$\Lambda = \lambda/(2\sin\theta) \qquad (19)$$

In the fabrication of gratings, the pitch Λ is the given quantity and the holographic bench is set to the angle given by:

$$\theta = \sin^{-1}(\lambda/2\Lambda) \qquad (20)$$

If the fabrication of gratings presenting a pitch smaller than $\lambda/2$ is envisaged, the front prism technique must be used. However, even though one might think that a high index input medium and a grazing incidence would be the most promising solution to short pitched grating fabrication, the increase in the beams cross section due to this settings dramatically enhances the beams defects and spoils all such hopes.

The most important points in the arrangement of a holographic bench have been mentioned. The absence of a collimating lens gives rise to long exposure times since the beam intensity is not focussed into a parallel beam but diverges to infinity. It was found that this is not detrimental to the grating quality.

A.3) Gaussian formalism:

It is necessary to involve gaussian optics any time a laser beam is used because of their gaussian profile. The formalism can be examined in full details in [Ref.108,109]; the purpose of this paragraph is to restate the basic properties of gaussian beams and their transformation through optical systems.

A.3.1. Gaussian wave characterisation.

Within the notation in figure 15, the wave equation and the assumption that the wave presents a symmetry of revolution leads to the following representation for the electric field:

$$E = E_0 \exp(-ikz) \exp\left[-i\left[P(z)+kr^2/(2q(z))\right]\right] \qquad (21)$$

where $q(z) = z+q_0$, $k=2\pi n/\lambda$ and

$$P(z) = -iLn(1+z/q_0) \qquad (21a)$$

q_0 satisfies:

$$q_0 = i\pi n w_0^2/\lambda \qquad (21b)$$

where w_0, called the waist of the beam, is the half-width at 1/e points for $z=0$.

The quantity $q(z)$ can be decomposed in terms of the waist $w(z)$ and the radius of curvature $R(z)$ at a z-plane:

$$1/q(z) = 1/R(z) - i\lambda/(\pi n w^2(z)) \qquad (22)$$

with

$$w^2(z) = w_0^2(1+z^2/z_0^2) \qquad (22a)$$

and

$$R(z) = z(1+z_0^2/z^2) \qquad (22b)$$

where the quantity z_0 has been introduced for ease of writing and satisfies:

$$z_0 = \pi w_0^2 n/\lambda \qquad (22c)$$

Equation (21) can then be rewritten as:

$$E = E_0 (T1)(T2)(T3) \qquad (23)$$

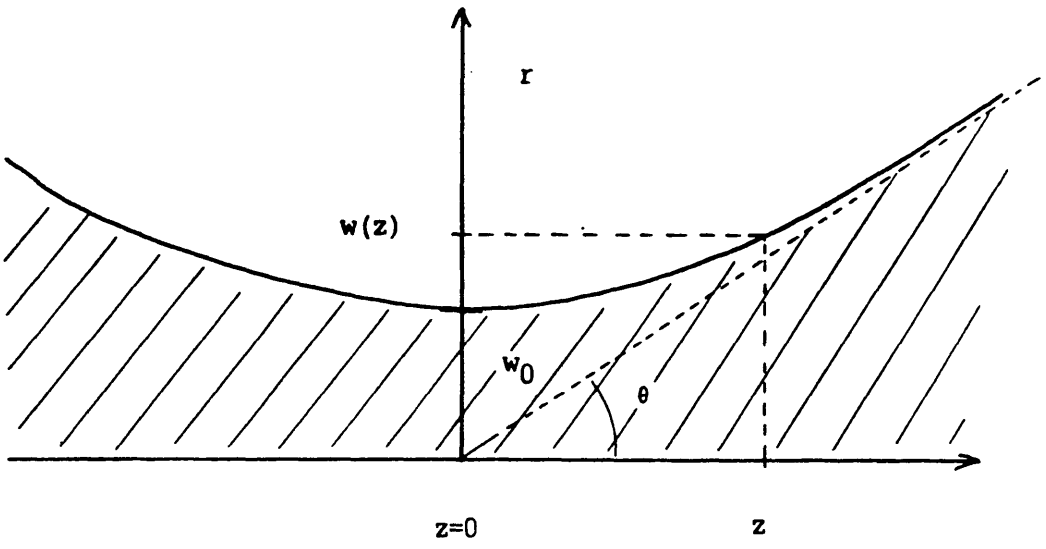

* z propagation axis.
* r distance from axis.
* there is no coordinate θ since the axial symmetry is assumed.
* w_0 is the waist of the beam and w(z) the waist at plane z such that: $E(z,w) = E(z,0)1/e$
* note that z is always referred to the "focal" plane where the waist is at its minimum.
* θ is the half angle of the beam when $z \to \infty$.

Figure 15: Geometry of a gaussian beam.

with

$$T1 = (1+z^2/z_0^2)^{-1/2} \tag{23a}$$

$$T2 = \exp\left[-i[kz-\tan^{-1}(z/z_0)]\right] \tag{23b}$$

$$T3 = \exp\left[-r^2[1/w^2(z)+ik/(2R(z))]\right] \tag{23c}$$

It is clear from equation (23) that the term (T1) describes the attenuation of the wave as it diverges from the waist. The term (T2) describes propagation along the z-axis and the term (T3) represents the transversal attenuation, i.e. the gaussian profile of the wave.

In conclusion, in order to fully characterise a gaussian beam at any point M, of cylindrical coordinates (r,z) (the angle is dropped due to the symmetry and the z-origin is taken at the focus of the beam, real or virtual), one only needs to know the quantity w_0, waist of the beam. The quantity z_0 is derived from w_0 using formula (22c) which in turn is replaced in equations (22a) and (22b) leading to the values of w and R (or the complex quantity q as defined by (22)) at the z plane. Equation (23) then fully represents the gaussian wave.

A.3.2. Waist of a laser beam.

Going back to equation (22a), it is interesting to find the expression of the quantity w/z when z increases to infinity.

$$(w/z)_\infty = w_0/z_0 = \lambda/(\pi w_0 n) \tag{24}$$

The quantity $(w/z)_\infty$ is related to the half-angle θ of the diverging beam as shown in figure 15 by:

$$(w/z)_\infty = \tan\theta \tag{25}$$

A laser beam being very close to a parallel beam has very little divergence and θ is a good approximation for $\tan\theta$. Therefore, measuring the half-angle of a laser beam at infinity, or at a

distance far greater than z_0 to be precise, leads to the laser waist w_0. The next step consists of measuring the waist of the beam at the output window of the laser and deriving the location of the waist with respect to the front of the laser from equation (22a). As an example, the SPECTRA-PHYSICS argon ion laser used during this work is specified to have an output beam diameter of 1.3 mm at a wavelength of 457.9 nm and a divergence angle (2θ) of 0.5 milliradians [Ref.110]. This data leads to a waist of 583 microns situated 1.15 metres behind the output window (this is in agreement with the laser cavity configuration formed by a converging output mirror and a flat reflector at the back end).

A.3.3. Transformation of a gaussian beam by a converging lens.

The last stage in gaussian formalism consists in deriving equations for the focussing of a laser beam by a converging lens. This section is particularly useful as the focal spotsize must be known when spatial filtering is to be carried out.

Within the thin lens approximation, going through a lens does not change the beam diameter but only introduces a phase factor [Ref.109]. From the geometrical optics theory, the phase term introduced by a lens of focal length f between input and output surfaces is:

$$\text{phase shift} = \exp\left(i\pi r^2/(\lambda f)\right) \tag{26}$$

When this phase shift is introduced in term (T3) of equation (23c), it becomes clear that the lens transformation is, using subscript 1 for the lens input plane and subscript 2 for the lens output plane:

$$w_1 = w_2 \tag{27a}$$

$$1/R_2 = 1/R_1 - 1/f \tag{27b}$$

It will be seen that for a laser beam, R_1 is far greater than f which means that R_2 becomes negative indicating that the wave is no longer diverging but converges towards a new focal point

(location of the waist w_{02}). The new waist size and its distance from the lens as defined in figure 16, are given by:

$$w_{02} = w_{01} f \left[(f-d_1)^2 + (\pi w_{01}^2/\lambda)^2 \right]^{-1/2} \qquad (28a)$$

and

$$d_2 = f + f^2 (d1-f) \left[(d1-f)^2 + (\pi w_{01}^2/\lambda)^2 \right]^{-1} \qquad (28b)$$

A.3.4. Determination of the filtering parameters.

The holographic bench studied within this section is geometrically described in figure 17.

From the laser waist w_{01} (583 microns) to the input surface of the lens, the distance d_1 is 2460 mm and the focal length f of the lens is 20 mm. Using equation (28a) and (28b) with λ=457.9 nm leads to:

$$d_2 = 20.09 \text{ mm} \qquad (29a)$$

$$w_{02} = 3.5 \text{ micron} \qquad (29b)$$

It is interesting to notice that the distance d_2 is very close to the focal length of the lens. In practice the position of the pinhole will be set at the focal plane of the lens, as in geometrical optics, and adjusted with a micrometer translation stage (the adjustment procedure is described in the experimental report, part III).

To determine the size of the pinhole, its diameter must be greater than $2w_{02}$, i.e. greater than 7 micron. A 10 micron diameter pinhole will let through more than 98% of the light intensity (from square of equation (23)) and appears to carry out the spatial filtering in a satisfactory manner. When it reaches the recording sample, the beam diameter should have increased to about 16 mm (from equation (22a)). This was however not observed because the circular aperture (pinhole), overlapping the beam profile, spreads the beam intensity among diffracted orders.

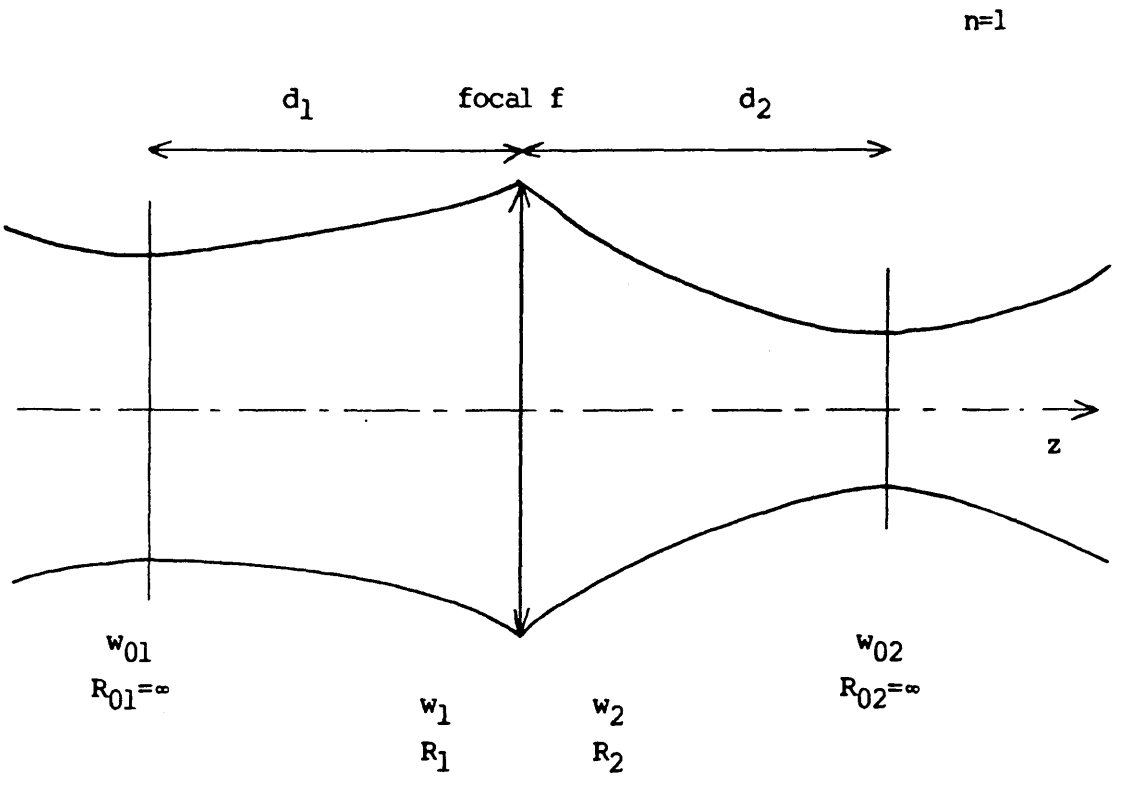

$1/R_2 = 1/R_1 - 1/f$ $\qquad\qquad$ $w_1 = w_2$

Figure 16: Transformation of a gaussian beam by a converging lens.

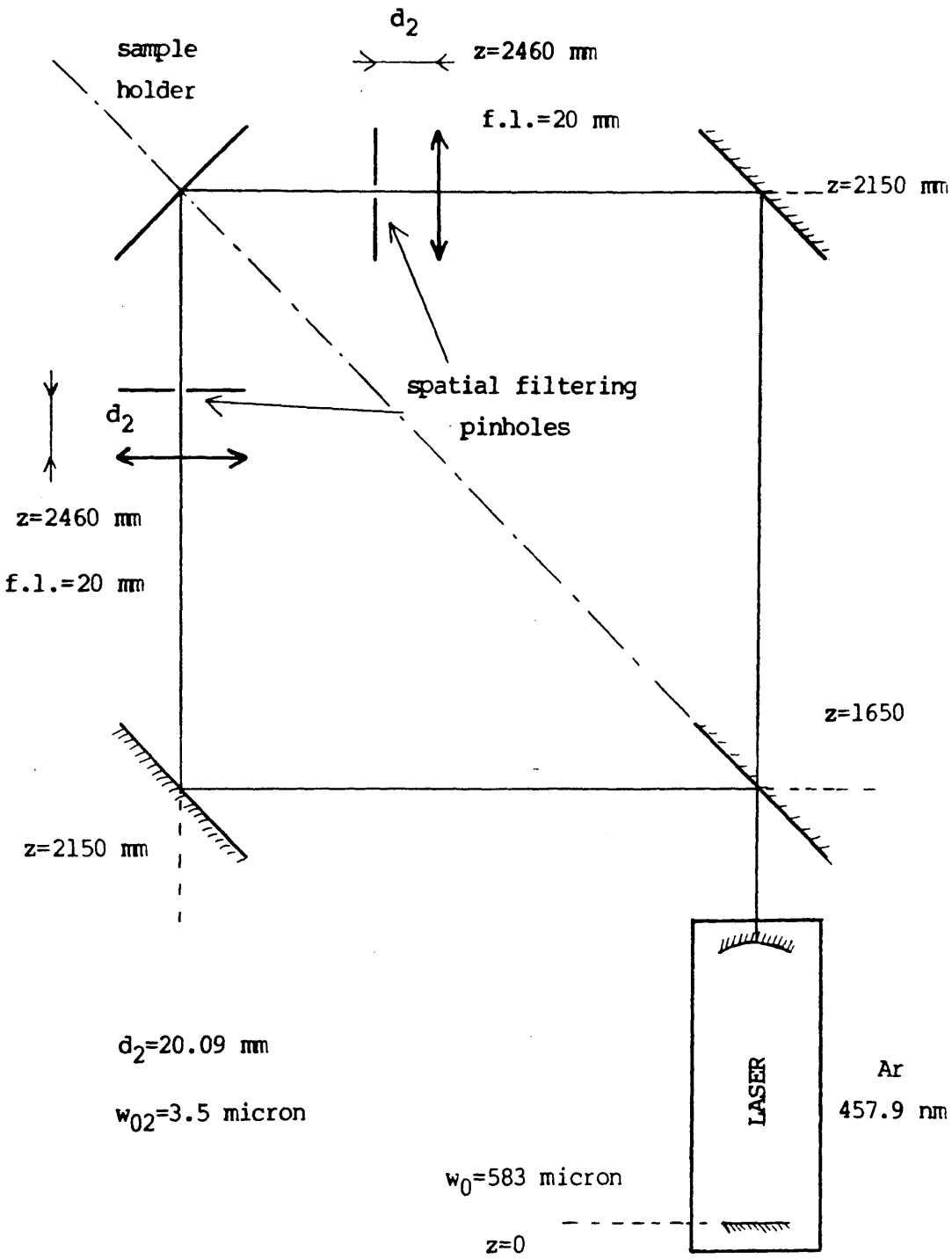

Figure 17: Description of the arrangement submitted to the gaussian formalism.
Determination of the waist and its position after the lens (d_2,w_{02})

A.4) Approximation to a plane wave:

It was decided to investigate the geometry of the grating pattern generated by interference between two spatially filtered gaussian non-collimated beams.

A.4.1 Notation and assumptions:

The calculations must take into account the gaussian nature of each beam and the diffraction from the pinholes. To this effect, the notation outlined in figure 18 was adopted. Two assumptions were also made:

-The Gauss approximation which will be justified further.

-A total symmetry was assumed between the two beams as this was the case with our arrangement.

In order to save space, the calculation will be presented with and index j when necessary, taking the values 1 or 2 (beam 1 or beam 2), and the quantity $\epsilon_j=(-1)^j$ will often be used.

A.4.2 Expression for the electric field $E(P,M_j)$:

According to HUYGHENS diffraction principle [Ref.109], the electric field at a point P on the sample is the summation over both apertures (the pinholes) of each luminous point M_j contribution considered as a spherical wave.

Each contribution can be expressed as:

$$E(P,M_j) = E(M_j)/|M_jP|\exp(-2i\pi|M_jP|/\lambda) \qquad (30)$$

The quantity M_jP is obviously important and verifies:

$$|M_jP| = \left[(z+\epsilon_j x\sin\theta)^2+(x\cos\theta-x_j)^2+(y-y_j)^2\right]^{1/2} \qquad (31)$$

Under the Gauss approximation ($x, x_j, y, y_j \ll z$), equation (31) can be written in a Taylor expansion:

$$|M_jP| = z\left[1+\epsilon_j x\sin\theta/z+r^2/(2z^2)+r_j^2/(2z^2) - (xx_j\cos\theta+yy_j)/z^2-x^2\sin^2\theta/(2z^2)+o(x/z)^2\right] \qquad (32)$$

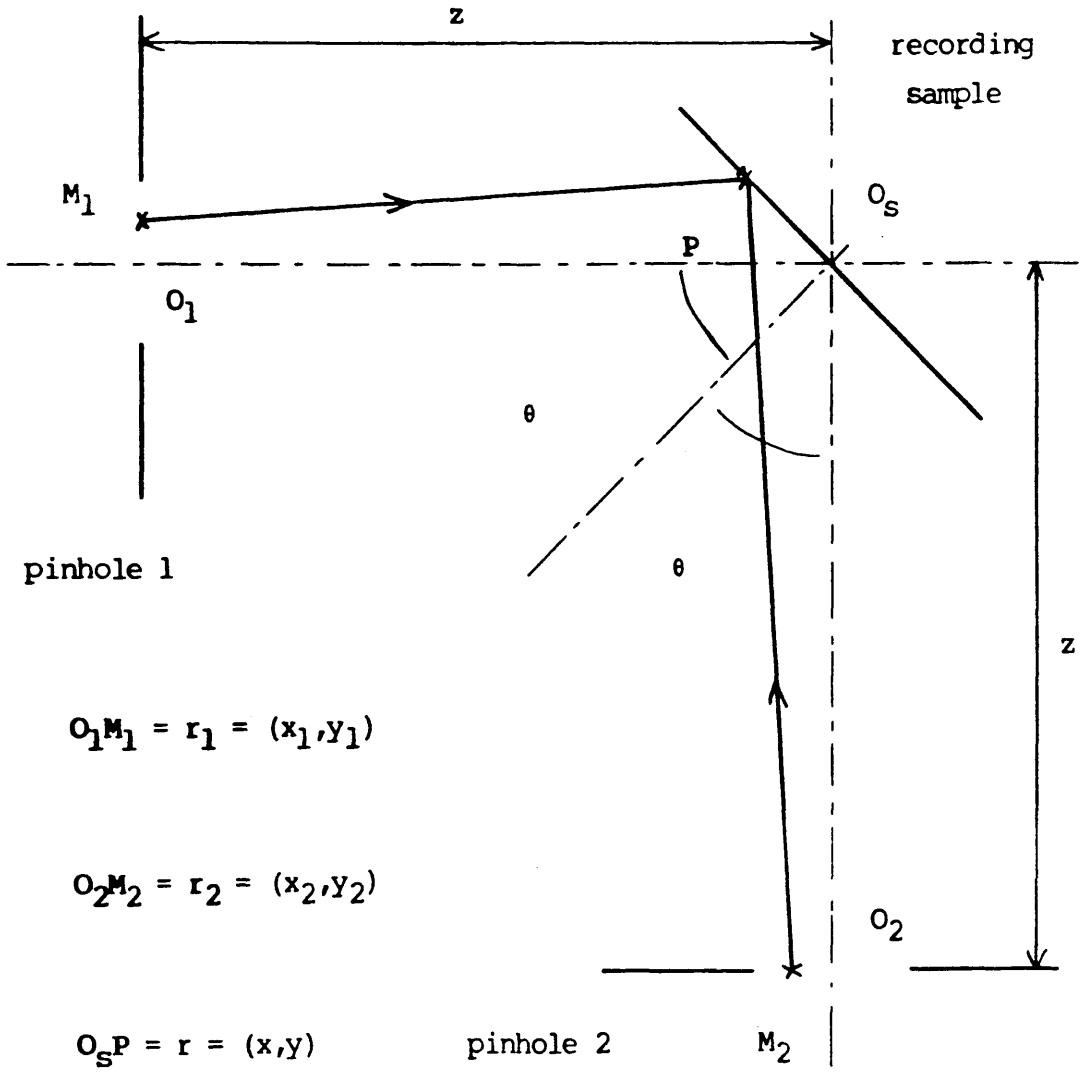

Gauss approximation: $z >> r_1, r_2, r$

Figure 18: Notation and approximation for spherical wave interference calculations.

And an expression for M_jP^{-1} can similarly be obtained:

$$|M_jP|^{-1} = 1/z\left[1-\epsilon_j x\sin\theta/z+o(x/z)\right] \tag{33}$$

By replacing equations (32) and (33) in equation (30), the expression for the spherical wave can be obtained:

$$E(PM_j) = T(P)U(P,\epsilon_j)V(P,M_j) \tag{34}$$

where T(P) does not depend on either M_j nor ϵ_j:

$$T(P) = 1/z\exp\left[-2i\pi/\lambda[z+r^2/(2z)-x^2\sin^2\theta/(2z)]\right] \tag{34a}$$

where $U(P,\epsilon_j)$ does not depend on M_j:

$$U(P,\epsilon_j) = (1-\epsilon_j x\sin\theta/z)\exp(-2i\pi/\lambda\epsilon_j x\sin\theta) \tag{34b}$$

and where $V(P,M_j)$ does not depend on ϵ_j:

$$V(P,M_j) = E(M_j)\exp\left[-2i\pi/\lambda[r_j^2/(2z)-(xx_j\cos\theta+yy_j)/z]\right] \tag{34c}$$

$E(M_j)$ is an expression of the light distribution within the pinhole j (waist w_0 and infinite curvature) and verifies:

$$E(M_j) = E_0\exp(-r_j^2/w_0^2) \tag{34d}$$

A.4.3 Integration over the pinholes area:

The total field E(P) at point P can be expressed as :

$$E(P) = T(P)\left[U(P,\epsilon_1)+U(P,\epsilon_2)\right]\int_{\text{pinholes}} V(P,M_j)\,dr_j \tag{35}$$

In the evaluation of the integral I, the index j becomes irrelevant and will be dropped:

$$I=E_0\int_0^a\int_0^{2\pi}\exp\left[-r^2[1/w_0^2+i\pi/(\lambda z)]\right]\exp\left[2i\pi ru\cos\phi/(\pi z)\right]\,rdrd\phi \tag{36}$$

where a is the pinhole radius, u the modulus of vector $\mathbf{u}(x\cos\theta, y)$ and ϕ the angle between vectors **u** and **r**.

Using the identity:

$$J_0(x) = 1/\pi \int_0^{\pi} \exp(ix\cos\phi)\, d\phi \tag{37}$$

where J_0 is the BESSEL function of the first kind [Ref.111], leads to:

$$I = 2\pi E_0 \int_0^{a} \exp\left[-r^2 [1/w_0^2 + i\pi/(\lambda z)]\right] J_0(2\pi ur/(\lambda z))\, r\, dr \tag{38}$$

In the case of a 10 micron pinhole, far from its plane (in our case z=190 mm >> a=5 micron), it is simple to verify that:

$$1/w_0^2 + i\pi/(\lambda z) \approx 1/w_0^2 \tag{39}$$

Thus expression (38) becomes:

$$I = 2\pi E_0 \int_0^{a} \exp(-r^2/w_0^2) J_0\left[2\pi ur/(\lambda z)\right] r\, dr \tag{40}$$

The object of this paragraph is not to develop an analytical solution for the above integral and a qualitative study is proposed below, describing the behaviour of the integral.

Relating integral (40) to WEBER's first exponential integral [Ref.112],

$$\int_0^{\infty} r J_0(ar) \exp(-p^2 r^2)\, dr = 1/(2p^2) \exp(-a^2/(4p^2)) \tag{41}$$

indicates that the field will behave in an $\exp(-(u/w)^2)$ manner, i.e. in a gaussian way. The actual diffraction pattern is as usual introduced by the fact that the integration is over a finite interval. Setting aside the exponential term in the integrand for a while, discloses a behaviour of the J_1 type, where J_1 is a BESSEL function of the first kind, due to the identity [Ref.112]:

$$\int_0^{\alpha} xJ_0(x)dx = \alpha J_1(\alpha) \qquad (42)$$

The larger the aperture, the closer this representation is to reality. In the numerical case described previously (a=5 micron), it is a good representation of the patterns obtained during our work. It is particularly interesting to estimate the diameter of the first dark ring of the interference pattern given by the first zero of J_1:

$$J_1(2\pi au/(\lambda z)) = 0 \qquad (43)$$

which leads to:

$$2\pi au/(\lambda z) = 3.832 \qquad (1^{st} \text{ zero of } J_1 \text{ [Ref.111]}) \qquad (66)$$

and yields:

$$u = 11 \text{ mm} \qquad (45)$$

The first dark ring is then about 22 mm in diameter and this is in good agreement with what was obtained experimentally.

In our case, the parameters appearing in the integral have the following numerical values:

$$0 < u < 1 \text{ mm} \qquad (46a)$$

$$w_0 = 3.5 \text{ micron} \qquad (46b)$$

$$a = 5 \text{ micron} \qquad (46c)$$

$z = 190$ mm (46d)

$\lambda = 457.9$ nm (46e)

Evaluating the BESSEL function and the exponential term in the integrand for the limits of the integration (using tables in [Ref.113]):

$0.96 < J_0(...) < 1.00$ (47a)

$0.16 < \exp(..) < 1.00$ (47b)

It is justified under such conditions to assimilate the expression $J_0(....)$ to unity. This leaves an integral which does not depend upon the quantity u and that can therefore be considered as a constant I_c in equation (35).

A.4.4 Interference phenomenon:

Under the assumption that the integral in equation (35) can be approximated as being a constant, the field expression becomes simpler:

$$E(P) = I_c T(P)\left[U(P,\varepsilon_1)+U(P,\varepsilon_2)\right] \quad (48)$$

Evaluating the quantity between brackets with equation (34b) leads to:

$$E(P) = 2I_c T(P)\left[\cosh(2i\pi x\sin\theta/\lambda)+x\sin\theta/z\sinh(2i\pi x\sin\theta/\lambda)\right] \quad (49a)$$

or

$$E(P) = 2I_c T(P)\left[\cos(2\pi x\sin\theta/\lambda)+ix\sin\theta/z\sin(2\pi x\sin\theta/\lambda)\right] \quad (49b)$$

The light intensity is evaluated by taking the square modulus of equation (49b):

$$I(P) = 4I_c{}^2/z^2\left[\cos^2(2\pi x\sin\theta/\lambda)+x^2\sin^2\theta/z^2\sin^2(2\pi x\sin\theta/\lambda)\right] \quad (50a)$$

or

$$I(P)=2I_c^2/z^2\left[(1+x^2\sin^2\theta/z^2)-(1-x^2\sin^2\theta/z^2)\cos(2\pi x2\sin\theta/\lambda)\right] \quad (50b)$$

A.4.5 Conclusion:

Comparison between the interference equation for two plane waves (equation (A20) appendix 2) and the spherical wave equation (50b) leads to the following conclusions:

-The grating pattern still exists, with the same periodicity and orientation (cosine term).

-The contrast of the grating lines in the case of the spherical waves is however not as good as when plane waves are used. But numerical evaluation shows that the degradation is negligeable:

$$x^2\sin^2\theta/z^2 = 6.10^{-5} \quad (51)$$

-The overall light intensity does not stay constant with z but decreases as its square. This is not surprising since the waves issuing from the pinholes are diverging.

It is therefore perfectly justified to consider that the two interfering waves are plane waves. The contrast degradation factor ($x^2\sin^2\theta/z^2$) is a very good indication of the validity of such an assumption and it is interesting to remark that its dependence on the angle of incidence, the sample to pinhole distance and the excursion on the sample is in agreement with experimental observation.

B: OPTICAL THEORY FOR ABSORBING MEDIA

The purpose of this section is to state the notation used throughout the next chapter. It deals with the properties of optically absorbing isotropic media. Most of its material is inspired from a classical textbook [Ref.114].

B.1) Complex index:

When dealing with an absorbing medium it is convenient to introduce a complex refractive index the imaginary part of which is a representation of its absorption properties. Using a "^" as an indication of a complex number, the refractive index verifies:

$$\hat{n} = n - i\alpha \tag{52}$$

And, within the configuration described in figure 19, the electric field can be written (setting aside the time dependence) as:

$$E(M) = E_0 \exp(-2i\pi \hat{n} |OM|/\lambda) \tag{53}$$

By replacing (52) in (53) one gets:

$$E(M) = E_0 \underbrace{\exp(-2\pi\alpha|OM|/\lambda)}_{(T1)} \underbrace{\exp(-2i\pi n|OM|/\lambda)}_{(T2)} \tag{54}$$

It is easy to observe that the term (T2) describes the usual propagation in a non-absorbing medium while the term (T1) represents the absorption properties.

B.2) SNELL's law in an absorbing medium:

Linearity considerations on the continuity conditions at the interface between two media show that SNELL'law is valid even when complex indices are used. Within the notation outlined in figure 20, one obtains:

$$n_0 \sin\theta_0 = \hat{n}_1 \sin\hat{\theta}_1 \tag{55}$$

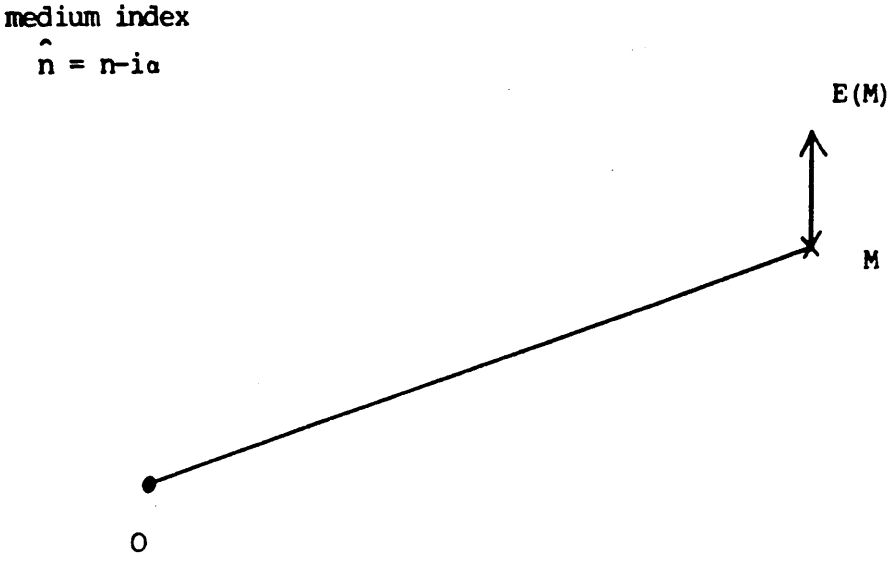

$$E(M) = E(O)\exp(-i2\pi\hat{n}|OM|/\lambda)$$

Figure 19: Electric field in an absorbing medium.

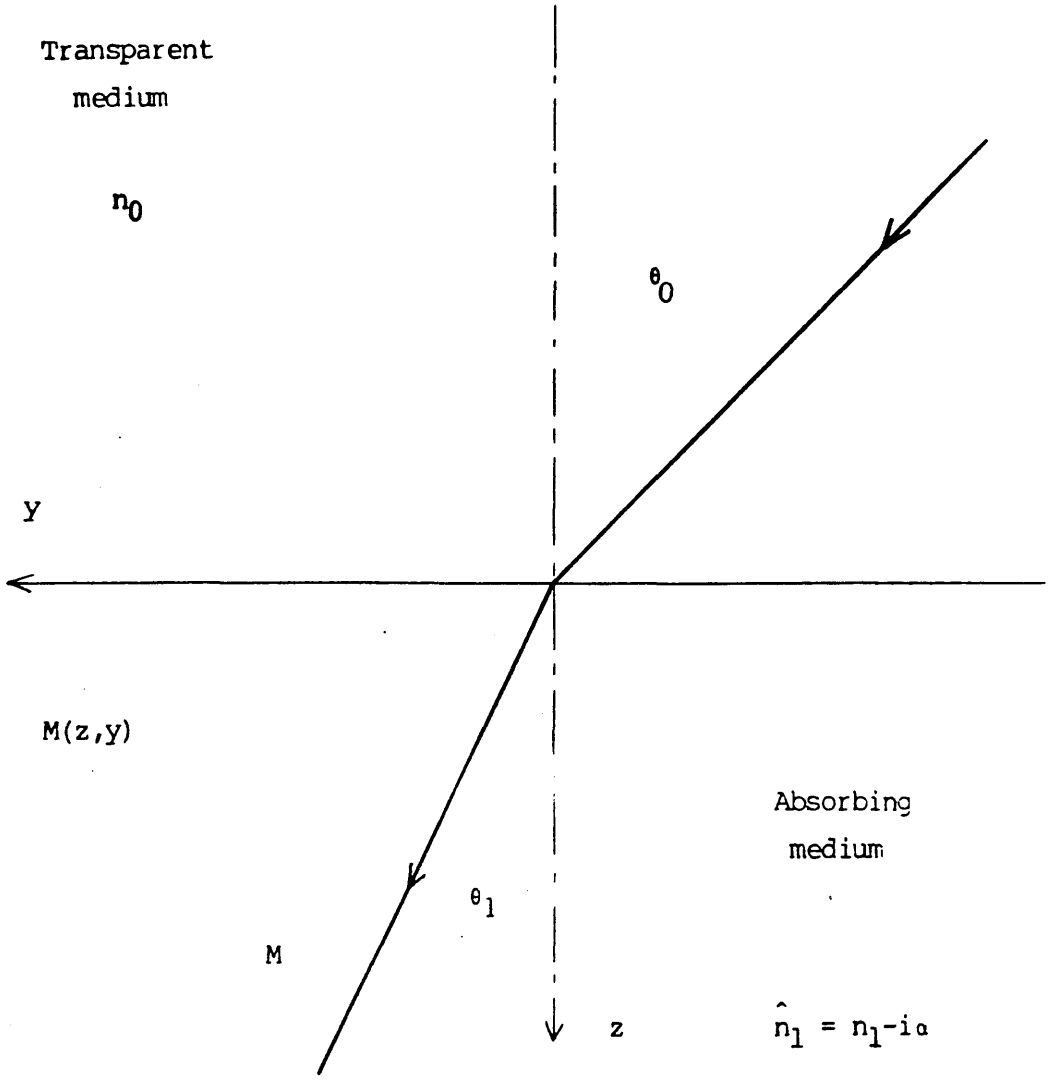

Figure 20: Notation and axis at the interface between $n_0/\hat{n}_1$.

As the medium indexed 0 is transparent, the left term in (55) is real. This forces the quantity $\sin\theta_1$ in the right term to be complex. The notion of complex angle is then introduced when analysing absorbing media at non-normal incidences and explains the "^" on θ_1.

B.3) Non homogeneous wave:

The physical interpretation of a complex angle is to be explained. Decomposing the wave vector $\hat{k}$ on the (z,y) axis, see figure 20, in medium 1 leads to the following exponent in equation (53):

$$\text{expon} = -2i\pi/\lambda(\hat{n}_1\sin\theta_1 y+\hat{n}_1\cos\theta_1 z) \qquad (56)$$

Keeping in mind that the quantity $\hat{n}_1\sin\hat{\theta}_1$ is real and decomposing the $\hat{n}_1\cos\hat{\theta}_1$ into real (a) and imaginary (b) part, leads to:

$$\text{expon} = -2\pi/\lambda\left(bz+i(\hat{n}_1\sin\hat{\theta}_1 y+az)\right) \qquad (57)$$

which, once replaced in (53) yields:

$$E(M) = E_0\exp(-2\pi bz/\lambda)\exp\left(-2i\pi/\lambda(\hat{n}_1\sin\hat{\theta}_1 y+az)\right) \qquad (58)$$

$$E(M) = E_0\exp(-2\pi bz/\lambda)\exp\left(-2i\pi/\lambda(n_1\sin\theta_1 y+az)\right)$$

It is clear from equation (58) that the planes of equal intensity are parallel to the interface and do not coincide with the planes of equal phase. Such a wave is qualified as being inhomogeneous. It is important to note that, although the attenuation only takes place along the normal to the interface, the attenuation coefficient itself ($2\pi b/\lambda$) depends upon the angle of incidence. Using complex indices and complex angles therefore not only takes into account the absorption within the medium but also represents any angle of incidence.

B.4) The case of critical incidence:

It is important to verify that the case of critical incidence is included in the above formalism. Assuming a non-absorbing medium for simplicity, it is possible to show that the introduction of complex angles includes the critical angle case.

The condition for which the critical angle is attained is when SNELL's law leads to:

$$|\sin\hat{\theta}| > 1 \tag{59}$$

Such a condition leads to the following conclusions (remember the medium is assumed non-absorbent):

$$\sin\hat{\theta} > 1 \text{ and real} \tag{60a}$$

$$\cos\hat{\theta} \quad \text{imaginary} \tag{60b}$$

It leads to an exponent of the type:

$$\text{expon} = \left(-2i\pi n/\lambda(\sin\theta y + \cos\hat{\theta} z)\right) \tag{61}$$

(the "^" has been dropped from $\sin\theta$ to indicate its overall real nature) or:

$$\text{expon} = -\alpha z - i\beta y \tag{62}$$

where α and β are two positive real numbers. Such an exponent characterises a wave which does not propagate at all in the considered medium but is on the contrary attenuated along the z-axis (first term in (62)). The second term in (62), a phase factor only y-dependent, is an indication that this is a surface wave. Thus is the case of critical angle included in the complex formalism.

B.5) Conclusion:

It is very convenient to use complex quantities in SNELL'law. A complex refractive index takes into account the absorbing properties of the medium and a complex angle not only is a representation of an inhomogeneous wave but also includes any case of incidence on an interface, whether before or past the critical angle. Such a formalism will therefore be used extensively in the next chapter when dealing with multilayer formalism and computer simulation.

C: MULTILAYER FORMALISM

A very good and effective multilayer formalism for the treatment of thin films systems can be found in [Ref.115]. The use of such a formalism with the complex quantities introduced in the previous sections allows a simple modelling of the interference phenomena in a multilayer absorbing system. This short section only restates the different recurrence relations that are used in a computer simulation.

C.1) Notation:

The subscript j is used for the recurrence layer in a multilayer system. As stated in figure 21, the electric field has to be considered at many different planes. Travelling through layer j are two waves: a transmitted wave E_j^t going in the z direction and a reflected wave E_j^r going the opposite way. Within a layer, the field propagates as in a homogeneous medium and it is easy to relate the field at one interface (j-1) to the field across the layer at interface (j). However, at the crossing of a boundary (j-1) or (j), continuity relations are to be applied in order to relate the fields on either side of the interface. The treatment of a multilayer system therefore includes the modelling of two different phenomena:

-the crossing of a boundary (j)

-the traverse of a thickness l_j of layer j.

To start, the wave is assumed to be normal to the system (propagation along z only). The case of oblique incidence is introduced in a latter stage.

C.2) Crossing a boundary:

The continuity requirements for the electromagnetic field across a boundary (j) between two media give the first relation in a matrix form:

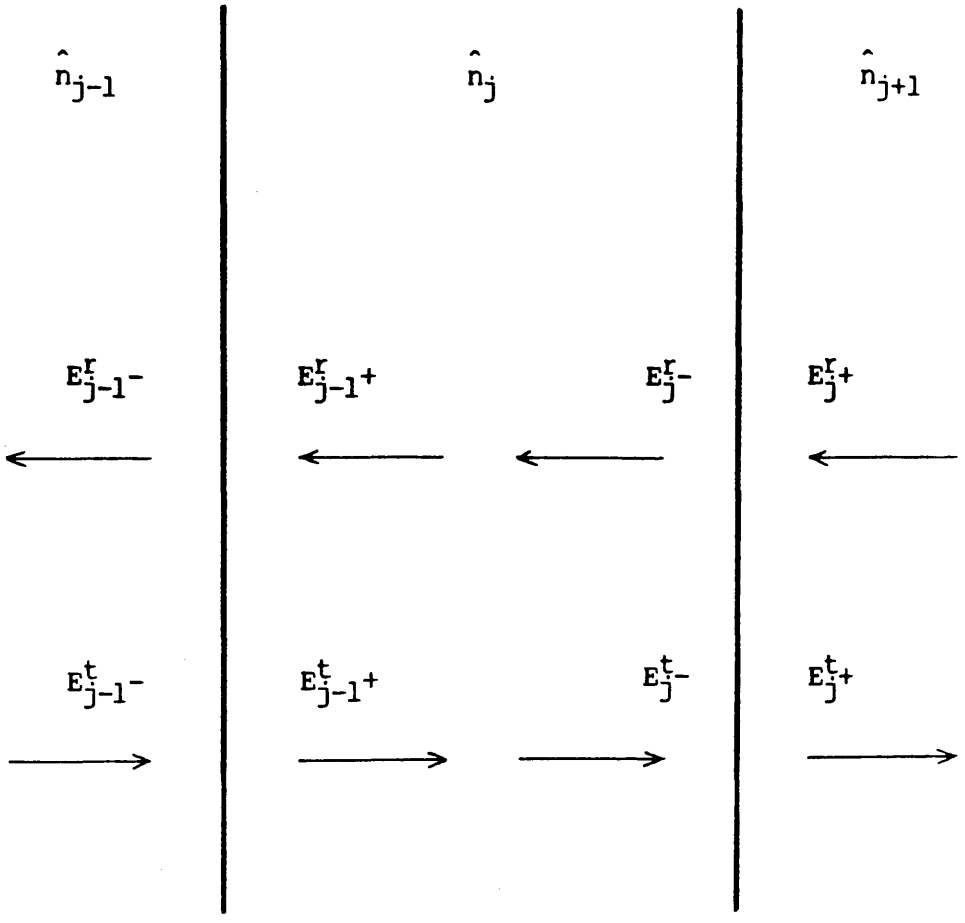

Figure 21: Notation for the recurrence layer.

$$\begin{bmatrix} E_j^{t-} \\ E_j^{r-} \end{bmatrix} = B_j \begin{bmatrix} E_j^{t+} \\ E_j^{r+} \end{bmatrix} \tag{63a}$$

where:

$$B_j = 1/2 \begin{bmatrix} 1+\hat{n}_{j+1}/\hat{n}_j & 1-\hat{n}_{j+1}/\hat{n}_j \\ 1-\hat{n}_{j+1}/\hat{n}_j & 1+\hat{n}_{j+1}/\hat{n}_j \end{bmatrix} \tag{63b}$$

For more details on the establishment of the expression for B_j refer to [Ref.115]. Note that complex indices are used throughout.

C.3) Traverse of a thickness l_j of layer j:

Writing in a matrix form the propagation and attenuation properties of a wave moving towards z positive for the transmitted wave and towards z negative for the reflected wave yields the following equation:

$$\begin{bmatrix} E_{j-1}^{t+} \\ E_{j-1}^{r+} \end{bmatrix} = T_j \begin{bmatrix} E_j^{t-} \\ E_j^{r-} \end{bmatrix} \tag{64a}$$

where:

$$T_j = \begin{bmatrix} \exp(2i\pi\hat{n}_j l_j/\lambda) & 0 \\ 0 & \exp(-2i\pi\hat{n}_j l_j/\lambda) \end{bmatrix} \tag{64b}$$

Note again the use of complex indices taking into account both phase shift and attenuation.

C.4) Introduction of the oblique incidence:

So far the equations used only hold for normal incidence. It is however easy to show that oblique incidences can be included in a simple fashion. Rewritting equation (56) in a different manner leads to:

$$\text{expon} = \left[-2i\pi/\lambda \hat{n}_1 \sin\hat{\theta}_1 y - 2i\pi/\lambda \hat{n}_1 \cos\hat{\theta}_1 z\right] \tag{65}$$

Stating SNELL's law, it will be seen that the first term in the exponent is a phase factor and remains constant throughout the entire multilayer system with y constant. This term can therefore be dropped for now and reintroduced after the multilayer system has been dealt with. Under these considerations, the electric field assumes the following form:

$$E(y,z) = \exp(-2i\pi n \sin\theta y/\lambda) E(0,z) \tag{66}$$

The subscript in the exponent has been dropped due to the conservation of the quantity $n\sin\theta$. The study of the field in the system is therefore reduced to the study of $E(0,z)$ which exponent satisfies:

$$\text{expon} = (-2i\pi \hat{n}_1 \cos\hat{\theta}_1 z/\lambda) \tag{67}$$

In other words, the incidence can be assumed to be normal and the concept of effective index introduced as follows:

$$\hat{n}_{jeff} = \hat{n}_j \cos\hat{\theta}_j \tag{68}$$

Therefore, in order to include the case of oblique incidence, every occurrence of refractive index within the formalism above must be replaced by its effective value as given by equation (68).

C.5) Resolution of a multilayer system:

Considering a system of n layers between two half-spaces, input medium and substrate, as shown in figure 22, the starting point consists in observing that only a transmitted wave exists in the substrate due to its infinite extent. In practice this is obtained by ensuring that the substrate thickness is much greater than the absorption distance in the substrate (>0.2 micron for silicon at 404.7 nm). The incident and reflected fields in the input medium verify:

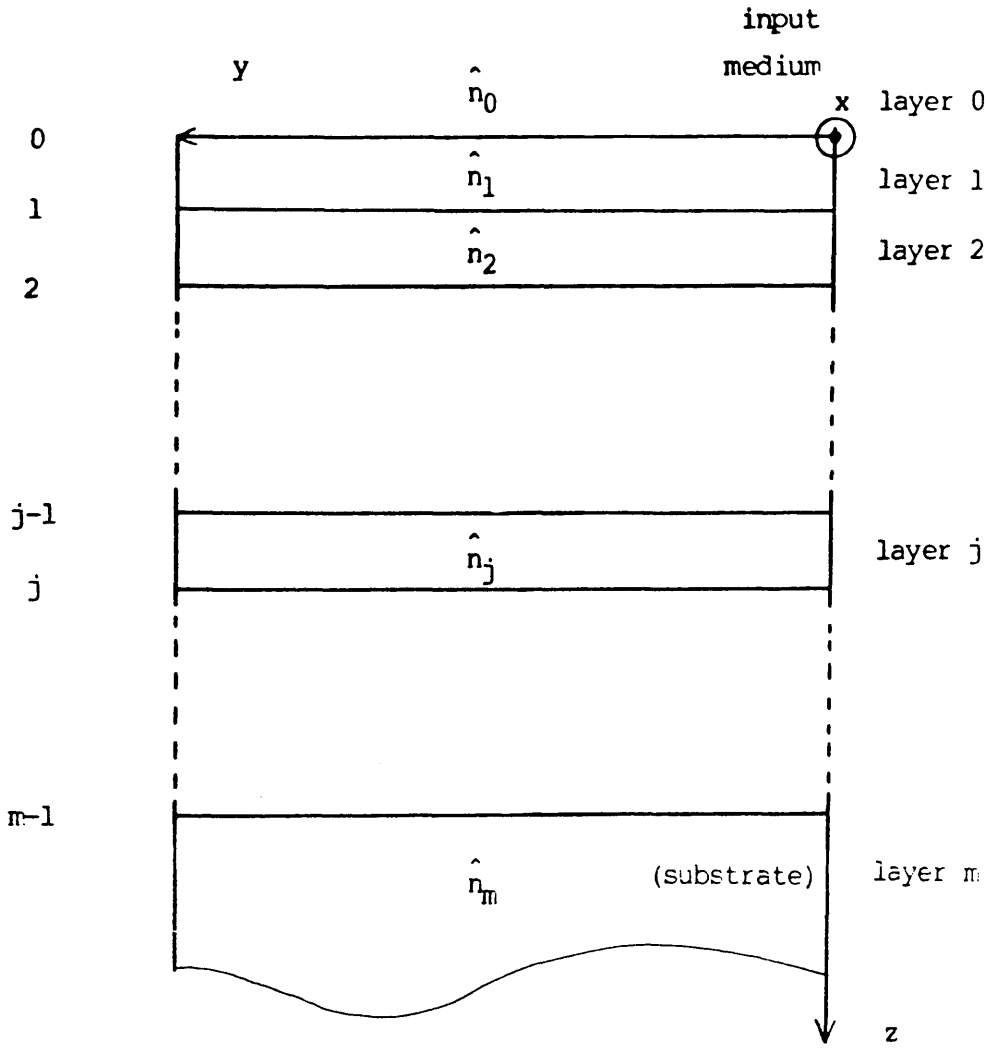

N.B: Layer j is between interfaces (j-1) and (j).

Figure 22: Multilayer system.

$$\begin{bmatrix} E^{(i)} \\ E^{(r)} \end{bmatrix} = M \begin{bmatrix} E^{t}_{(sub-1)^+} \\ 0 \end{bmatrix} \tag{69}$$

where M is a product of matrices T_j and B_j.

If the following notation is adopted for M:

$$M = \begin{bmatrix} m_{11} & m_{12} \\ m_{21} & m_{22} \end{bmatrix} \tag{70}$$

then

$$E^{(i)} = m_{11} E^{t} \tag{71a}$$

$$E^{(r)} = m_{21} E^{t} = m_{21}/m_{11} E^{(i)} \tag{71a}$$

and the transmission and reflection coefficients are:

$$t = 1/m_{11} \tag{72a}$$

$$r = m_{21}/m_{11} \tag{72b}$$

These coefficients, being of complex nature, give both phase shift and amplitude informations on the reflected and transmitted waves. When numerically establishing the topography of the electric field in a stratified system, the quantity E_t is usually normalised to unity.

C.6) Conclusion:

By working up the way from the substrate interface towards the input medium, the fields (reflected and transmitted) can be found at any plane in the system. When the input medium has been reached, the incident field intensity is used to scale the field map as follows:

$$E(0,z) = 1/m_{11} E^{(i)} E_{norm}(0,z) \tag{73}$$

where the quantity $E_{norm}(0,z)$ is the value of the field found from the normalised hypothesis and $E^{(i)}$ the value of the incident field.

D: COMPUTER SIMULATION.

A computer simulation of the recording of a holographic grating within a positive photoresist (AZ SHIPLEY) layer coating a substrate as represented in figure 9b, was developed. The theoretical transcription of the properties of the positive resist is restated before the computer program structure is exposed.

D.1) The phenomenon to be modelled:

The experiment has been described previously and is shown in figure 14 and 17. During such an experiment the interference pattern recorded within the layer of photoresist can be divided into two phenomena. Such a division arises from equation (66) and is easily observed during experimental work. A transverse periodic interference pattern is formed in the resist film between "left" and "right" beams, characterised by its pitch Λ, which will create the grating required. However, another interference pattern is formed by the standing wave within the thickness of the resist film, arising from the interaction between the transmitted beams and those reflected from the various dielectric interfaces. We characterise this pattern by its periodicity 2u (where u stands for undercut). Our aim in simulating holographic exposure is to allow us to determine the pitch and amplitude of both interference pattern, Λ and u, by adjusting the material thicknesses and indices (where possible).

D.2) Resist modelling:

As explained by H.DILL et al. [Ref.116], positive photoresist of the diazo-type (e.g. SHIPLEY AZ), usually consists of three chemicals, a photoactive compound, a base resin and a suitable organic solvant. The resist is spun onto the sample and baked according to the usual procedure, after which most of the solvant has disappeared. The solubility of the resist film in an aqueous alkaline developer becomes very high in areas where the photoactive compound has been broken up by light and stays very low in the shadowed areas hence the name of inhibitor for the

active compound. The absorption coefficient of the resist at a plane z and at time t is assumed to be a linear function of M(z,t), the remaining inhibitor fraction, according to the following formula:

$$\hat{n}_{resist} = n_r - i\lambda/(4\pi)\left[A*M(z,t)+B\right] \qquad (74)$$

where A and B are two resist dependent constants.

Calling C the fractional decay rate of inhibitor per unit intensity and I(z,t) the light intensity at any z plane at time t, one can write the time dependent equation:

$$\partial/\partial t\ M(z,t) = -I(z,t)M(z,t)C \qquad (75)$$

with initial condition M(z,0)=1 at any z plane.

The resist layer is divided into sublayers in order to take into account the progressive bleaching of the material and hence determine accurately the vertical interference pattern. As the light intensity pattern is periodical in one horizontal axis, of pitch Λ, we only need to consider one period. We therefore consider a block of photoresist as shown in figure 23. The program then must provide us with an inhibitor fraction map over the area (resist thickness * pitch of the grating) accurate enough to describe properly the bleaching of the resist.

D.3) Program structure:

The flow chart presented in figure 24 describes the logical structure of the program. By using the theoretical tools introduced in the previous sections, the light intensity (INT) in the system is calculated for a small energy increment, then the inhibitor map (INH), the corresponding complex refractive index map (IND) and the new light intensity distribution within the photoresist. We then proceed by iteration until the energy increments sum up to the total light energy we decided to give the sample. The set of inhibitor fraction profiles for increasing values of incident energy is arranged in an inhibitor map (MAP1)

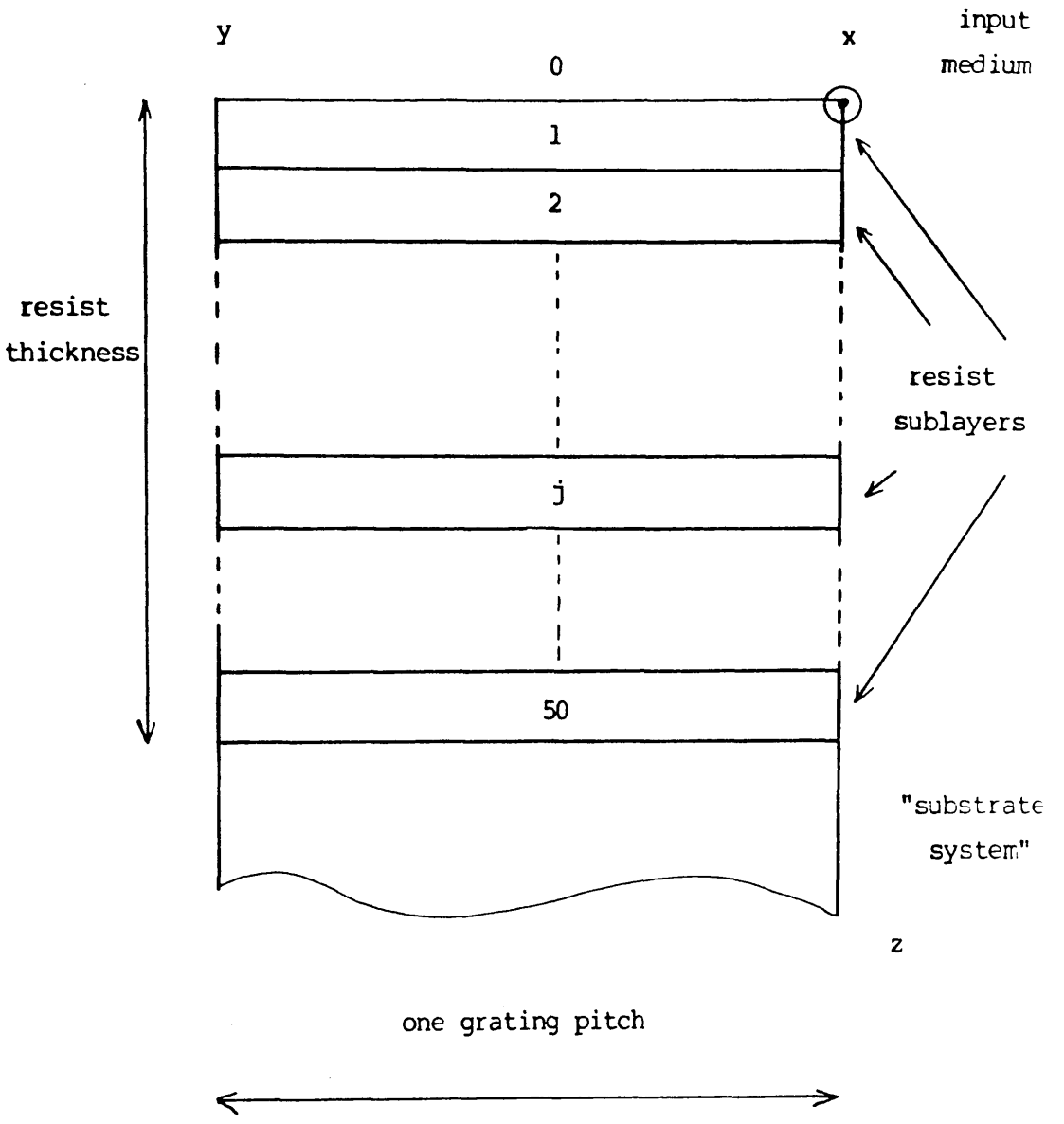

Figure 23: Illustration of the photoresist area used in the computer simulation.

Figure 24: The logical structure of BOLOGRAM.

expressed as a function of the two variables, depth and incident energy. With the help of the incident light intensity profile accross one pitch (calculations from appendix 1) the energy/depth map is transformed into a width/depth map (MAP2) by linear interpolation. The program, called HOLOGRAM, then transforms the inhibitor fraction map in a manner to suit part of an already existing program, SAMPLE [Ref.117], the task of which is to output the resist developed profile given the inhibitor map. Figure 25 shows a typical profile for the inhibitor fraction at one value of incident energy along the z axis in the resist and figure 26 the complete inhibitor map. Both curves clearly show the vertical standing wave phenomenon and are in very good agreement with published results [Ref.118].

A listing of the program HOLOGRAM accompanied with comments is given in appendix 2.

D.4) Program handling:

It will be seen that the program can easily be amended to cater for "substrate structures" of a more complicated nature than the silicon/silicon nitride configuration that has been adopted. When prompted for the characteristics of the input medium (refractive index), it is equally simple to enter the optical properties of air or any solid or liquid prism, thus is the front prism technique dealt with.

Figure 27 shows in a schematic fashion the simulation of holographic exposure by the computer. In order to illustrate the use of such a program in the fabrication of gratings an example is taken. The multilayer system investigated is shown in figure 28. The selection procedure is as follows:

-Given the goal in terms of pitch Λ and grating thickness u, aiming for an undercut profile, the following two equations allow for a rapid choice of the angle of incidence θ_r in the resist (figure 29) and of the ratio resist index/wavelength (figure 30):

$$\Lambda = \lambda/(2n_r \sin\theta_r) \qquad (76a)$$

DATA SET:

Input medium index:	1.0
Photoresist index:	1.7
Dielectric index:	1.49
Silicon index:	5.613-i0.19
Resist thickness:	800 nm
Si_3N_4 thickness:	50 nm
Wavelength:	404.7 nm
Angle of incidence:	45^{o}
A, B, C:	0.8, 0.07, 0.018
Incident energy:	60 mJ/cm^2

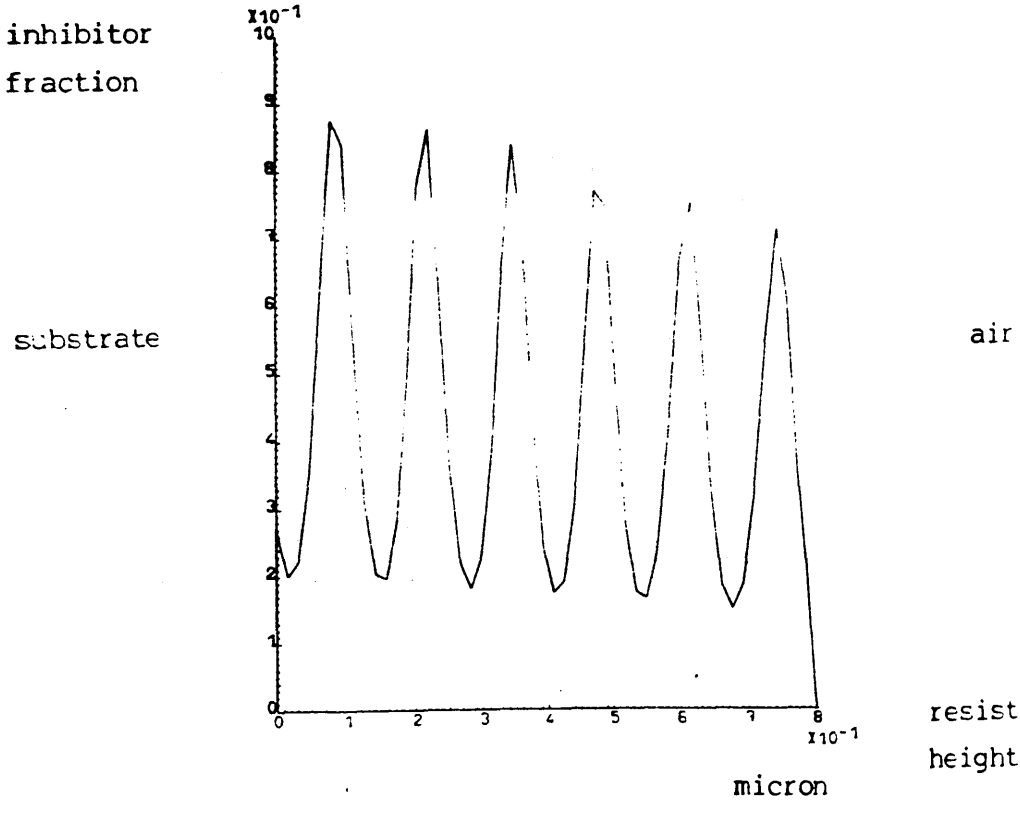

Figure 25: Inhibitor vertical profile showing the standing wave pattern.

Data set presented in Figure 25

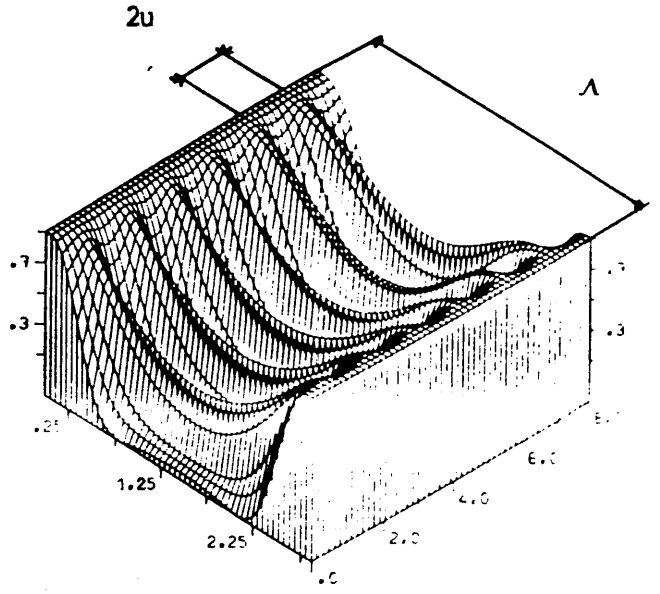

horizontal displacement
covering one whole grating
pitch in 10^{-1} microns.

depth into photoresist
in 10^{-1} microns

Figure 26: Bleached resist map output by BOLOGRAM and fed to SAMPLE.

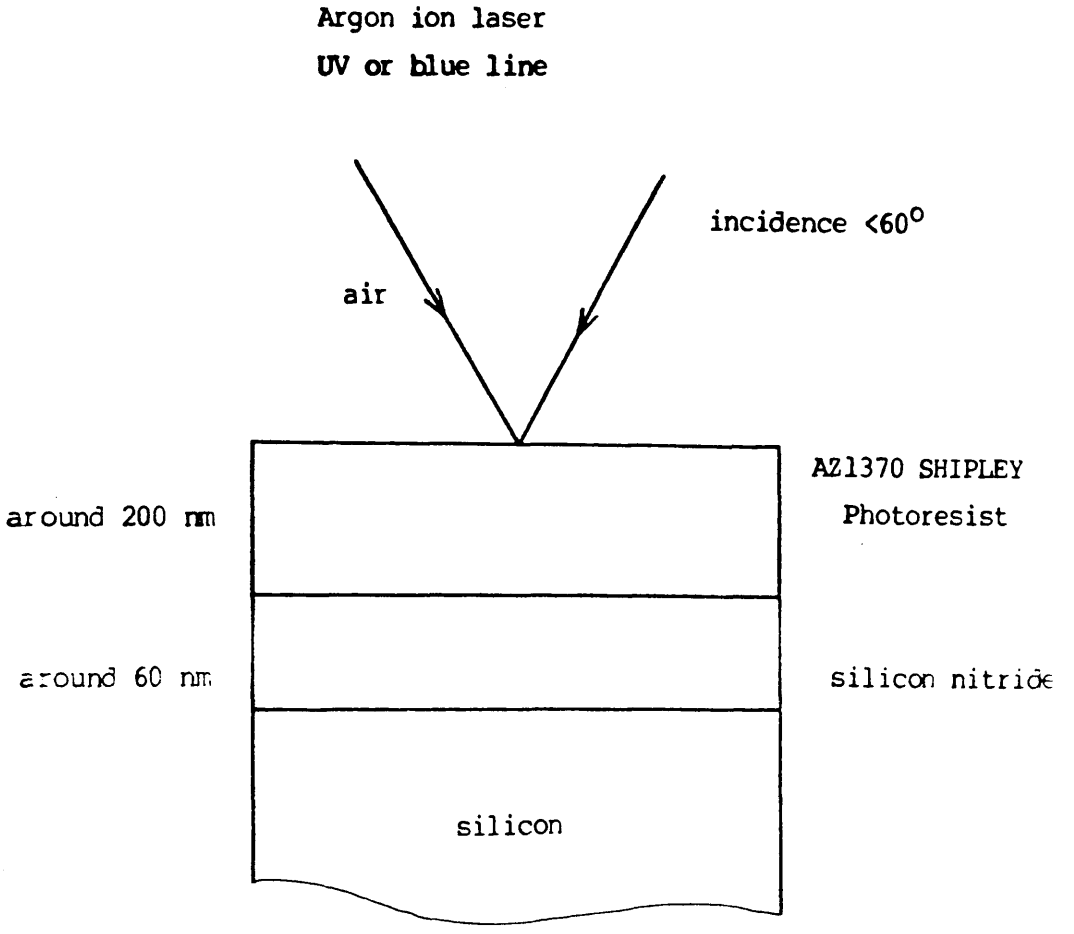

Figure 28: Experimental system.

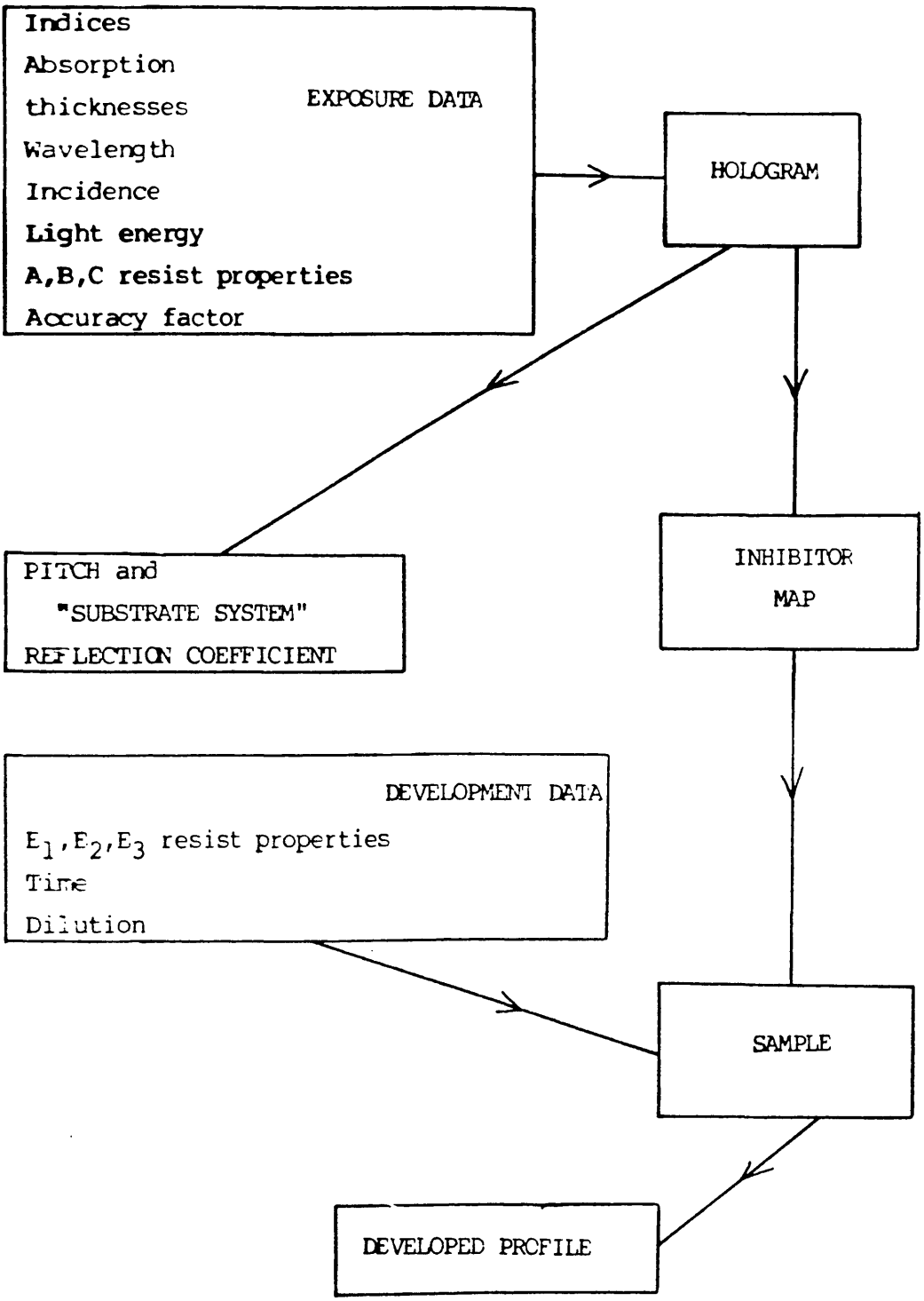

Figure 27: Program organisation.

Contour height
θ_r in degrees.

Grating pitch
Λ in 10^{-1} microns

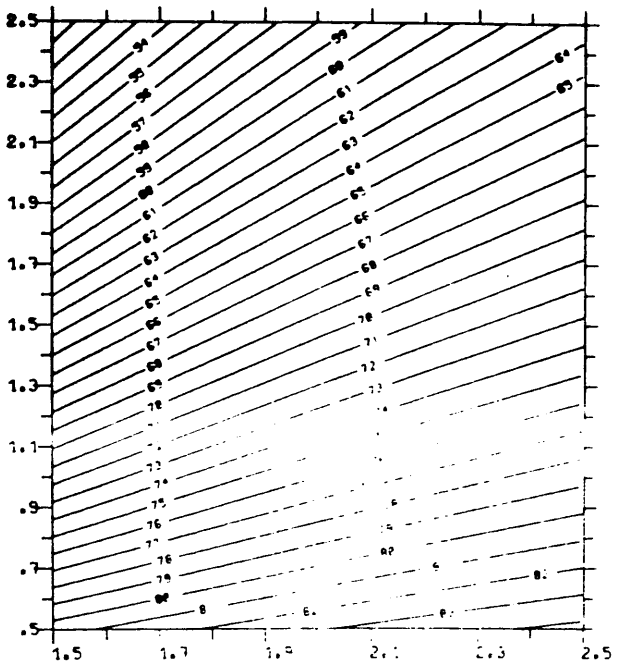

Resist thickness
u in 10^{-1} microns

Figure 29: Wave angle in the resist against pitch and resist undercut height.

Contour height: n/λ

Contour step: 0.25

Grating pitch
Λ in 10^{-1} microns

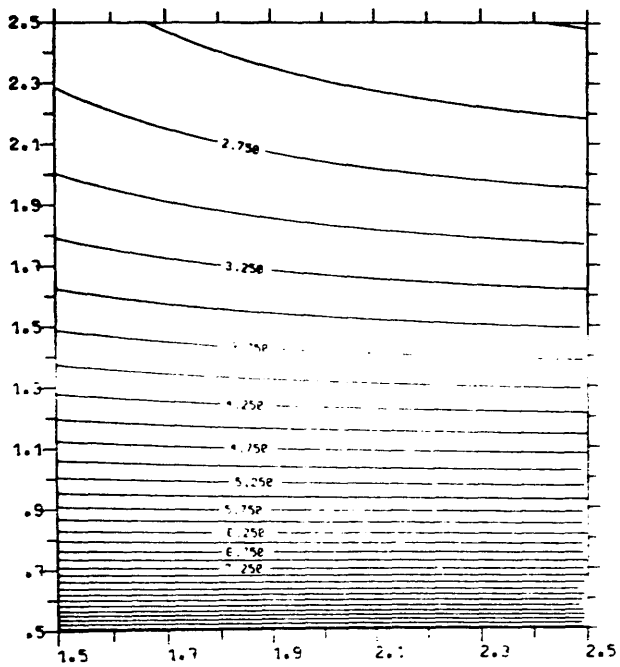

Resist thickness
u in 10^{-1} microns

Figure 30: Ratio n/λ against pitch and resist undercut height.

$$2u = \lambda/(2n_r \cos\theta_r) \qquad (76b)$$

or

$$n_r/\lambda = 1/2\left[1/\Lambda^2 + 1/(2u)^2\right]^{1/2} \qquad (77a)$$

$$\theta_r = \tan^{-1}(2u/\Lambda) \qquad (77b)$$

where real valued indices have been used for simplicity.

-A simple calculation (using SNELL's law) easily leads to the angle of incidence to be set on the optical bench, once a photoresist presenting an adequate ratio n/λ has been chosen.

-The next step consists in finding a suitable Si_3N_4 thickness for an undercut profile to occur. In order to do so, provision has been made for the program to output the complex reflection coefficient at the resist/nitride interface (reflection ratio and phase shift); and different values of the experimental conditions (especially Si_3N_4 thickness) are tried out for a null phase shift leading to a maximum of intensity at the interface and therefore producing an undercut profile [Ref.67].

-The last step involves running the whole simulation (HOLOGRAM + SAMPLE) and determining by trial and error the exposure and development characteristics. At the end of such a computer simulation, one is in possession of an optimal set of experimental conditions for the fabrication of a grating (Λ,u) with undercut profile.

D.5) Conclusion:

A reliable tool has been fabricated allowing us to determine the most suitable experimental environment in order to satisfy our holographic requirements which are mainly pitch and line profile requirements. Provision has been made within the program to allow for a rapid adjustment of the intermediate layer thickness (Si_3N_4 in our case) to arrive theoretically at the undercut case (i.e. zero phase shift at the interface Si/Si_3N_4).

An experimental solution to the same problem has been obtained by N.N. EFREMOW et al. [Ref.67].

There is however a lack of data on photoresists and on materials such as silicon nitride concerning direct measurements of their optical constants at wavelengths different from the usual mercury line (404.7 nm) or helium-neon laser (633 nm). There is indeed a need for such data (optical characteristics and A, B, C coefficients for the photoresist) at UV wavelengths for the obtention of small pitched gratings (around 0.15 micron) with undercut line profile by using a UV laser on the holographic arrangement is highly desirable. The undercut line profile is a very important characteristic of the resist grating as it renders a further metal lift-off operation more likely to succeed. Following the above remark a few optical constants measurements were taken at a UV wavelength of 351.1 nm. Such measurements are reported in the next part (part III) along with a comparison between computer predicted and experimental line profiles (where possible) and it will be seen that the computer program gives a fair account of the holographic exposure phenomenon.

PART III

EXPERIMENTAL WORK

Grating fabrication with line profile control.

INTRODUCTION

The following part is a report on the experimental work carried out. Even though the goal was to ultimately make a X-ray mask as described in Figure 12, there also was the ambition to achieve a recording with line profile control of gratings with a pitch of 0.1 micron.

Section A reports preparatory experiments undertaken, e.g. index measurements in the UV, so that the computer simulation could be run for UV holographic exposure. Section A also ends by listing the characteristics of the materials used, either inferred from existing literature or measured experimentally. The sample preparation procedure is also described along with the alignment technique for the holographic setup.

Section B, presents the fabrication of gratings, different experimental environments, and the results compared with the corresponding simulation where possible.

Finally a discussion exposes the encountered difficulties and the suggested solutions. A line of progress for further experiments is also proposed.

A: PREPARATORY EXPERIMENTS

The optical properties of silicon, silicon nitride and photoresist have been established experimentally where possible or inferred from literature when the experimental procedure was inaccurate. The sample preparation procedure is also presented before a thorough description of the holographic arrangement and the alignment procedure are exposed.

A.1) "Substrate system" properties:

Three inch wafers of silicon/silicon nitride were obtained from the SERC Microfabrication Facility at EDINBURGH University. The nitride layer was grown to our specifications by Chemical Vapour Deposition and the quality was found to be generally good, of uniform thickness and with very few pinholes. Some batches which showed defects were used as trial samples for determination of exposure and development times.

A.1.1 Thickness measurements:

When ordering the Si_3N_4 coated silicon wafers, the nitride thickness was specified within a few nanometres of the value chosen by computer simulation for an undercut profile to occur. Thickness measurements were carried out on the sanples using a "GAERTNER L117" ellipsometer fitted with a helium-neon laser (λ=633 nm). Five measurements evenly spread on each of the wafers showed uniformity in the nitride layer thickness and values close to our specifications (within a nanometre).

A.1.2 Index measurements:

In order to run a simulation for holographic grating printing at UV wavelengths, it is important to know the characteristics of the employed materials. Therefore measurements were made of the refractive indices of silicon and silcon nitride at a wavelength of 351.1 nm (UV line for the argon ion laser). The ABELES method, first tried out, consists of measuring the BREWSTER angle of the medium linked to its refractive index by a simple equation. However the experimental setup used was found to be inaccurate,

partly due to the method itself as it consists in finding a very flat extremum, and partly due to the silicon detector used which exhibits an increasing response to UV light with time and presents a memory effect. The poor quality of silicon detectors at short wavelengths has been reported on previous occasions [Ref.119]. It was therefore decided to construct a UV ellipsometer with a photomultiplier tube for its light detector.

A.1.3 UV ellipsometer:

The design of the ellipsometer was inspired by R.J. ARCHER [Ref.120] and its principle is outlined in figure 31. The argon ion laser UV doublet was separated by a prism and the 351.1 nm line was used. There are cases of incidence when the reflection of an elliptically polarised beam on a thin film coated substrate is plane polarised. Measurements of the ellipticity of the incident wave when such a phenomenon occurs allow the determination of the refractive index and the thickness of the thin film.

A combination of compensator-polariser-compensator, figure 32a, was used to select any state of elliptical polarisation of the UV laser beam. Angular readings could be taken on the polariser and its origin was set perpendicular to the plane of the examined sample as suggested in [Ref.120]. The reflected beam goes through an analyser, figure 32b, of which angular readings could also be taken, before its intensity is measured by a photomultiplier detector connected to a lock-in amplifier (the light was chopped at 1 kHz in order to avoid measuring any noise in the system). The experimental setup, figure 32, is used as a classical ellipsometer, two zero readings were carried out providing two sets of angles (polariser, analyser) for which the reflected wave is plane polarised and linked by simple equations to the characteristics Ψ (amplitude ratio) and Δ (phase difference) of the incident beam. Knowing those two quantities, the DATA conversion software accompanying the "GAERTNER" ellipsometer allowed us to calculate the refractive index, the absorption coefficient and the thickness of the tested material.

A.1.4 Conclusion:

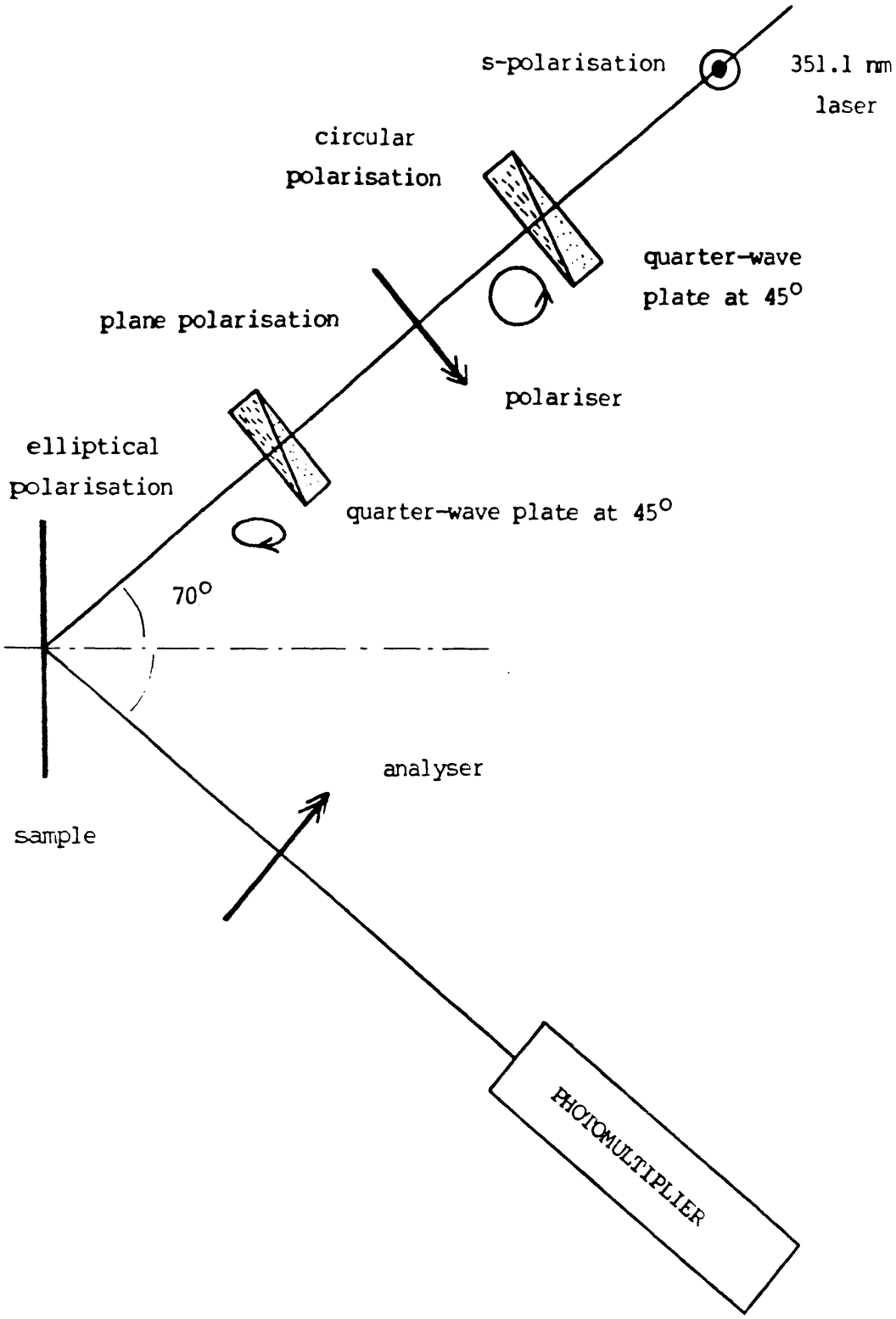

Figure 31: Principle of an ellipsometer.

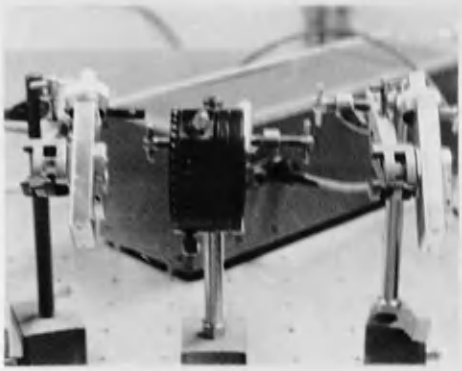

32a

32b

polariser arm

analyser arm

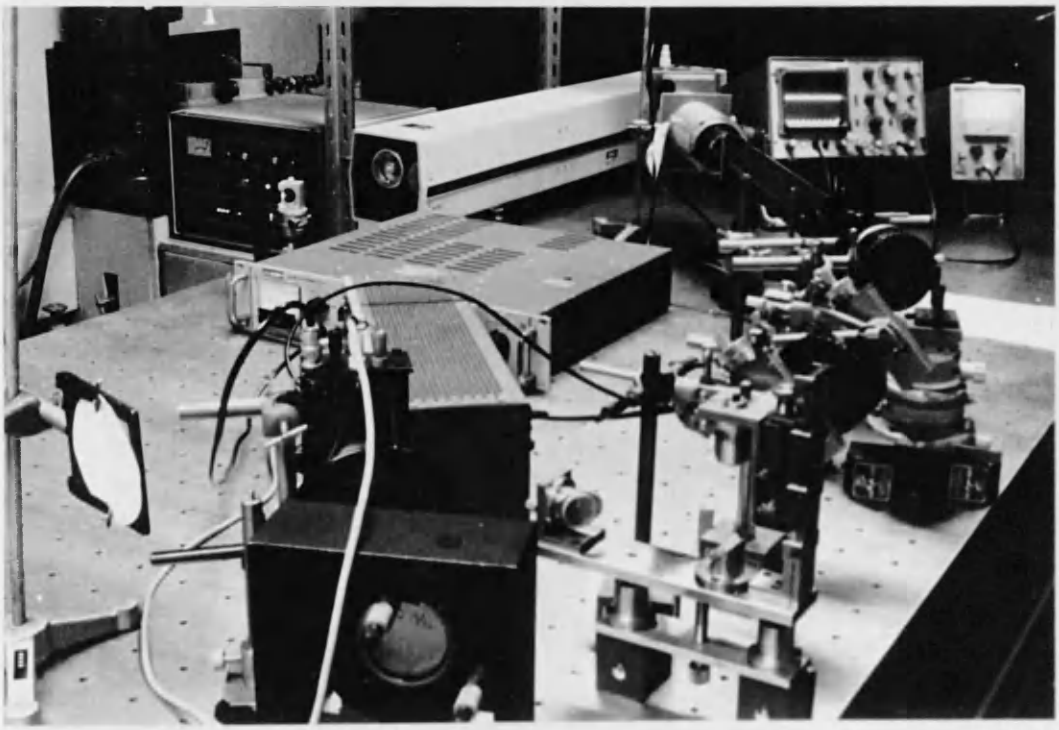

Figure 32: The ellipsometer arrangement.

Measurements carried out on a sample of silicon gave the following results:

$\hat{n}_{Si} = 5.4 - i3.1$ at $\lambda = 351.1$ nm

These figures are in good agreement with data obtained by other methods [Ref.121].

The measurements carried out on the Si/Si_3N_4 samples led to the following results:

$\hat{n}_{nit} = 2.18$ at $\lambda = 351.1$ nm

No absorption was noticed and the measurements were also in good agreement with reported values [Ref.122]. Moreover, the thicknesses of the silicon nitride films calculated from measurements using the UV ellipsometer were found to be similar to those calculated from measurements using the "GAERTNER" ellipsometer.

A.2) Photoresist properties:

It was observed on the computer simulation plots that localisation of a maximum of light intensity at the interface resist/Si_3N_4, and therefore the occurrence of an undercut profile, depends heavily on the optical and geometrical characteristics of the substrate system. This is why accurate measurements were needed and carried out on the Si/Si_3N_4 system. On the contrary, it was also observed that a certain latitude (10^{-2}) on the resist index could be tolerated, which only slightly affected the height and the shape of the undercut profile.

Index measurements were taken for the resist; those showing accurate values were kept, while those showing discrepancies were discarded and a value was extrapolated from measurements at other wavelengths known to be accurate. Our aim was to bring the simulation to its closest approximation of the real phenomenon without becoming too involved in difficult and lengthy refractive index measurements.

The choice of the photoresist has been dictated by the following expression, "$n\sin\theta$", which occurs in both the grating pitch formula (equation 18) and SNELL's law (equation 55), signifying that the smallest pitch achievable in a multilayer system is determined by the lowest index medium. This justifies the choice of a high index resist, particularly if the front prism technique is used.

A.2.1 Resist index:

Among the resists marketed by SHIPLEY, AZ1370 was found to present the highest refractive index. Indeed, index measurements reported in [Ref.100] exhibit a value of:

$$n_{AZ1370} = 1.91 \qquad \text{at } \lambda = 325 \text{ nm}$$

Measurements were carried out at $\lambda = 351.1$ nm but the results showed too much discrepancy while numerous ellipsometric measurements at $\lambda = 457.9$ nm showed consistent values of:

$$n_{AZ1370} = 1.817 \qquad \text{at } \lambda = 457.9 \text{ nm}$$

As justified earlier, the resist index value in the UV was extrapolated from the two values exposed above. It was thought that at a wavelength coming close to the absorption edge of the resist material, a linear approximation would be too inaccurate. This is why a parabolic interpolation was used, which lead to:

$$n_{AZ1370} = 1.89 \qquad \text{at } \lambda = 351.1 \text{ nm}$$

A.2.2 Resist bleaching properties:

As outlined in II.D.2, the bleaching properties of positive photoresist can be expressed in terms of 3 constants A, B and C, and the absorption part of the complex refractive index of the resist is linked to these constants (equation 74). The use of inaccurate values for these coefficients in the computer simulation affects the indications on the exposure and development times and the line profile but, whether an undercut does or does not occur depends on the refractive indices and

thicknesses of the materials and not on the resist absorption properties. An experimental set-up for the determination of A, B and C is presented in [Ref.104] and values for these coefficients are given at different wavelengths. Stated values were used at λ=365 nm for the simulation at λ=351.1 nm and at λ=435.8 for simulation at λ=457.9 nm.

A.2.3 Resist thickness:

Glass slides were cleaned and spun at different speeds with AZ1370 diluted to various ratio so that the photoresist thickness dependence on these parameters could be determined. The resist film thickness was further measured using a TALYSTEP instrument and the obtained graphs are presented figure 33.

A.3) Sample preparation:

All samples preparation was carried out under dust free conditions in a class 100 clean-room tunnel and all the chemicals used were of ANALAR quality.

A.3.1 Sample cutting:

The three inch silicon nitride coated silicon wafers were cleaned in acetone, rinsed in deionised water and blown dry. They were left to completely dry for about an hour on a hot plate (at 40 to 50^{o}C) after which time they were coated with a protective layer of undiluted photoresist (2.5 micron thick) and left to dry for 5 minutes. The wafers were then cut into nine 19*19 mm square samples using a diamond scriber and cleaving them along the scribed lines.

A.3.2 Cleaning procedure:

After the resist protective layer had been dissolved in acetone and the samples rinsed in deionised water, the cleaning procedure was as follows:

a) Scrub with liquid soap and a small sponge held in a hemostat clamp starting with the polished side and finishing with the rough side of the samples. A new piece of sponge was used for each sample.

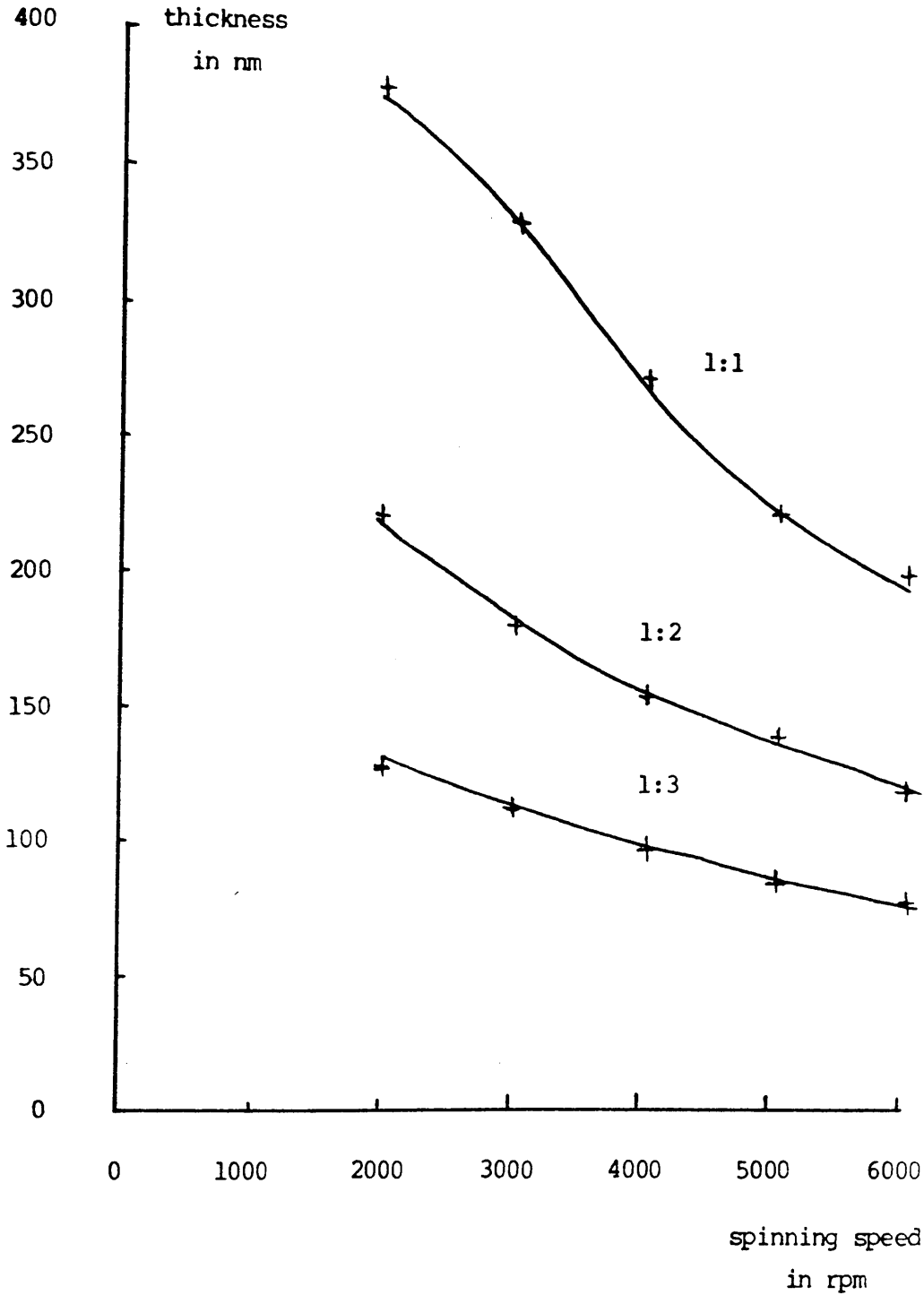

Figure 33: AZ1370 thickness versus dilution and spinning speed.

b) 10 minutes in soapy water.

c) Rinse in deionised water for 10 minutes.

d) 10 minutes in an acetone bath.

e) Rinse in deionised water for 10 minutes.

f) Rinse in ultrapure water for 10 minutes.

g) The samples were then blown dry one by one with filtered nitrogen and left on a hot plate (40 to 50^{o}C) to dry further for an hour.

All the stages but the first and the last were carried out in an ultrasonic bath and care was taken to keep the samples vertical so that any dust particles would fall to the bottom of the receptacle. A rinse under running deionised water was carried out between each stage while transferring the samples, one at a time, from one bath to another. The various dishes and holders used were thoroughly cleaned before and between stages. The usual precautions were also observed such as:

-Keeping the samples between the laminar airflow and the manipulator.

-Using a lid on the receptacles except when transferring the samples between bathes.

It was found that if all these precautions were observed, the samples were of absolute cleanliness and free of particles to such an extent that it was difficult to find a speck of dust on the surfaces that could be used as a focussing aid under the electron microscope.

A.3.3 Resist coating:

The next stage consists in coating the samples with a thin layer of photoresist (less than 200nm). In order to obtain

sufficiently thin coatings, the photoresist was diluted in a ratio of 2 parts of thinner to 1 part of resist. Resist preparation was handled under ultra-clean conditions and specialy cleaned equipment was used throughout, the dilution being carried out using precision measuring cylinders.

The photoresist was dispensed on the samples from a hypodermic syringe to which was attached a 0.2 micron filter. The samples were entirely covered with photoresist before being spun for 20 seconds at speeds ranging from 2000 to 6000 rpm depending on the desired thickness. The coated samples were then postbaked at 83°C in air for 30 minutes. When ready for exposure, the samples were stored under light tight and clean conditions until they were used on the holographic setup.

The colouring of the samples, due to the thin film of resist, was found to be uniform thus showing good uniformity in the resist thickness. Only at the very corners of the samples were changes in the colouring observed where the resist film was thicker. When using the front prism technique, the resist could be removed at the corners by dipping into MICROPOSIT resist remover.

A.4) Holographic arrangement:

The experimental set-up was arranged on an EALING optical table mounted on an air bed and housed under a temperature controlled ($\pm$ 1°C around 23°C) positive pressure tent. It was found that under such conditions the air surrounding the holographic setup was relatively clean and that the temperature control provided good stability to the laser cavity length, particularly necessary in the UV where the adjustment of the cavity mirrors was critical.

In order to check the mechanical stability of the table a crude MICHELSON interferometer was set up. The fringe movements showed vibrations of small amplitude (a few wavelengths) induced by the laminar flow units in the laboratory and by the laser cooling water pump. Vibrations of a much greater intensity were also clearly visible during the day when the building was busy

with students and also at times when the road traffic nearby was heavy. It was found that, late in the evening, when all appliances other than the laser water pump had been switched off, and very few people were in the building and there was virtually no road traffic, the fringes showed very little sign of vibration apart from the odd fringe shift every 100 seconds or so. Most of the grating printing was therefore carried out at nightime. Some succes was however obtained when printing gratings in "adverse conditions" but not with such consistancy as when printed at night.

A.4.1 Laser source:

A SPECTRA-PHYSICS Model 164-08 argon ion laser was used throughout and power up to 300 mW was available at λ=457.9 nm, whereas an output of only 9 mW was observed at λ=351.1 nm after the UV doublet had been separated by a prism. All power measurements were carried out using a SCIENTECH thermopile (power and energy meter model 365).

A.4.2 Beam-splitter and mirrors arrangement:

Two different beam-splitters were used to provide an even split of the light at 45^{o} of incidence at λ=457.9 nm for the former and at λ=351.1 nm for the latter. The beam-splitter angle with respect to the laser beam was further adjusted on the bench for equal intensity, with an accuracy of 1%, by monitoring the light intensity in the two beams using a thermopile .

In order to set the redirecting mirrors in a symmetrical way, the following procedure was used:

-The bisector of the two beams was materialised by a red laser beam (a small He-Ne laser).

-A glass slide (GS) mounted on a graded rotational stage was set with its normal axis along the red beam.

-An auxiliary mirror (AM) was used to reflect the red beam back along its own path length as shown in figure 34a.

-The glass slide was then rotated along a vertical axis by half the desired angle of incidence.

-A mirror (RM) was then placed at the intersection of the red and the blue laser beams as shown in figure 34b.

-The glass slide was rotated again towards the other side and another mirror was placed at the intersection of the two beams leading to the configuration shown in figure 34c.

-The red laser was finally removed and the glass slide replaced by the auxiliary mirror adjusted so that both blue beams were of symmetrical incidence, figure 34d.

-Finally the two redirecting mirrors, the beam-splitter and the auxiliary mirror were adjusted along a horizontal axis so as to bring the beams into the same horizontal plane.

At this stage the two arms of the setup interfere strongly and wide fringes can be observed near the beam-splitter and on the laser output window, final adjustments can be made by centering this interference pattern on the beams. When the setup is completely adjusted the sample holder is put in place of the auxiliary mirror.

Both mirrors and the beam-splitter were optically flat to $\lambda/20$, freshly cleaned and relatively free from dust particles.

A.4.3 Spatial filtering:

The next stage in the setting up of the holographic bench consists in adjusting and positioning the spatial filtering units (see IIA.1).

The two focussing lenses (20 mm focal length) were first positioned at equal distances from the sample holder in each arm of the interferometer. In order to do so, two auxiliary mirrors were used to intercept both beams (figure 35) and produce Michelson interference rings visible by the beam-splitter. The

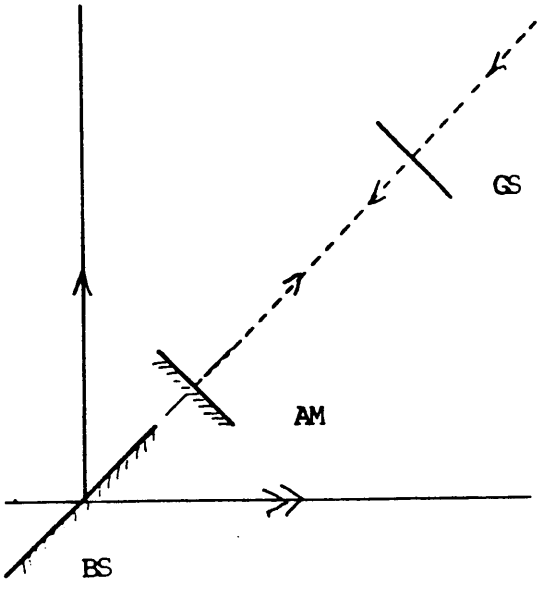

34a

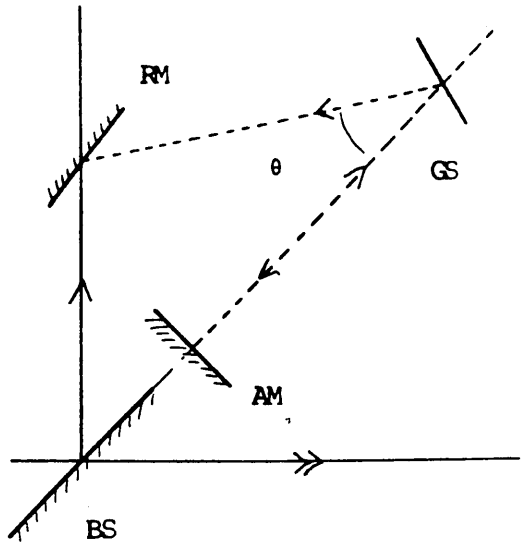

34b

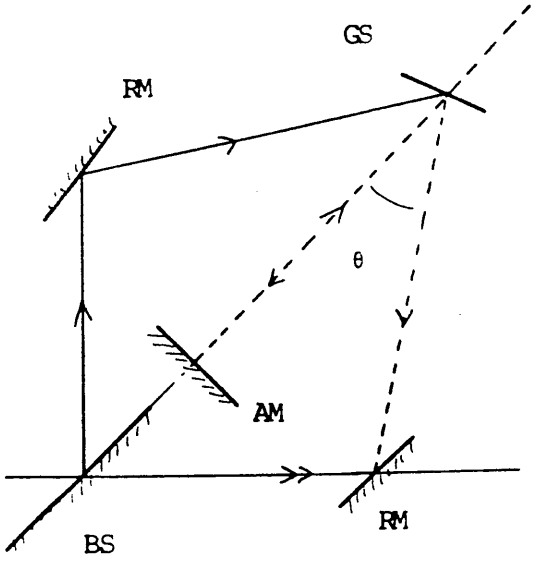

34c

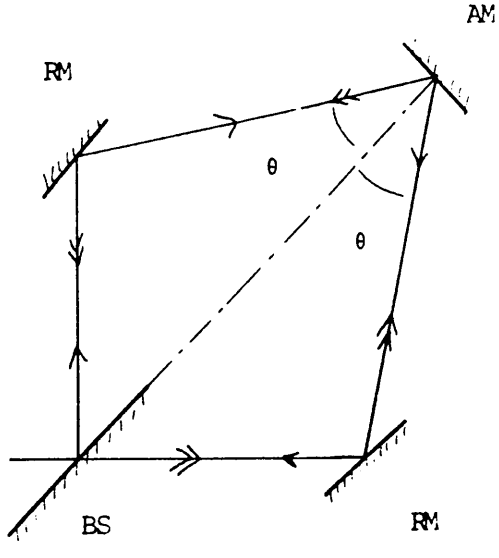

34d

Figure 34: Alignment procedure.
(red beam in dashes)

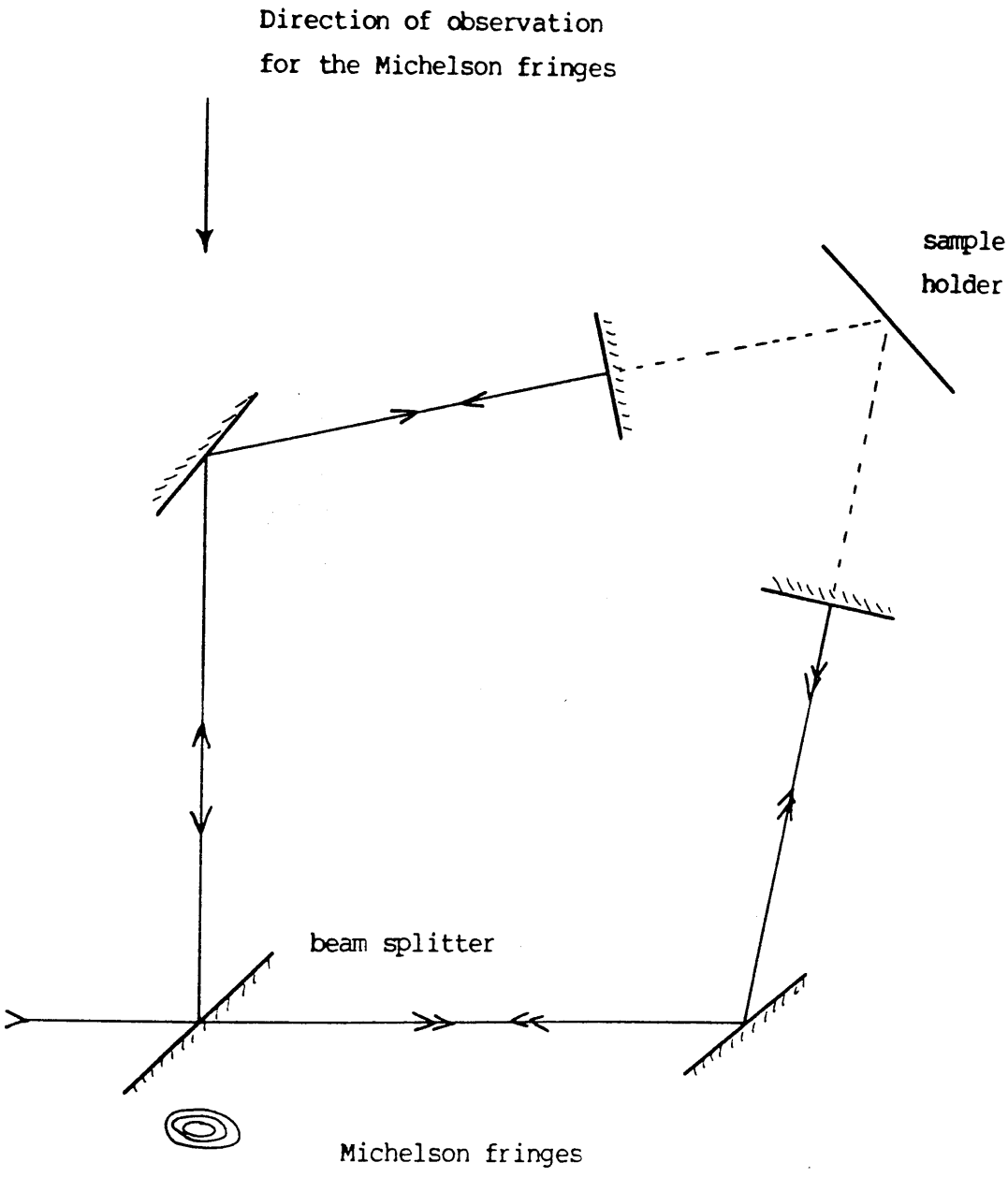

Figure 35: Michelson arrangement for positioning the lenses at equal distances.

mirrors were adjusted by trial and error so that the fringes were as wide as possible indicating a very small path difference between the two arms. The lenses then replaced each mirror and were positioned so that the beams passed through their mechanical centers. Further tilt adjustment of the lenses was carried out by centering the interference rings, visible anywhere on the path of light between the lenses and the laser output window, due to the multiple reflections from the front and the back surfaces of the lenses.

The pinholes were finally placed in the focal plane of the lenses and centered adequately. This is done by observing the diffraction rings generated by the circular aperture of the pinhole. In the past, pinholes of a size up to 20 or 25 microns have been used for the 457.9 nm line and with some success, but it was decided to use 10 micron pinholes as the calculations from IIA3.4 show that they let most of the light through (98 %). It is true nevertheless that the aperture interference pattern was noticeable but the central patch seemed very uniform indeed and the gratings obtained confirmed this observation.

A set of 5 micron pinholes (from AGAR AIDS) were used when the 351.1 nm line was selected but their quality was rather poor, figure 36) and strong distortion could be seen in the filtered beams. Therefore 10 microns pinholes were used throughout the project regardless of the wavelength, even though it is thought that they do not carry out the filtering of the UV light as well as desired.

By moving the pinhole back and forth one can observe the interference rings going inwards or outwards; it was found that when the distance lens-pinhole was such that the central patch appeared at its brightest, a dark fringe was just about to appear in the center of the pattern and the estimated light intensity is shown in figure 37a. This is why the pinholes were slightly "pulled-in" resulting in a more uniform profile across the central patch (figure 37b).

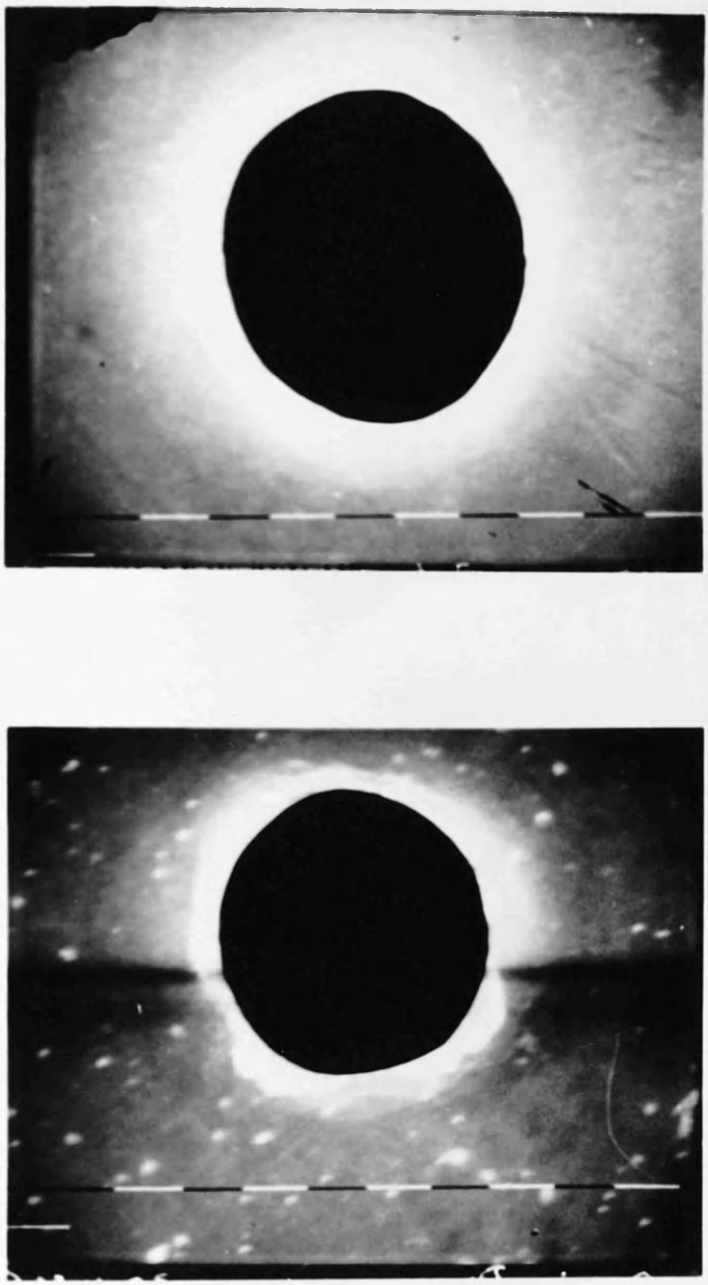

Figure 36: Electron micrographs of the 5 micron pinhole set used with the 351.1 nm line.
(10000 magnification, 1 micron marker)

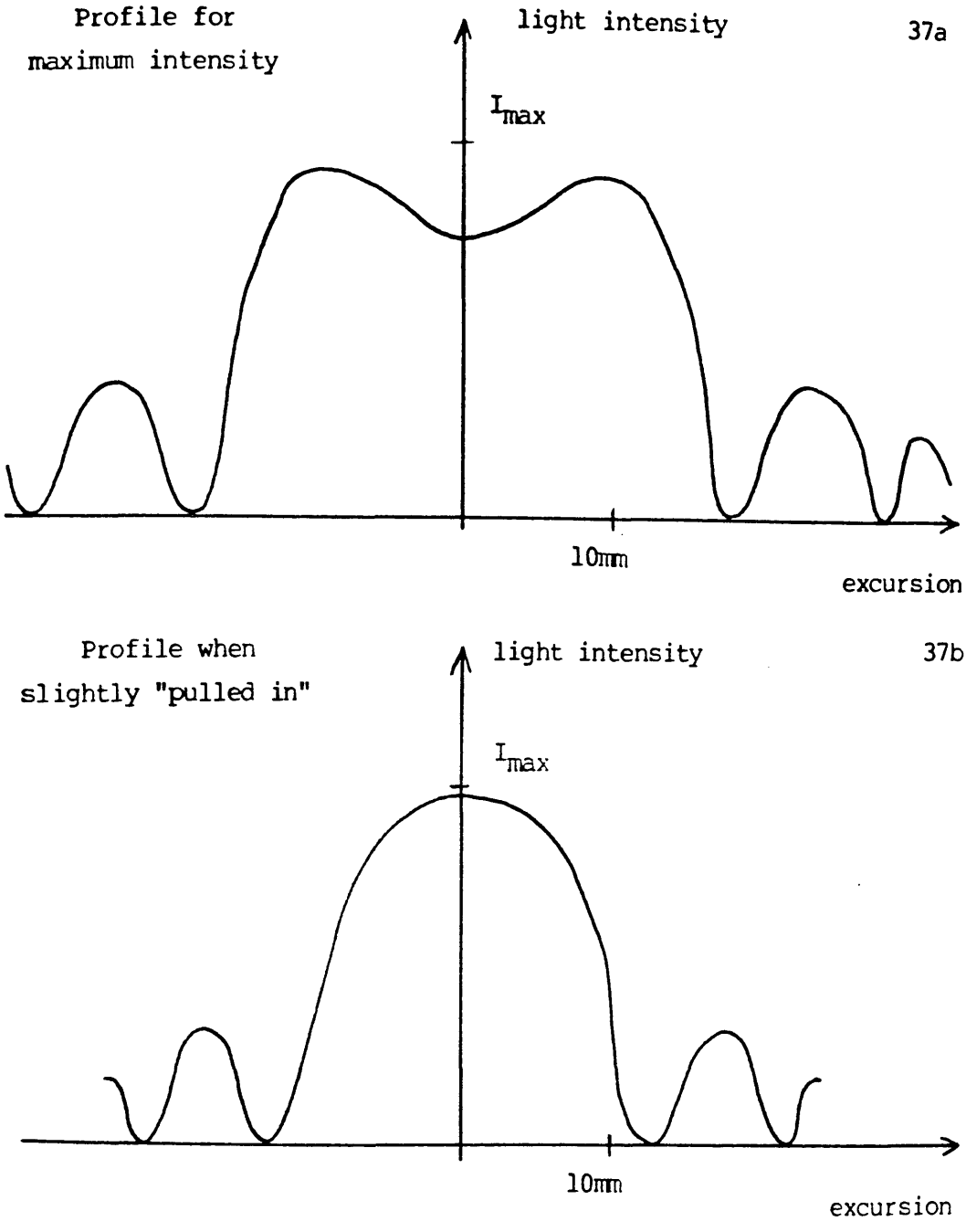

Figure 37: Estimated light intensity profile of the centre patch after the pinholes.

In order to ensure that light intensity at the centre of the patch was maximal, the spatial filter was slightly pulled in (37b) from the position where the patch appeared to be at its maximum width (37a).

Light intensities as high as 2.3 mW/cm^2 were obtained by this method using the 457.9 line, but when the 351.1 line was selected the light intensity values were estimated to be around 30 times smaller.

A.4.4 Sample holders:

Two types of sample holders were used depending on whether the front prism technique was involved or not. In the latter case, a holder was used, shown in figure 38, mounted on a magnetic clamp and onto which the samples were held by suction, the holder being connected to a water jet pump.

However, in order to fabricate very small pitched gratings, the front prism technique was used and the holder (figure 39b) itself was mounted on a three rotational and three translational stage (figure 39a&b). The prisms used were cut from a block of LaSFN31 SCHOTT glass of a very high index (1.95 at 351.1 nm and 1.90 at 457.9 nm) and of relatively high transparency to the UV line 351.1 nm.

The samples were pressed against the back face of the prism by a small pressure chamber (figure 39c) and optical contact occurred between sample and prism in places where a dark patch could be observed. Iodine was occasionally used as a matching index liquid but no improvement on the dry technique was noticed.

The front prism holder could be slid in and out of its stage allowing the loading procedure to be executed in a clean cabinet thus ensuring that no dust particles would be trapped between the sample and the prism.

A.5) Conclusion:

Figure 40 shows an overview of the holographic bench. The samples were exposed to the holographic pattern by remote control, an electric shutter (placed at the laser output window) being activated while all appliances were switched off and with the operator outside the tent.

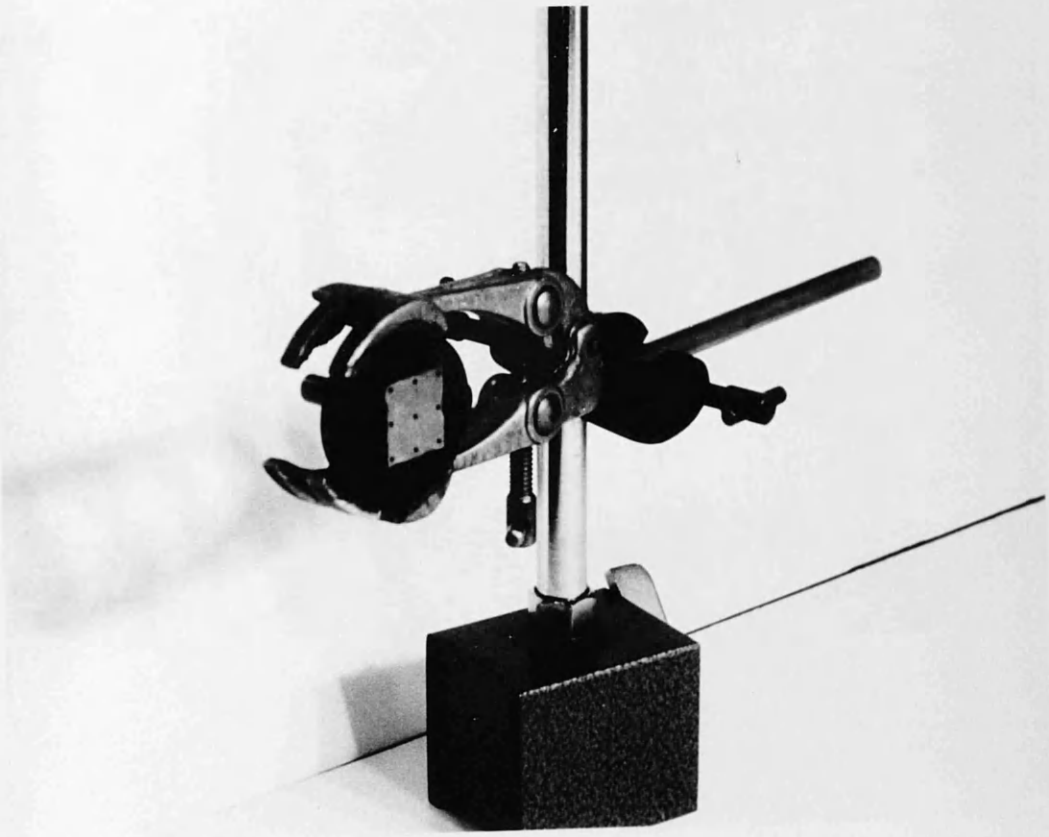

Figure 38: View on the vacuum chuck holder for plain exposure.

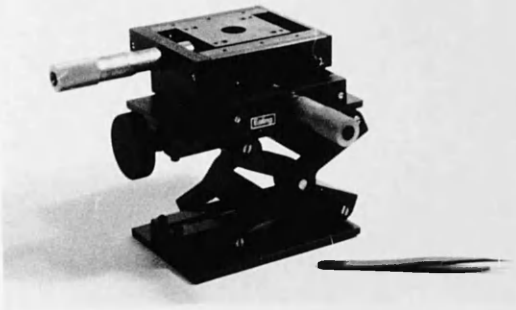

The three translation stage

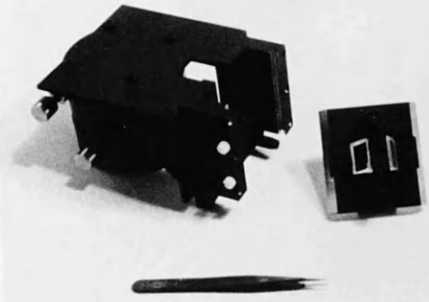

The three rotation stage and the prism holder

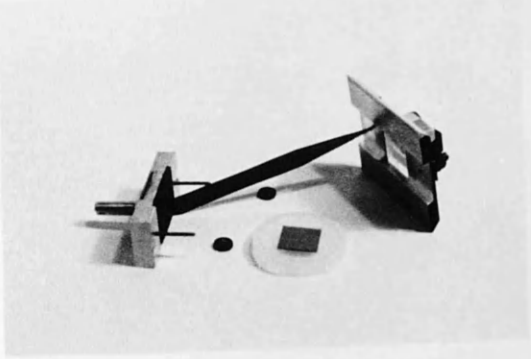

The prism holder
the sample
the back pressure chamber

Figure 39: The front prism technique holder.

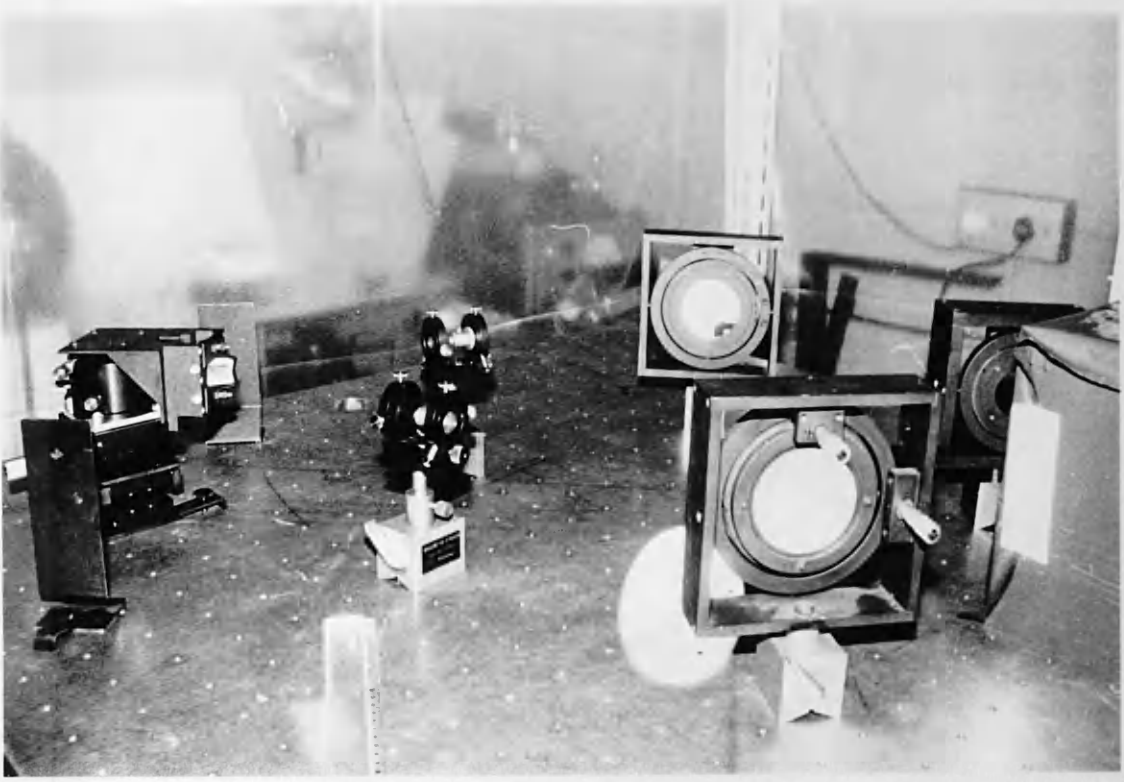

Figure 40: The holographic arrangement.

After they had been exposed, the samples were developed in a clean cabinet with a 1 to 1 aqueous solution of MICROPOSIT developer. The samples were then rinsed in deionised water and blown dry with filtered dry nitrogen.

B: GRATING FABRICATION

B.1 Introduction:

By using the simple two-mirror interferometric arrangement described in the last chapter, well-defined gratings have been produced over large areas by recording the interference pattern arising when the two 457.9 nm laser beams meet on a photoresist coated Silicon Nitride/Silicon substrate.

The computer simulation allowed for the line profile to be monitored so that it would present an undercut when the thickness of the intermediate layer (i.e. Si_3N_4) was adequately chosen.

It is possible to reduce the grating pitch by switching to a shorter wavelength or by reducing it artificially using the front prism technique (FPT). To examine the feasibility of such processes, the UV laser line was selected and the front prism technique was experimented with.

However, success was only partially met within the course of our experimentation and the problems encountered will be discussed in detail. The computer simulation can account for an effect which was seen when samples were overexposed.

B.2 Computer simulation

B.2.1 Silicon nitride thickness:

Using the part of the program HOLOGRAM which allows for a rapid finding of the Si_3N_4 thickness necessary to bring a maximum of intensity at the resist/"substrate system" interface, gave a value of around 60 nm. A certain latitude ($\pm$5nm) could be tolerated without causing an important shift of the reflection coefficient of the substrate system, thus keeping the experimental environment close to the "undercut conditions".

Consequently, three batches of silicon wafers respectively coated with 55, 60 and 65 nm layers of silicon nitride were ordered. Ellipsometric measurements on the wafers gave values of

54.3 nm, 60.9 nm and 74.3 nm respectively. These were then used for the complete computer simulation of the holographic process.

B.2.2 Photoresist thickness:

Simulations were run for various photoresist thicknesses and it was found that when the resist film thickness was less than the vertical standing wave pattern periodicity, the adjustment of the nitride thickness for an undercut profile was not so critical. Each subsequent sample was therefore coated with a 120 nm film of photoresist (1:2 dilution ratio, spun at 6000 rpm) which the computer simulation showed to be an adequate thickness for an undercut profile to be monitored by an extended range of silicon nitride thicknesses.

Examination of the three simulations, respectively shown in figures 41, 42 and 43, shows that when the silicon nitride is 55 or 60 nm thick, the height of the undercut is greater and would therefore be more suitable for lift-off than when the nitride is 75 nm thick.

It is important to ensure that the undercut rises as high as possible, as this height determines the maximum possible thickness of the metal pattern which can be lifted-off successfully.

B.3 Grating fabrication:

Samples of silicon/silicon nitride were exposed to the interference pattern for a time period which ranged from 1 to 10 seconds, and were subsequently developed for 10 to 60 seconds. All the results were consigned in an exposure-development graph which is discussed later. For each set of coordinates (exposure and development times) a letter indicates the quality of the grating recorded within the photoresist layer.

B.3.1 Grating quality assessment:

The quality of the gratings was assessed in two stages; with the naked eye on a macroscopic scale and under an electron beam microscope on a microscopic scale.

Data set:	Air index	1.0
	resist index	1.817
	Si_3N_4 index	2.055
	Si index	4.5-i*1.87
	Wavelength	457.9 nm
	Resist bleaching constants	0.54, 0.06, 0.012
	Si_3N_4 thickness	54.3 nm
	Resist thickness	120 nm
	Exposure intensity	2.3 mW/cm^2
	Exposure time	7 seconds
	Dose decrement	1 mJ/cm^2
	Angle of incidence	45^o
Program output:	Reflection coefficient	0.3955, 12.65^o
	Periodicity	0.33 micron

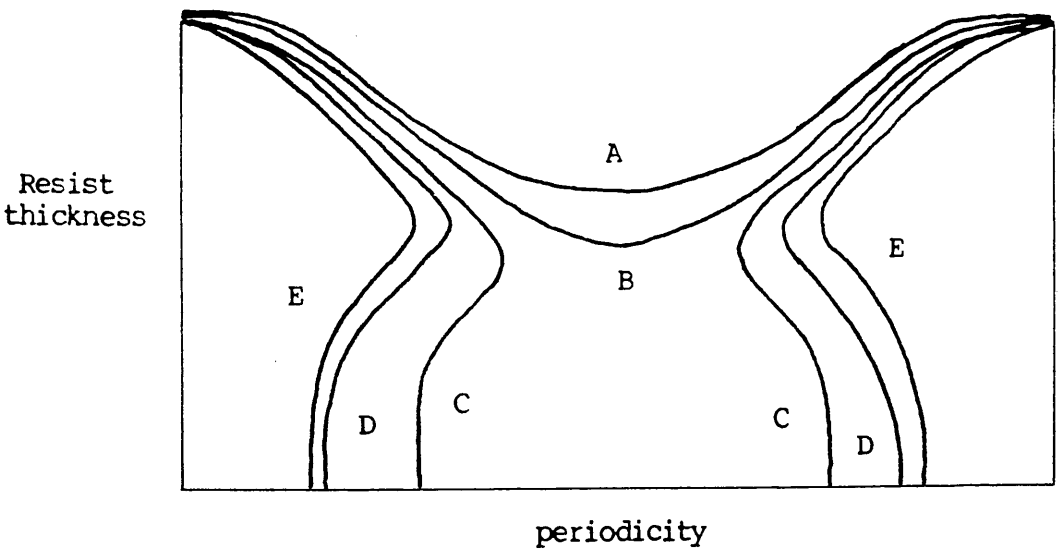

Figure 41: Computer simulation when Si_3N_4 thickness = 54.3 nm.

Development time: A = 10 seconds
B = 15 seconds
C = 20 seconds
D = 25 seconds
E = 30 seconds

Data set:	Air index	1.0
	resist index	1.817
	Si_3N_4 index	2.055
	Si index	4.5-i*1.87
	Wavelength	457.9 nm
	Resist bleaching constants	0.54, 0.06, 0.012
	Si_3N_4 thickness	60.9 nm
	Resist thickness	120 nm
	Exposure intensity	2.3 mW/cm^2
	Exposure time	7 seconds
	Dose decrement	1 mJ/cm^2
	Angle of incidence	45^o
Program output:	Reflection coefficient	$0.3955, -7.32^o$
	Periodicity	0.33 micron

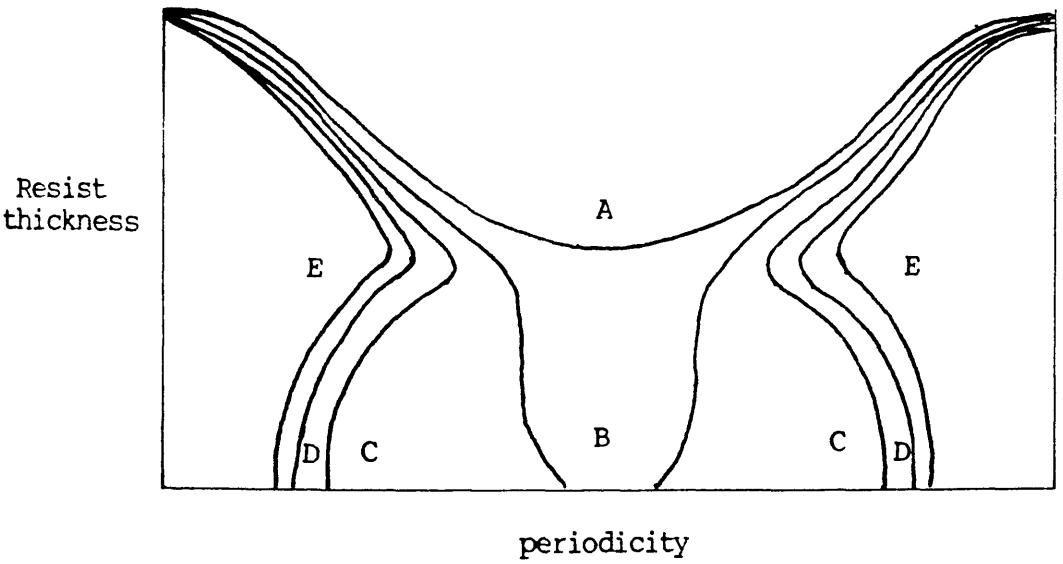

Figure 42: Computer simulation when Si_3N_4 thickness = 60.9 nm.

Development time: A = 10 seconds
B = 15 seconds
C = 20 seconds
D = 25 seconds
E = 30 seconds

Data set:	Air index	1.0
	resist index	1.817
	Si_3N_4 index	2.055
	Si index	4.5-i*1.87
	Wavelength	457.9 nm
	Resist bleaching constants	0.54, 0.06, 0.012
	Si_3N_4 thickness	74.3 nm
	Resist thickness	120 nm
	Exposure intensity	2.3 mW/cm^2
	Exposure time	7 seconds
	Dose decrement	1 mJ/cm^2
	Angle of incidence	45^o
Program output:	Reflection coefficient	$0.3955, -48.03^o$
	Periodicity	0.33 micron

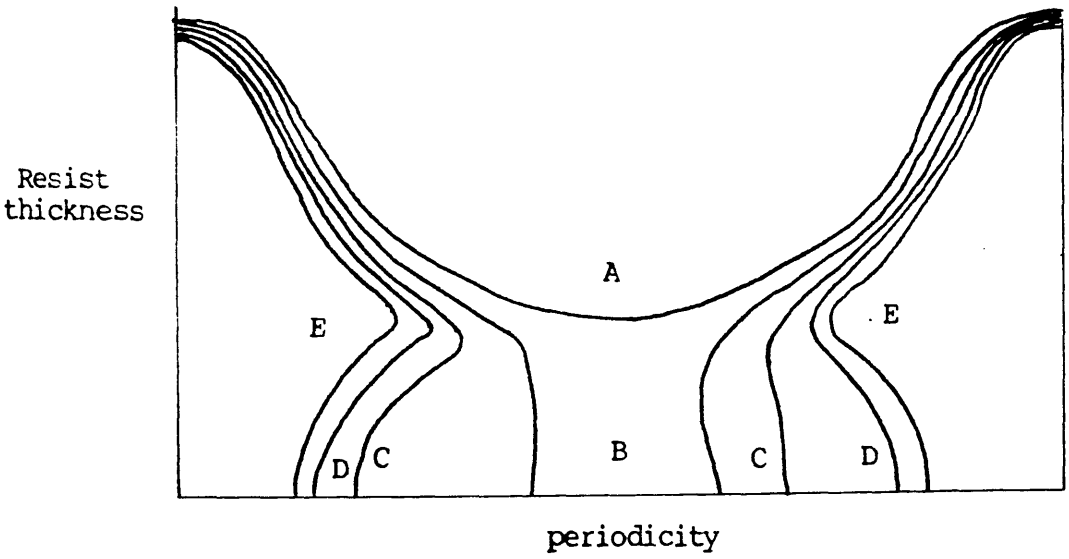

Figure 43: Computer simulation when Si_3N_4 thickness = 74.3 nm.

Development time: A = 10 seconds
B = 15 seconds
C = 20 seconds
D = 25 seconds
E = 30 seconds

B.3.1.1 Macroscopic scale:

The samples were checked for uniformity by observing the colour of the Bragg reflection of white light from the gratings. This is a very sensitive method as a small change in the grating pitch is given away by a colour shift at a given viewing angle. Thus the line spacing of the gratings could be assessed over the whole patch area. After a careful alinement of the interfering beams and a proper adjustment of both the spatial filters, all gratings showed very good uniformity over the fairly large area of the sample exposed to light.

However, although colour shifts were not detectable, and therefore the grating pitch was shown to be uniform, variations of the intensity of the Bragg reflection were noticed from sample to sample, as well as on single samples in some cases. These intensity variations allow for the grating contrast to be assessed, as well as permitting a determination of whether the resist film is continuous or broken into well-defined separate grating lines.

Three different types of intensity distribution were observed:

- A uniformly distributed faint grating over the whole area of the sample.

- On a faint overall grating, a brighter patch could be seen in the centre of the sample.

- Lastly, a bright grating crown, surrounded by a faint grating, enclosed a washed out area where no grating could be seen (figure 44).

B.3.1.2 Microscopic scale:

In order to investigate these variations of intensity as well as to assess the microscopic quality of the gratings, a SEM was used which gave the following results:

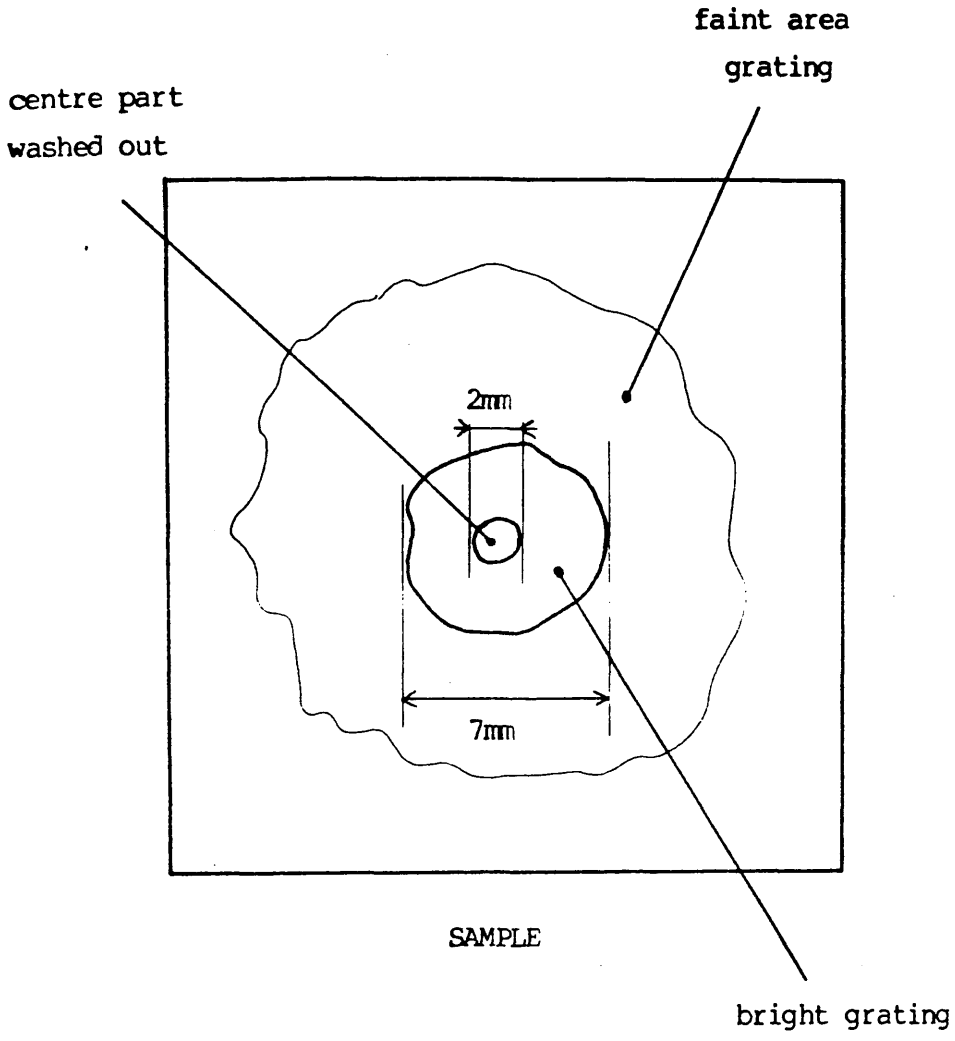

Figure 44: Typical geometry of a UV grating.

- The grating uniformity regarding the pitch and parallel arrangement of lines which could be inferred from the macroscopic observations, was confirmed by the microscopic investigation under the SEM.

- Faint grating regions were found to be areas where the resist was not broken down to the substrate. The resist film was continuous, only presenting corrugations on its upper surface, figure 45 and 46. The poor aspect ratio and the fact that reflections on the photoresist material are low explain why the Bragg reflections arising from such continuous gratings are weak.

- The regions of bright grating showed a resist film which had broken down to the substrate between the lines thus giving a well-defined grating, figure 47. The high aspect ratio and the fact that the light was reflected from the naked substrate between the lines explain why the Bragg reflections from these samples were noticeably higher than in the previous case.

- The washed out areas which could occasionally be observed in the middle of bright grating patches, were found to be absolutely clear of any photoresist material as estimated from the macroscopic observations. These areas have been either overexposed or overdeveloped, or a combination of both.

B.3.1.3 The spaghetti-like effect:

An interesting feature of the junction between bright grating areas and washed out areas is the spaghetti-like effect, as illustrated in figure 48. At first, this effect was thought to be consequent to an adhesion problem which was exacerbated by the narrow base of the grating lines when the sample is overexposed. However, running the computer simulation for overexposed samples simply showed that, not only would the photoresist be broken down to the substrate, but also that the undercut would become so great that a break through the resist wall of a grating line should be expected. The fact that no spaghetti-like effect was observed on gratings presenting an overcut line profile, reinforces the idea that it is not an effect arising from poor

40000 magnification

1 micron marker

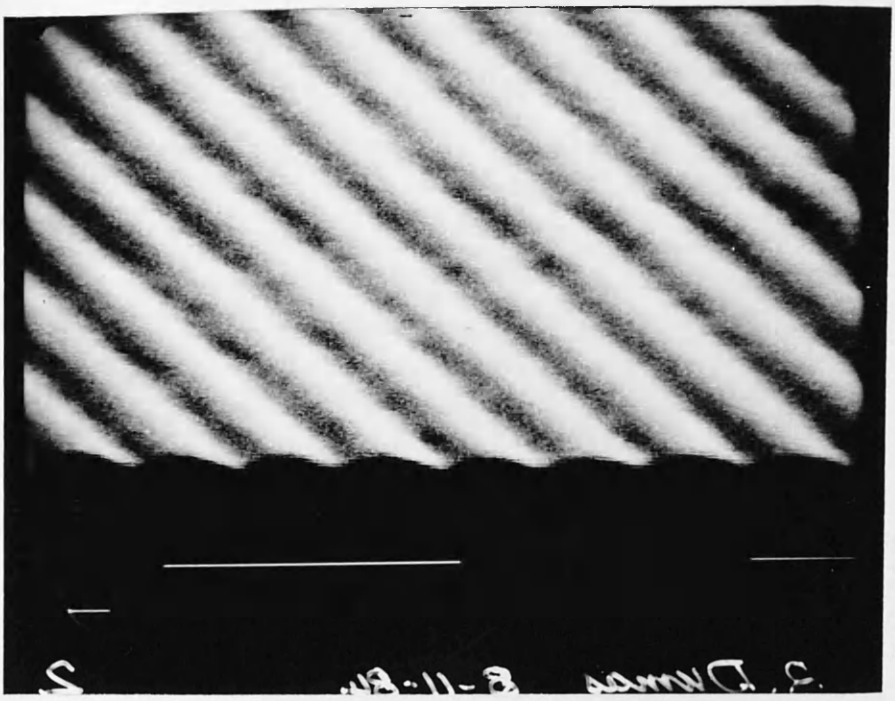

Figure 45: **0.3 micron grating micrograph.**
Exposure and development times are too short, the lines are not cut down to the substrate.

40000 magnification

1 micron marker

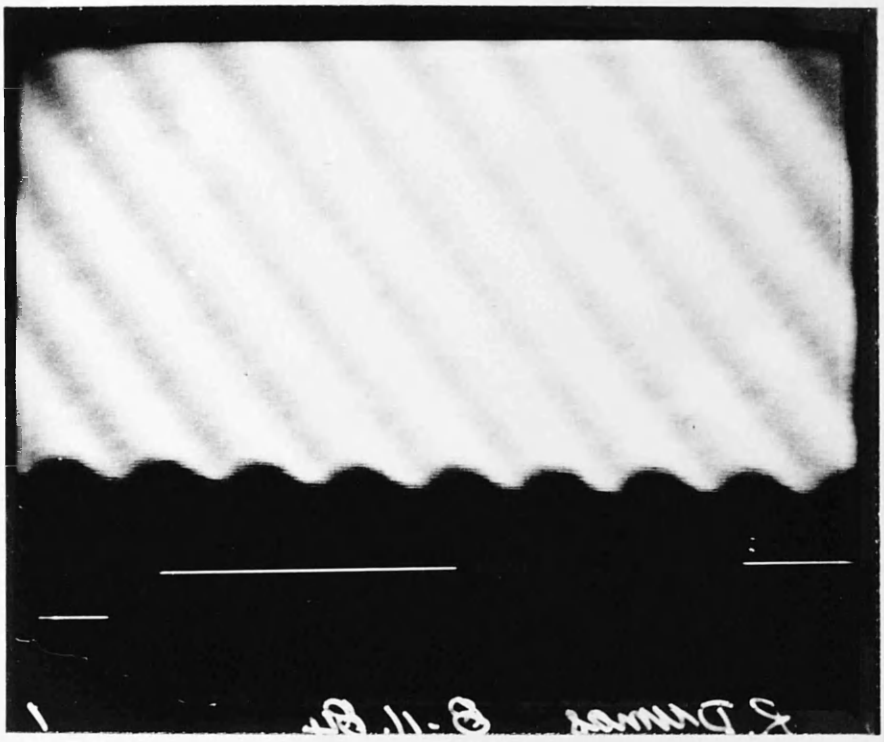

Figure 46: The grooves are deeper but still not cut down to the substrate. Exposure and development times must be increased.

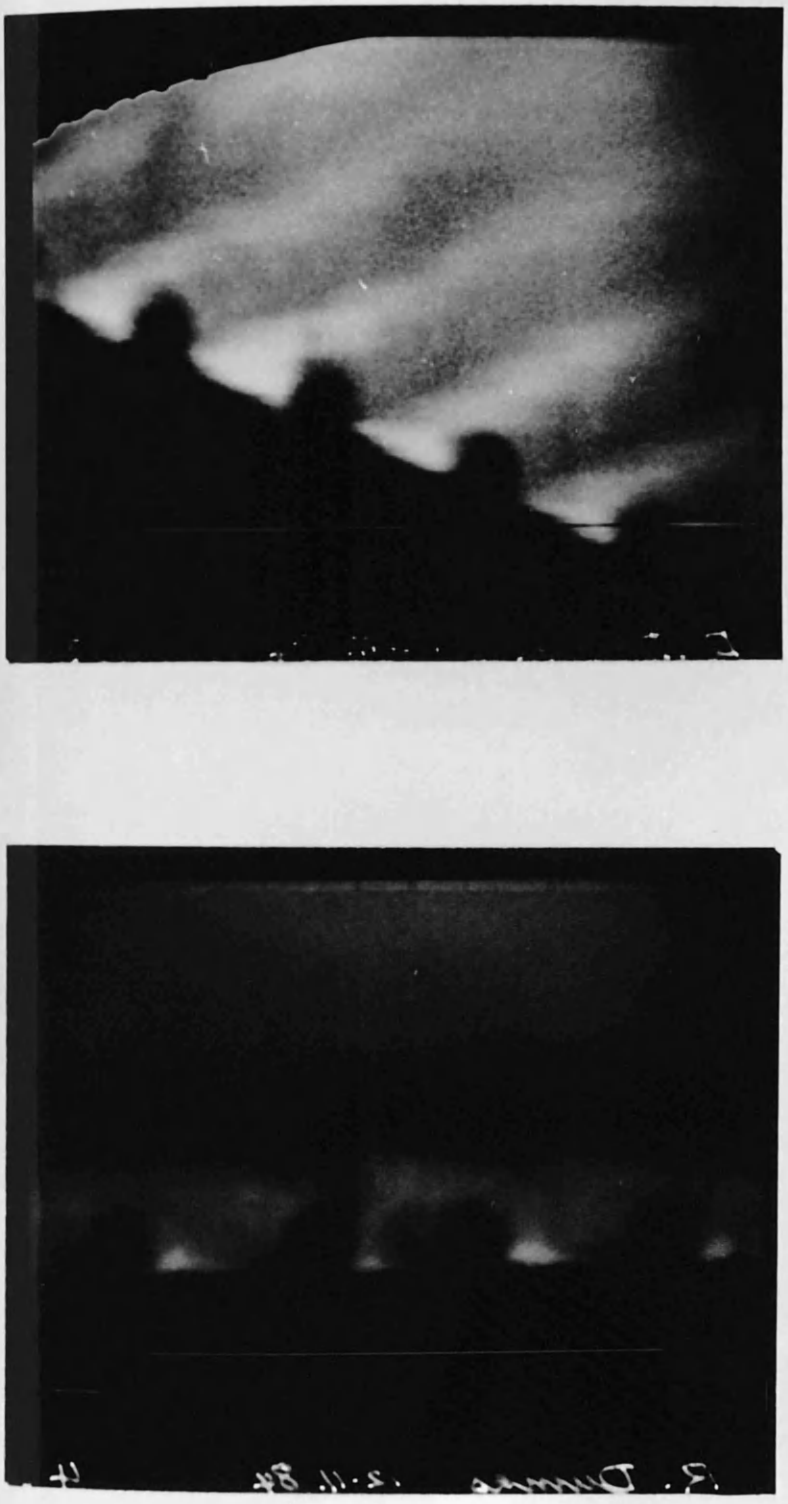

Figure 47: Photoresist grating with undercut line profile.

(Top: 40000 magnification; bottom: 80000 magnification)

1 micron markers

Figure 48: The spaghetti-like effect on a 0.3 micron grating.
(5000 magnification, 1 micron marker)

adherence, and therefore cannot be cured by using any kind of adherence enhancer. The spaghetti-like effect sets a limit on the exposure and development characteristics of the holographic process when an undercut profile is to be achieved, and therefore renders the production of high aspect ratio (thin and tall lines) gratings somewhat difficult.

B.3.2 Exposure and development diagram:

Macroscopic and microscopic investigations were carried out on each exposed sample as explained above.

- All samples that showed a faint grating over its whole area were tagged as underexposed (U).

- All samples that had a washed out central patch were tagged as overexposed (O).

- Samples were tagged suitably exposed (S) when a bright uniform patch could be seen surrounded by a faint overall grating area.

It was also observed that the property of a sample to be underexposed, overexposed or correctly exposed, depended only on the exposure and development characteristics, and not on the Si_3N_4 thickness.

It is inferred from the computer simulation that the silicon nitride thickness would render the spaghetti-like phenomenon more likely to happen when the maximum of light intensity is brought exactly at or above the nitride/resist interface. However, no difference was observed between the three different thicknesses of Si_3N_4 which were used within the course of our experimentation, and this is why only one exposure-development diagram is presented, which includes the results from all samples, figure 49.

B.3.3 Discussion:

Several interesting features of the photoresist film properties concerning development and exposure can be observed in

Dev_{thr}: 30 seconds before breaking through to the substrate
(time to develop away 120 nm of entirely exposed resist)

Dev_{max}: Time to develop 120 nm of slightly exposed resist (M=0.4)

Exp_{max}: M=0. even in the "darkest areas"

Exp_{thr}: Minimal exposure for the resist to develop away (M<0.4)

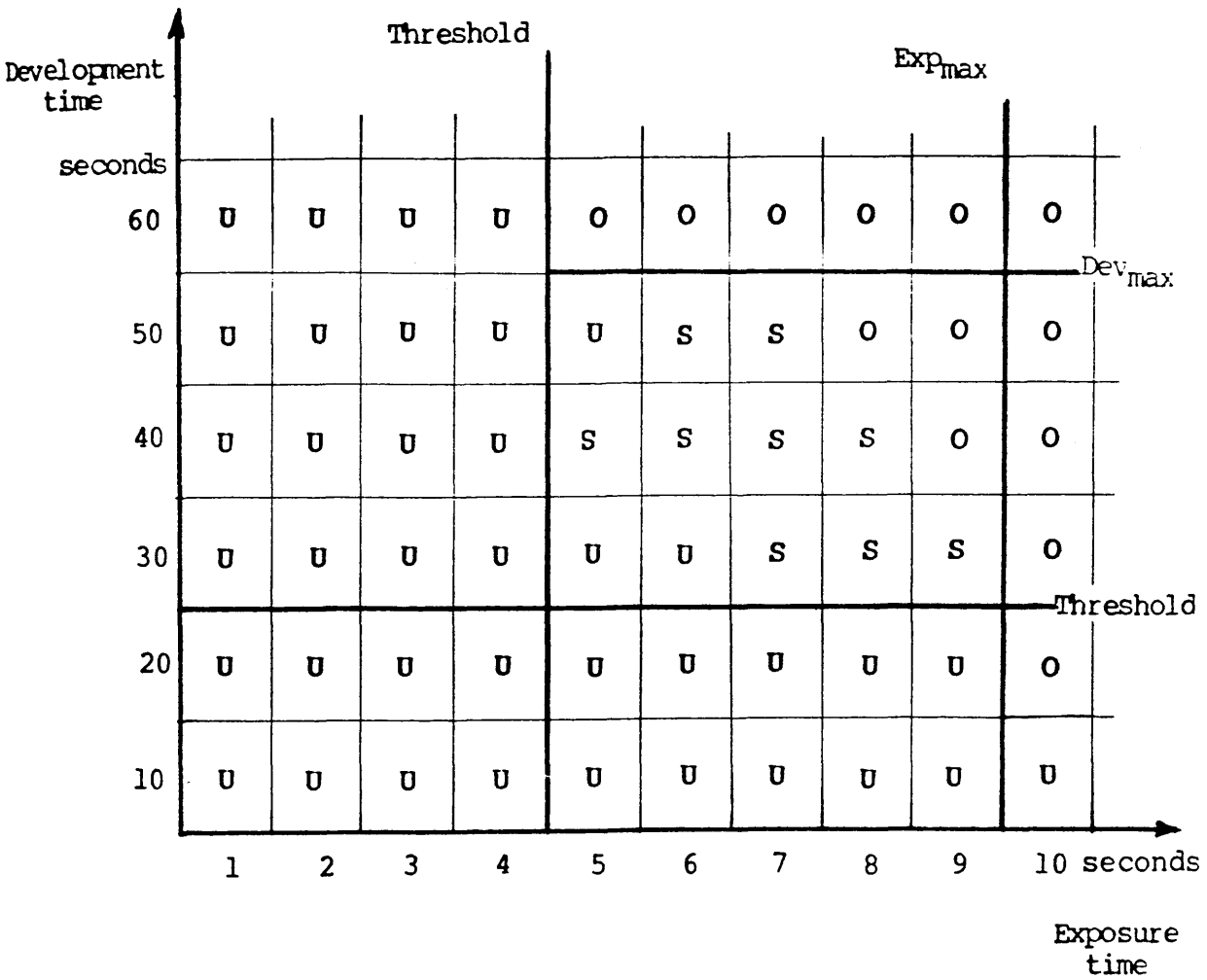

Figure 49: Exposure-Development diagram

U: underexposed
O: overexposed
S: suitably exposed

the diagram.

It can be observed that on all the samples exposed for less than 4 seconds, no grating cut down to the substrate was noticed. Under this threshold value, the light energy is such that, near the interface Si_3N_4/resist, no part of the film presents a remaining inhibitor fraction lower than the development value of 0.4 which is given in the theoretical model [Ref.117].

Not only is there a threshold value for the exposure time but there is also a development time threshold value, under which no "cut down to the substrate" well defined lines were observed. This is due to the fact that the developer takes some time to break through a film of photoresist, even when entirely exposed (M=0). In our case, the developer took 20 seconds to reach the substrate surface through a 120 nm layer of entirely exposed photoresist.

Apart from threshold values limiting the exposure and development characteristics by the lower end, maximum values are also involved, and these are discussed below:

All samples exposed for longer than exp_{max}, as defined in the diagram, showed a washed out central patch and were therefore unsuitable for further use in the fabrication of X-ray grating masks. This shows that, even within the darkest areas of the interference pattern (i.e. the dark lines), exposure still occurred. Indeed, however low the light could be within these areas, given a long enough exposure time (9 seconds), the resist would be fully exposed and therefore entirely develop away. If the interference pattern contrast were ideal, i.e. no light intensity within the "dark areas", it would be possible to further move the exposure time upper limit, and therefore to extend the exposure range, thus allowing for monitoring of the grating line profile and width. However, limitations on the fringes contrast are inherent to the experimental setup; they are due to the Gaussian shape of the uncollimated beams, as shown in the theoretical section, and due also to scattering within the

photoresist material. Contrast deterioration also occurs if the symmetry between the two interfering beams is not perfect. It is difficult to assess to which extent each of the three reasons discussed above contribute to the grating contrast degradation. However, it is important to ensure that each of these factors is minimised by careful manipulation.

Finally, the diagram also exhibits a maximum value for the development time and this is the time the developer takes to develop through a layer of resist exposed at its threshold (M=0.4).

B.3.4 Conclusion:

It is now possible to consistantly produce gratings with an undercut line profile. All the samples were exposed for seven seconds and the choice of this exposure time is justified in that a margin of $\pm$1 second was needed, as the electrical shutter used on the setup presented a time response estimated to be half a second. It was operated manually and a simple clockwatch was used to time the exposure.

The development time was found to depend heavily on the characteristics of the developer, so another development procedure was devised. The samples were placed in a Petri dish and covered with developer, as development continued, a dark patch appeared at the center of the substrate, slowly spreading outwards. When this dark area had reached a predetermined dimension, the development was stopped immediately by flushing with deionised water.

The samples were then overcoated with a thin film of Au/Pd (about 100 nm), but, due to the poor adherence of gold films, a few angstroms of Ni/Cr was first evaporated onto the samples to act as an adherence enhancer. Lift-off was accomplished by dissolving the photoresist in acetone in an ultrasonic bath for ten minutes thus exposing grating lines over a wide area with very few defects, figure 50 and 51. However,a close inspection of the line profile under an electron microscope, revealed a

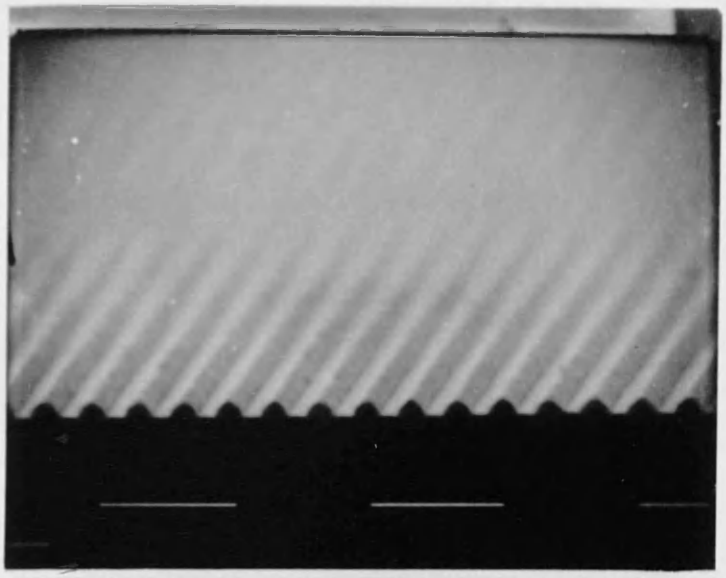

20000 magn.

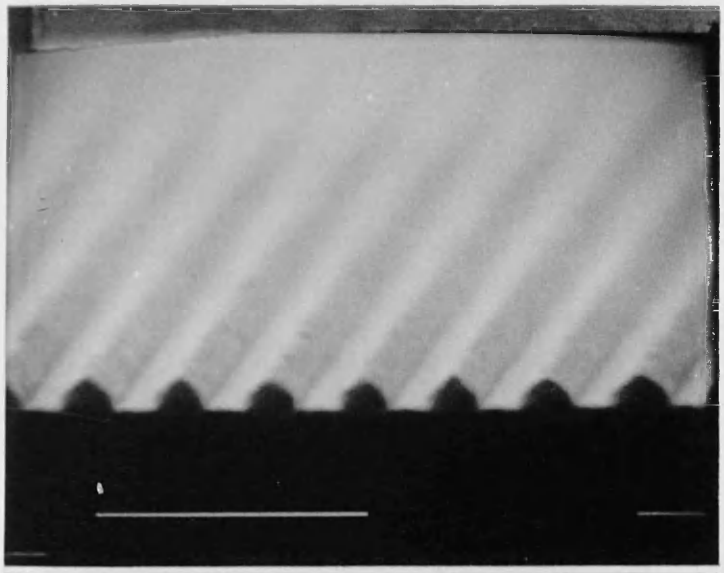

40000 magn.

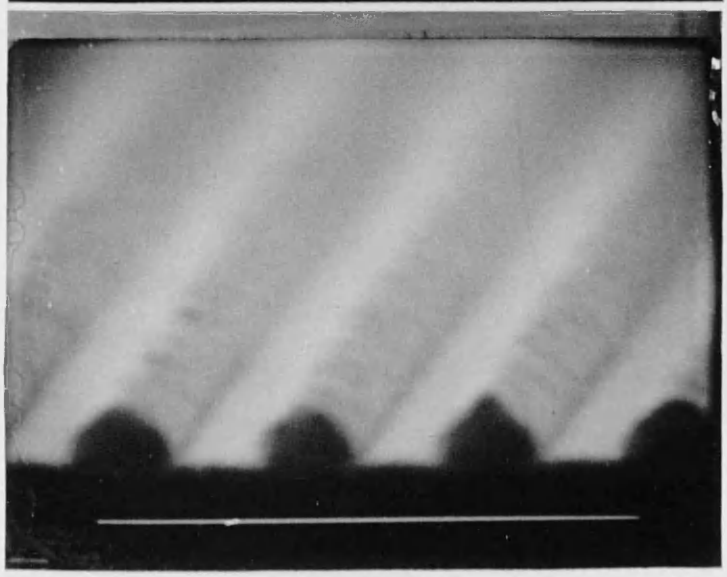

80000 magn.

Figure 50: Gold grating lines after lift-off.
(1 micron marker)

2500 magnification

10 micron marker

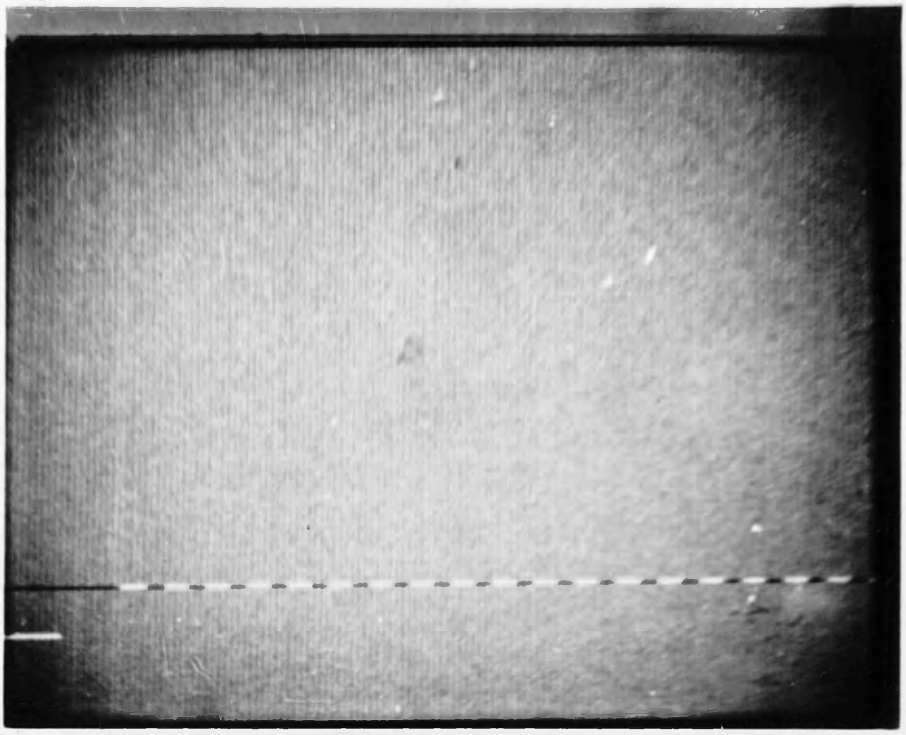

Figure 51: Overview of a Au/Pd grating showing good uniformity.

tunnelling effect (figure 52) indicating that the thickness of the evaporated metal (130 nm) was far greater than the expected thickness (around 90 nm). It is obvious that a much greater control of the metal thickness is required before the lift-off stage is well controlled.

Attempts were also made to open a window at the back of those gratings which presented an adequate metal line pattern. Unfortunately the attempts were not successful because it has proved impossible to adequately protect the grating pattern from the silicon nitride and the silicon etchants.

B.4 Short pitched gratings investigation:

The computer simulation is a close description of the photoresist exposure and development properties as shown in the previous section. The experimental technique is well mastered so that gratings with an undercut line profile can be produced consistantly over large areas; with both theoretical and experimental work showing that the lift-off stage can be made successful. It was also decided to investigate the fabrication of shorter pitched gratings using ultraviolet laser light and the front prism technique, either by themselves or in combination.

B.4.1 UV exposure without the front prism technique:

Silicon wafers coated with 70 nm of Si_3N_4 were used for this experiment; the argon ion laser was tuned in the ultraviolet; a small angle of incidence (around 35°) was set and the production of 0.3 micron gratings was attempted.

The samples were coated with a 150 nm layer of positive photoresist (SHIPLEY AZ 1370), exposed to the holographic pattern for 150 seconds and rapidly developed (less than 20 seconds). Observation of the developed samples by the naked eye revealed the same types of grating geometry as described in the previous section. A crown of "intense grating" with a washed out area in its center, surrounded by an area of "faint grating" was by far the most common intensity pattern which was obtained. This suggested that the samples were overexposed but reduction of the

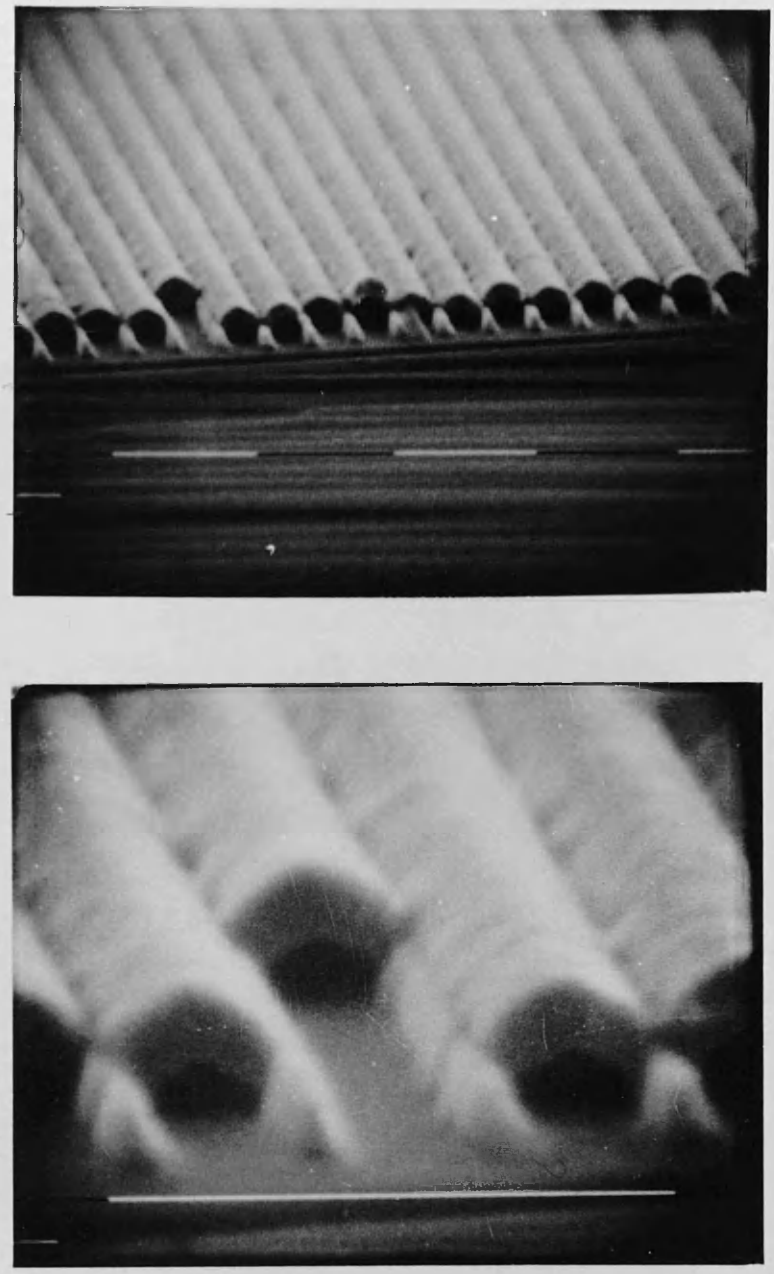

Figure 52: **Tunnelling effect after lift-off when the metal evaporation was too generous.**
(Top: 20000 magnification; Bottom: 80000 magnification)
1 micron marker

exposure time was ineffective, as the recorded gratings were very faint, and no cut down grating lines were observed.

Examination at low magnification of the various grating areas showed good uniformity, figure 53, and examination at high magnification of the line profiles showed that the bright areas were areas of well separated grating lines, figure 54b, contrary to those of "faint grating" where the resist film was not broken down to the substrate, figure 54a. The grating lines present an overcut profile as predicted by the computer simulation, figure 55.

The fabrication of gratings with a 60^{o} angle of incidence was also attempted. Exposure times in excess of 10 minutes and development times up to 3 minutes were necessary but no grating was recorded. Every slight deformation of the wavefront was strongly enhanced by such a high incidence and this is supported by previous experimental results reporting a limit of 58^{o} for the angle of incidence [Ref.100].

At the end of this series of experiments, the following observations were made.

The quality of the interfering wavefronts were good enough to produce gratings over a fairly large area, providing the angle of incidence was not set too high and the higher the angle of incidence the more difficulties were to be expected when printing gratings.

However, exposure times were long and this is not desirable as the grating recording is more likely to fail due to external conditions such as vibrations or stray light. In order to limit the effect of such phenomena, the laser was kept under light tight conditions to prevent unwanted exposure by stray light from inside the laser apparatus, and the gratings were printed at nightime when external vibrations proved to be at their lowest.

The development stage was also critical as the central part

2500 magnification

1 micron marker

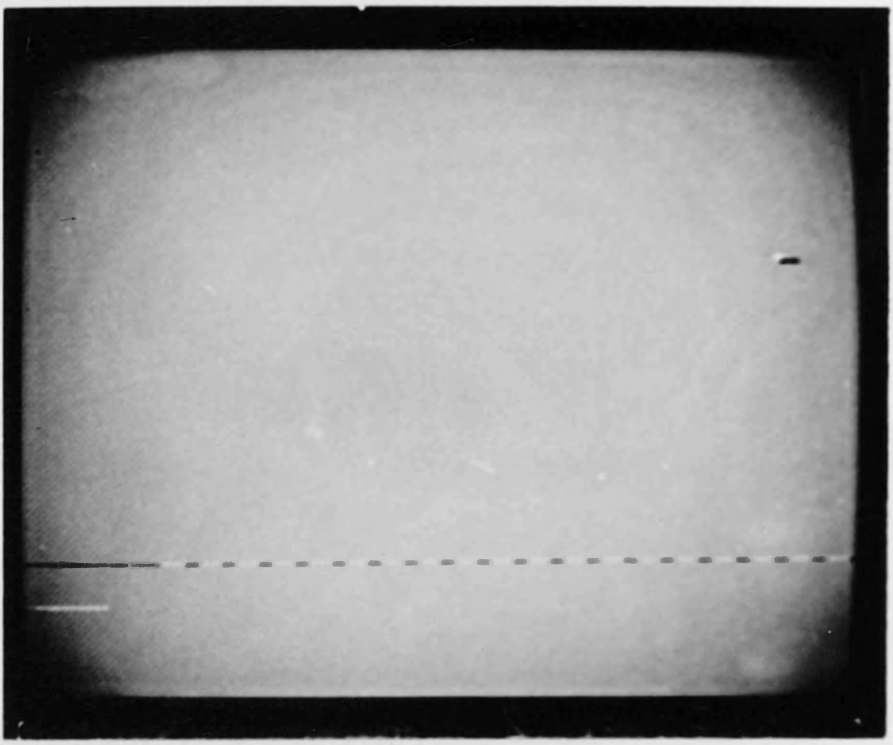

Figure 53: 0.29 micron grating.

a

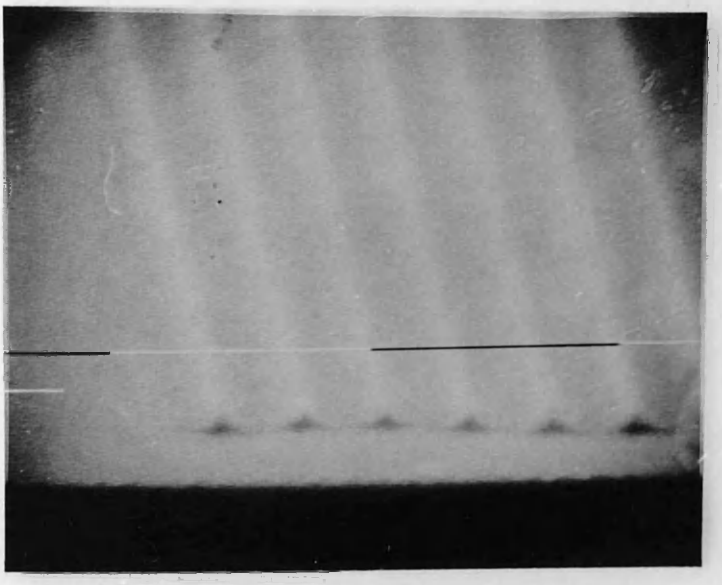

b

Figure 54: Line profile showing overcut.
(40000 magnification, 1 micron marker)

Data set:

Wavelength:	351.1 nm
Incidence:	37°
Nitride:	70 nm thick
Resist:	150 nm thick

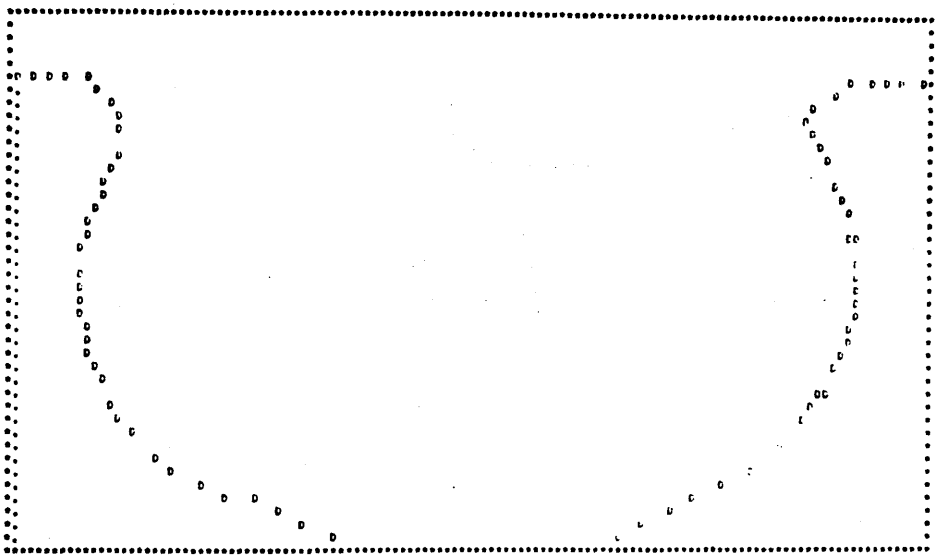

Figure 55: Computer simulation profile predicting an overcut.

of the gratings had to be washed out for any bright grating to appear over a large enough area. The solution to this problem would be to use a smaller pinhole (a 5 micron instead of the 10 micron used) as the diffracted central patch would be larger thus presenting a flatter intensity profile (a smaller pinhole size would also improve the quality of the filtering). However, increasing the central patch size of the filtered beam by either using a smaller pinhole or alternatively by moving the sample further from the spatial filtering units would further increase the exposure times.

In conclusion, although the printing of gratings using the UV line of the argon ion laser was shown possible, it was difficult due to the low power available (only 9 mW before the beam-splitter). This is why a high power helium-cadmium laser (lasing at 325. nm) should be used if possible.

B.4.2 UV exposure and front prism technique:

The experimental conditions chosen for the production of 0.12 micron gratings were:

-UV line 351.1 nm.

-50° of incidence inside a high index prism (1.95)

-70 nm of Si_3N_4

-150 nm of photoresist.

The holographic arrangement was set at 30° of incidence and a double 69° prism (quality $\lambda/20$) was used thus bringing the incidence inside the "input medium" to 50°. The prism was set so that the unfiltered beams met on its back surface. No matching index fluid was used and the optical contact between sample and prism was ensured by a pressure chamber.

0.12 micron gratings were produced with poor results. The gratings were patchy, the lines were not well separated and the

spaghetti-like effect was often observed (figure 56). Moreover, the transition between faint grating areas and the washed out central patch was very sharp (figure 57).

The exposure times were very long (from 3 to 5 minutes) due to the increase of the central patch size because of refraction in the prism and to the absorption of UV light by the prism material.

The development stage was also critical, similar to that reported previously, but the transition between faint grating area and washed out area was far sharper (less than 1/2 mm against 2 mm previously). This suggests that the central spot was not large enough so that its overall intensity profile could be considered flat over most of the sample. Placing the samples further from the pinholes as suggested in the previous paragraph would definitely lead to very long exposure times.

The patchy aspect of the gratings signifies the presence of noise within the interference pattern. One possible reason for this could be that some of the incoming light is scattered by the rough side surfaces of the prism. If this phenomenon is to be minimised blackening of the involved surfaces is advised.

It is also possible that noise could be the result of bad filtering made more noticeable by the increase in the beam's cross-sections due to refraction in a high index medium. This same phenomenon limits the angle of incidence on a simple setup.

Because of its low power, it was decided to give up the 351.1 nm line and to select the 457.9 nm blue line. It was also decided to experiment further with the front prism technique.

B.4.3 Blue exposure and front prism:

Experimental conditions:

-45° of incidence.

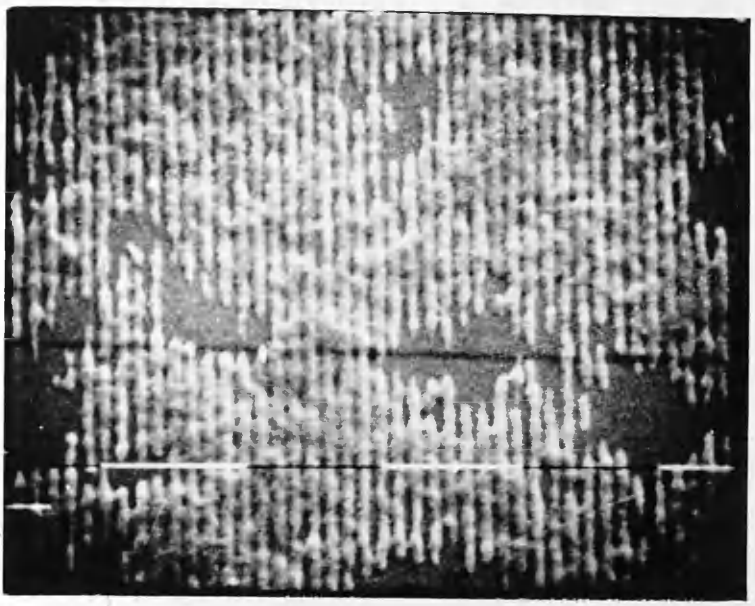

patchy grating (20000 magnification)

spaghetti-like effect (10000 magnification)

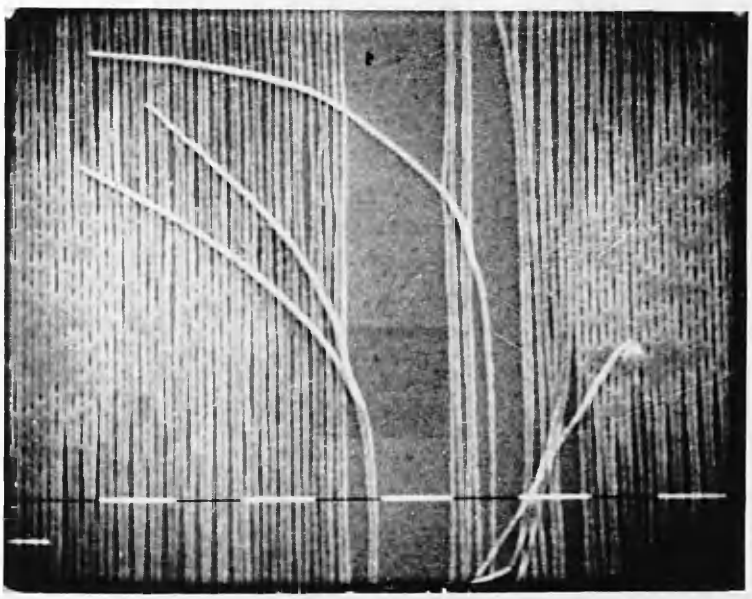

Figure 56: 0.12 micron gratings presenting a patchy aspect and spaghetti-like effect. (1 micron markers)

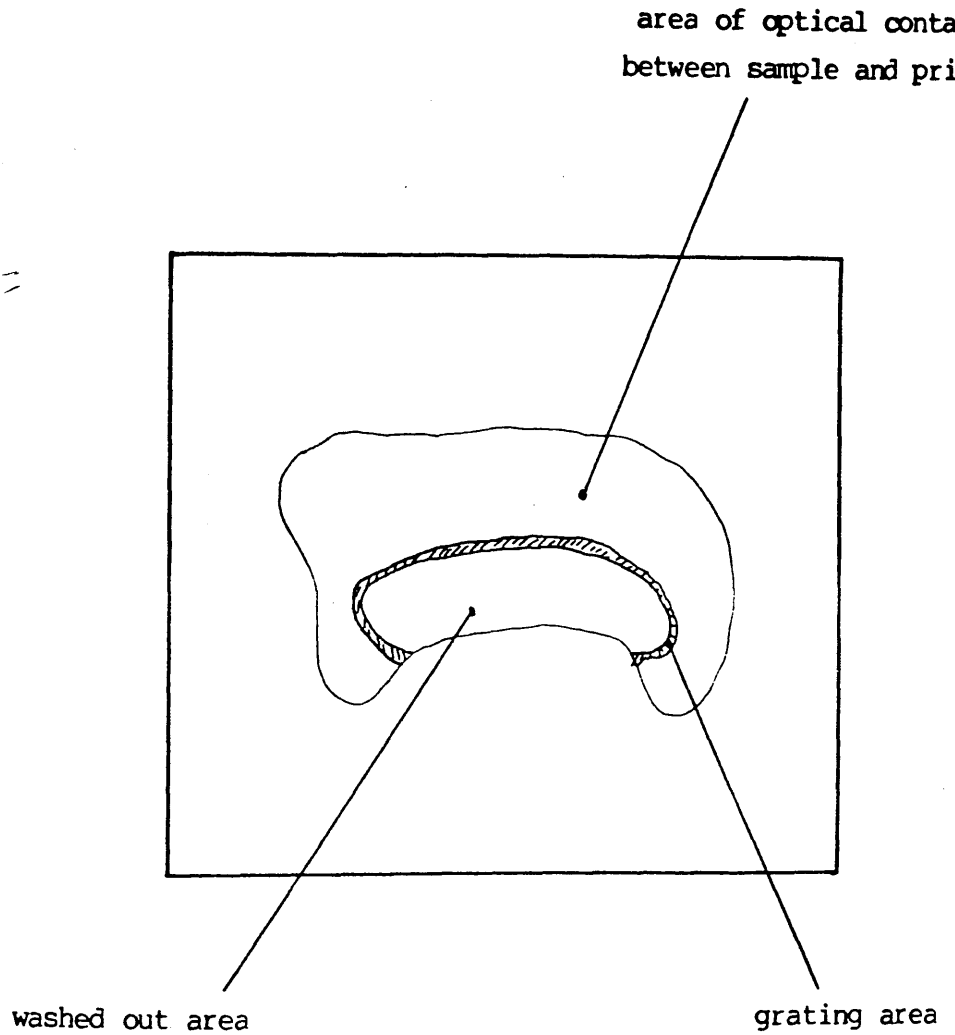

Figure 57: Geometry of the gratings produced with the front prism technique and UV light.

-Double 45° high index prism.

0.17 micron gratings were obtained, figure 58, with the type of defects reported previously. However, interesting moire patterns were superimposed on the gratings, figure 59, due, it is thought, to internal reflections within the prism. An overall modulation of the grating was also observed on a larger scale in the form of fringes of equal thickness from the film of matching index liquid when used, figure 60.

Exposure times were around 5 seconds and development times around 25 seconds, the exposure is much shorter because there was more power available (298 mW before the beam-splitter).

B.4.4 Discussion:

A preliminary experiment was undertaken on the basic setup with the laser tuned in the ultraviolet. The gratings produced were of good uniformity over a large area and the line profile showed an overcut in agreement with the computer simulation predictions.

No spaghetti-like effect was observed as should be expected, this phenomenon only occurring with undercut line profile.

The maximum possible size of the central patch before washout occurs is smaller than when blue light was used due to the smaller wavelength, the pinhole being used for the spatial filtering could not be changed for a smaller one.

The low power of the UV laser line rendered the exposure and development stage critical in that it was difficult to obtain well separated lines without washing out the central part of the exposed patch.

It was not attempted to further control the fabrication of gratings using the UV light without the front prism technique by investigating the whole exposure and development plane or by experimenting with other developer dilutions. Indeed, 0.3

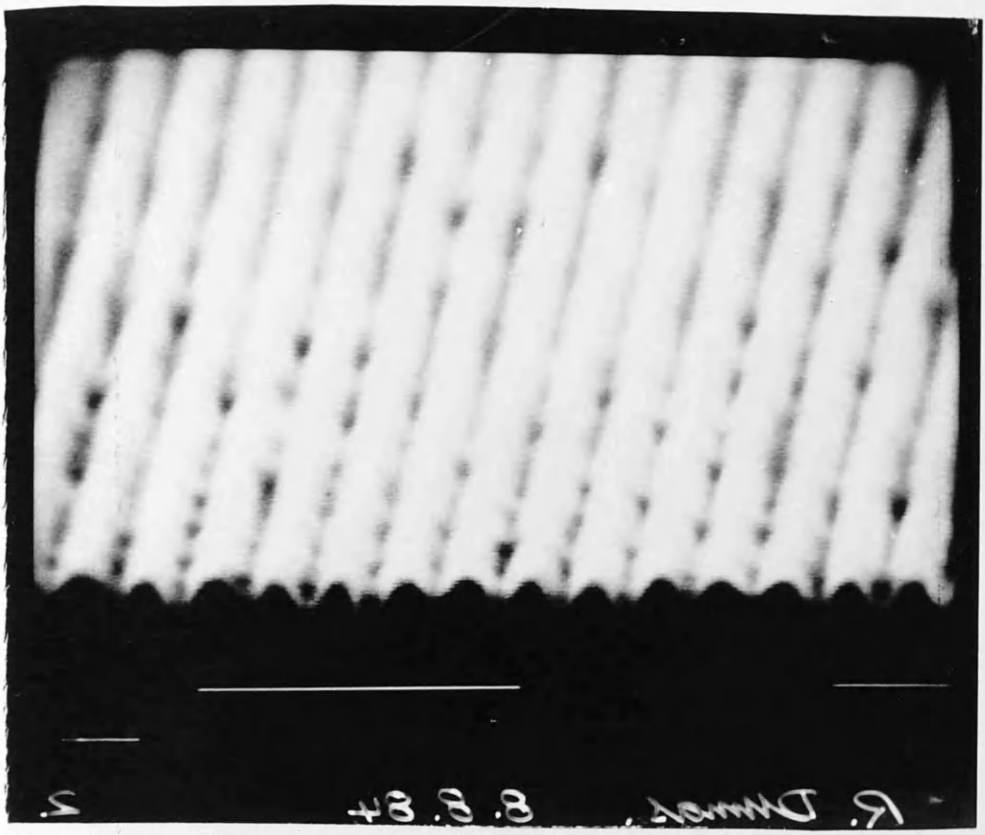

Figure 58: 0.17 micron grating micrograph.
(40000 magnification, 1 micron marker.)

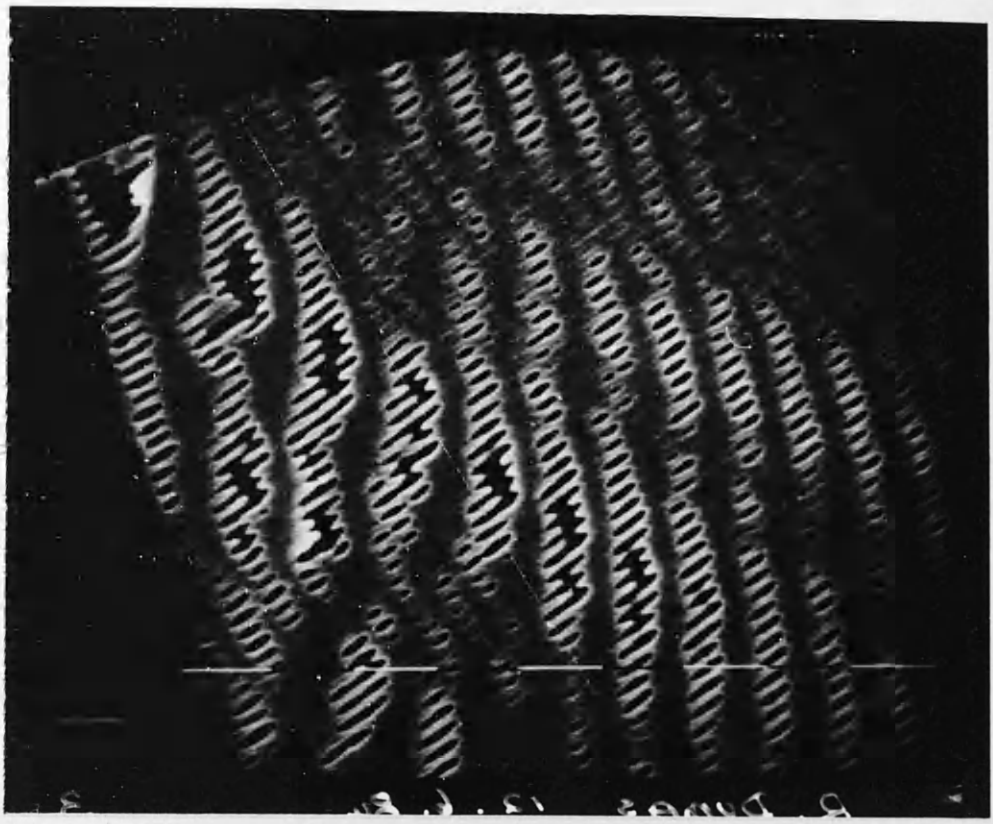

Figure 59: Moire pattern observed when using the front prism at normal incidence.
(10000 magnification, 1 micron marker)

Figure 60: Fringes of equal thickness lightly modulating the grating when index matching liquid was used. (100 micron marker, 20 magnification.)

micron gratings can be produced with excellent control as explained in the previous section. However, an attempt was made to print 0.1 micron gratings using the front prism technique on the UV setup. Success was partially met in that a 0.12 micron periodic pattern was recorded. Moreover, the occurrence of the spaghetti-like effect showed that the lines must have had a certain degree of undercut, as expected when the computer simulation was run to choose the silicon nitride thickness for this to happen.

The introduction of an input medium by means of the front prism technique gave rise to a high level of background noise which could be inferred from the patchy aspect of the gratings produced. It is thought that this is not inherent to bad filtering since the setup had not been modified, and the gratings produced without the FPT did not show the presence of luminous noise. It is possible however that better filtering can bring back the angle of incidence on the photoresist for the two laser beams above which wavefront deformations are so enhanced that the "noise" becomes predominant. It seems that within the experimental environment set on the bench, this limit for the angle of incidence is between 50° and 45°.

In order to further investigate the FPT, gratings were printed using the blue argon ion laser line for which more output power was available. This time, the front prism was used at normal incidence to avoid any refraction accross its input faces, which increases the beam cross section and therefore would enhance the beam defects. The angle of incidence was set at 45°, the angle of the prism, an angle below the limit exposed above. The gratings recorded presented only a low level of background noise and would have been fit for further exploitation if other phenomenon did not occur.

Indeed, a Moire pattern was observed modulating the overall grating when the prism was used at normal incidence. This is caused by internal reflections inside the prism. It is interesting to note that it must be possible, although not

practical, to adjust the setup, and particularly the input prism, so that the gratings arising from the internal reflections, those arising from the two input beams and their reflections on the substrate coincide.

Problems were also encountered when using an index matching fluid to provide optical contact between prism and samples. Classical fringes of equal thickness were observed slightly modulating the grating pattern. The problem was circumvented simply by not using any index matching liquid. Optical contact was ensured by mechanical pressure of the sample onto the back surface of the prism, a small pressure chamber being pumped up. This way optical contact was obtained over large enough areas providing the samples and the back surface of the prism were absolutely clean.

B.4.5 Conclusion:

The problems encountered were of various kinds. Linked to the low power available, problems arose from vibrations as can be seen by linked up lines and ambient luminous noise.

Linked to bad spatial filtering, the angle of incidence on the photoresist could not be set high enough; the beam's defects were strongly enhanced by high angle of incidence and this was given away by the patchy aspect of the gratings.

Lastly, linked to the FPT itself, Moire patterns were observed modulating the overall grating. This problem can be circumvented by using the front prism at oblique incidence.

It was not possible to expand sufficiently the laser beams and also to stay at an acceptable level of light intensity, so that the central patch of the diffracted pattern from the pinholes would present a flat intensity profile. This is why the development stage was critical; washing out was necessary before well defined separate lines could be observed.

It seems that the use of a deep UV laser with a high ouput power directly exposing the recording sample is the only viable alternative to holographic printing of very short pitch gratings.

CONCLUSION

Before a line of progress for future experiments is suggested, a summary of the obtained results is presented along with a discussion on the various problems encountered throughout the project.

C.1) Results:

0.3 micron gratings with undercut line profile over a large area were repeatedly recorded in a film of positive photoresist coating a Si_3N_4/Si substrate with a symmetrical holographic setup using the blue line 457.9 nm of an argon ion laser. 0.12 micron and 0.17 micron gratings were also recorded in the photoresist material by using the UV line of the laser and the front prism technique. The very short pitch gratings exhibited important defects which rendered them unsuitable for lift-off.

The computer predictions in each case, undercut, overcut and lateral break through, or the spaghetti-like effect, were experimentally verified which shows the usefulness of such a tool, since the Si_3N_4 thickness can now be determined rapidly for an undercut profile to be produced. It is important to mention that the computer program can tackle any kind of substrate system and is not limited to the case studied in our work.

On exploitable samples, a Au or Au/Pd metal layer was evaporated under vacuum, and lifted-off by dissolution of the photoresist lines in acetone. The metal pattern was generally well defined.

Lastly, attempts were made at the opening of a window at the back of the gratings but no reliable technique has yet been found which fully protects the metal pattern from the various etchants.

C.2) Discussion:

Experimental and theoretical work are discussed and possible improvements on the methods and solutions to the problems are

suggested.

C.2.1 Holographic exposure:

The theoretical study of the holographic exposure suggested that, using collimating lenses (and thus keeping the number of optical components between the pinholes and the sample to a minimum) would lead to major changes in the grating geometry. Indeed, the assumption that a non collimated beam could be approximated by a plane wave was justified in that the experimental results showed good uniformity of the grating over a large area.

However, a noticeable amount of the light energy is lost in the diffraction pattern generated by the pinholes of which only the middle part of the central patch is used. This calls for a particularly powerful laser line and an output power of about 300 mW seems to be the minimum requirement. Lower powers lead to long exposure times and render the holographic process critical and of low repeatability due to external light pollution and mechanical vibrations in the optical setup.

C.2.2 Computer simulation:

A computer simulation program was written which, given the experimental conditions on the holographic bench and the material characteristics, outputs an inhibitor fraction map of the photoresist depth across one grating pitch. This inhibitor map can be processed by an already existing program which in turn outputs the resist developed profile.

It is interesting to note that such a computer program has been written for the holographic process [Ref.124]. Such simulations make an extensive use of the Fresnel coefficients of a thin film [Ref.115] and consider the photoresist film as a homogeneous medium.

The program developed in the course of our work is new in that it does not suppose the photoresist material to be homogeneous and takes into account the progressive bleaching

properties of the photoresist as exposure continues. Also taken into account are the different rates of bleaching at different depth in the photoresist film due to the non homogeneous electrical field distribution of the exposing light pattern.

This should lead to much more accurate simulations of the process. This advantage does not stand out at present due to the partial unavailability of accurate data on the photoresist bleaching constants at the wavelengths we were involved with.

However, when such data becomes available, it should be possible to accurately determine the exposure and development times as well as to choose the most adequate experimental conditions such as layer thicknesses and angle of incidence for the desired line profile to be produced. It should ultimately be possible to experiment "on the computer" with various parameters of the experimental environment, and print gratings with the required qualities successfully at the first attempt.

Due to its modular form, the computer program can easily be modified to suit any kind of problem involving the recording of a light pattern in a photoresist material coating a multilayer system.

The computer simulation was used to determine the silicon nitride thickness necessary for an undercut profile to occur in the resist. Despite the lack of accurate data for the experimental environment, the program gave a fair account of the experimental profile. This is why it can already be used as a good guideline in the printing of photoresist gratings.

C.2.3 UV laser:

The use of the 351.1 nm line of the argon ion laser UV doublet was investigated and showed that the use of a weak line (9 mW) is critical due to long exposure times and the developed samples only presented the desired grating properties over very thin areas between washed out places and places where the gratings was faint. If a UV laser light is to be used in further

experiments, it is advisable to use a helium cadmium laser with a light output intensity of no less than 300 mW.

As the gratings presented a patchy aspect, indication of optical noise in the beam, it is thought that the 10 micron pinholes used were not filtering the beams adequately and the use of a 6 micron pinhole is suggested.

C.2.4 Front prism technique:

It is possible to artificially decrease the light wavelength and therefore to produce smaller pitched gratings by using a prism in contact with the sample and the production of gratings with this technique was investigated.

Many problems were encountered when using the front prism technique and it is possible to draw a few comments from these failures.

Using a matching index fluid for optical contact did not seem to make any difference compared with the dry technique apart from the occurrence of widely spaced fringes of equal thickness lightly modulating the overall grating pattern.

The gratings were of a patchy aspect which can be attributed to bad filtering for a part but which could also well be the result of a light scattering phenomenon on the unused surfaces of the prism. In order to limit this phenomenon it is suggested that the unused faces of the prism should be roughened and painted matt black.

Finally moire patterns were observed, strongly modulating the grating pattern when the prism was used at normal incidence and it is probably due to internal reflections within the prism. Therefore the prism angle should be chosen so as to prevent these reflections from reaching the substrate and this can be helped by using the prism at incidences far away from the normal. It might be possible to adjust the incidence of the beams on the prism so accurately that the fundamental grating and the gratings arising

from inside the prism reflections coincide perfectly and maybe enhance the overall grating contrast.

C.2.5 Exposure and development:

Using the 457.9 nm laser line, the samples were exposed for 7 seconds to 2.3 mW/cm^2 beams of light giving a total energy of 16 mJ/cm^2 per beam. The developing procedure was original in the sense that it was found to be easier and more repeatable not to give the samples a set development time but on the contrary to use visual judgement to decide when to stop the developing as areas where the grating is sufficiently developed, i.e. cut down to the substrate, appear of a different colour to the eye. By using a visual procedure, the degradation of the qualities of the developer can be compensated for as it oxidises when in contact with air and becomes weaker as more and more samples are developed.

C.2.6 Lift-off:

On the gratings which presented an undercut profile, metal lines were lifted-off metal by evaporating a thin layer of Au or Au/Pd under high vacuum and by subsequently dissolving the photoresist in acetone.

It was found necessary to evaporate a very thin (a few angstroms) layer of Ni/Cr prior to the metal deposition to increase its adherence to the substrate.

In some cases the amount of metal evaporated was too high and a tunnelling effect was observed giving a particularly good indication of the resist line profile and showing that the obtained undercut was of high quality. This could perhaps be used as a method for visualising resist line profiles for it was found difficult to obtain profile pictures of the resist due to its non conductivity, an undesirable property when viewing under an electron microscope.

C.3) Future experiments:

Aiming towards the fabrication of an X-ray grating mask,

future experiments can be lined up as follows.

C.3.1 Fabrication of smaller pitched gratings:

It is possible to make gratings of a pitch smaller than 0.3 micron by using a He-Cd laser line at 325.0 nm instead of the 457.9 blue line of the argon ion laser on the holographic arrangement. The grating pitch can then be brought down to 0.2 micron by this simple wavelength switch and a further reduction is possible if the front prism technique is used. It is necessary however to make sure that the following points are satisfied:

-Laser output of no less than 300 mW.

-Pinhole size not greater than 6 micron and smaller if necessary.

-If the front prism technique is used, oblique incidence and blackening of its side faces are advised.

When the production of very small pitch gratings over a relatively wide area is mastered, it would be sensible to run a computer simulation to determine the silicon nitride thickness necessary for an undercut profile to occur.

C.3.2 Lift-off:

It has been shown that it is important not to evaporate too much metal on the photoresist grating for the obtention of well defined and separated metal lines.

It must be determined experimentally the highest thickness of deposited metal in relation to the resist line thickness which would allow a successful lift-off.

C.3.3 Window opening:

The last stage in the fabrication of an X-ray mask consists in opening a window in the silicon substrate thereby exposing the nitride membrane supporting the metal grating. However, difficulties arise in that no suitable procedure has yet been

devised to protect the metal pattern from the vigorous etchants. The use of the device shown in figure 61, cut from a block of PTFE and which only lets one surface of the sample in contact to the etchants is proposed. It was found however that the seal was not of sufficiently high quality and the chemicals seeped through to the grating pattern. The use of a hard PTFE O-ring is not advisable as the samples are easily broken by excess pressure and a soft rubber seal does not stand the hot etchants usually used in the fabrication of silicon nitride membranes. Filling the cavity with oil might isolate the metal pattern from the etchants or the use of a wax, covering the grating area, could also be the answer.

C.4) Conclusion:

If the preceeding steps are fully mastered, it should be possible to produce a grating X-ray mask transferrable by X-ray lithography at the carbon K_{α} line.

The use of such masks are various and include:

-the fabrication of DFB or DBR lasers.

-the fabrication of optical wavelength filters by bragg reflection or refraction.

-the fabrication of input or output bragg couplers.

and this could facilitate the fabrication of the first truly integrated optical circuits.

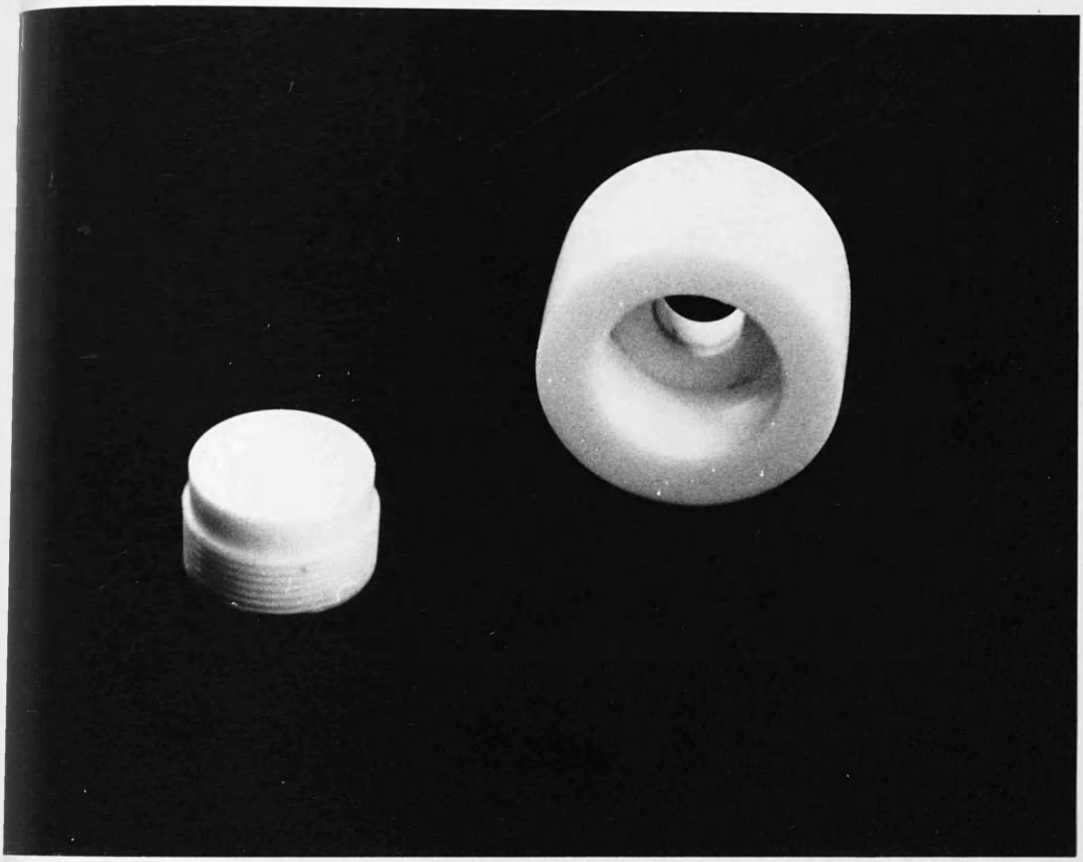

Figure 61: Suggested device for the protection of the metal grating from the various etchants.

APPENDICES

REFERENCES

APPENDIX 1

Figure A1 contains all information on the adopted notation . The two plane waves are of equal amplitude, of identical polarization and of symmetrical incidence. They also propagate in a perfect non-absorbing medium of index n.

Letting aside the time dependence, the electric fields $\mathbf{E}_1$ and $\mathbf{E}_2$ can be written as follows:

$$\mathbf{E}_1 = E\mathbf{u}_z \exp i\mathbf{k}_1.\mathbf{r} \qquad (A13)$$

$$\mathbf{E}_2 = E\mathbf{u}_z \exp i\mathbf{k}_2.\mathbf{r} \qquad (A14)$$

Calculation leads to:

$$\mathbf{k}_1.\mathbf{r} = -2\pi n/\lambda(x\sin\theta + y\cos\theta) \qquad (A15)$$

$$\mathbf{k}_2.\mathbf{r} = 2\pi n/\lambda(x\sin\theta - y\cos\theta) \qquad (A16)$$

The total field at point M is therefore:

$$\mathbf{E}_{tot} = 2E\mathbf{u}_z \exp(-2i\pi ny\cos\theta/\lambda)\cosh(2i\pi nx\sin\theta/\lambda) \qquad (A17)$$

or, by using the well known identity, $\cosh(ix) = \cos(x)$,

$$\mathbf{E}_{tot} = 2E\mathbf{u}_z \exp(-2i\pi ny\cos\theta/\lambda)\cos(2\pi n\sin\theta x/\lambda) \qquad (Ai8)$$

Taking the square modulus of the field leads to the intensity profile:

$$I = 4I_0\cos^2(2\pi n\sin\theta x/\lambda) \qquad (A19)$$

or, by means of a trigonometric identity:

$$I = 2I_0\left[1+\cos(2\pi x 2n\sin\theta/\lambda)\right] \qquad (A20)$$

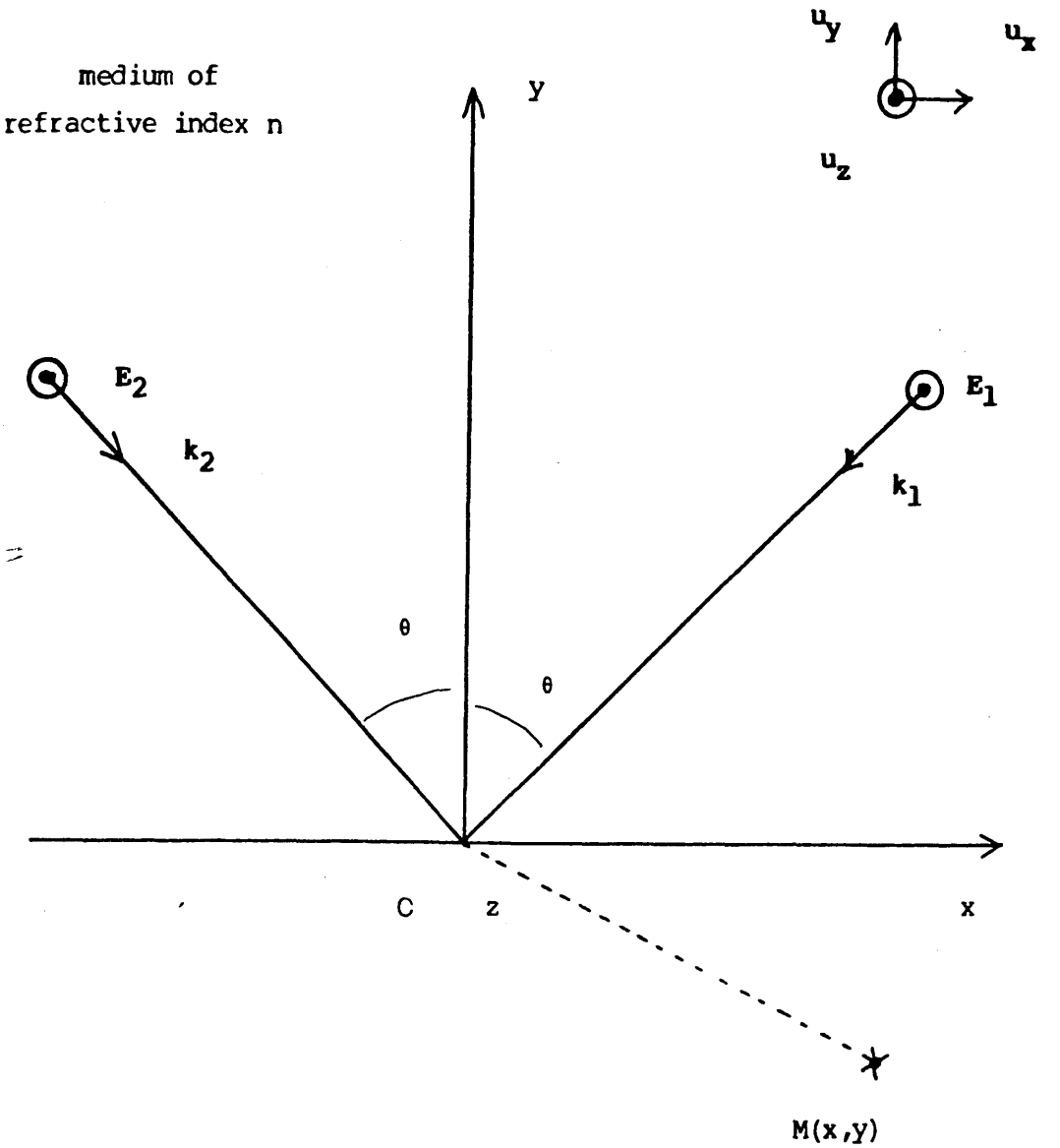

(x,y) plane of incidence

(z) direction of polarisation (s-polar.)

Figure A1: Notation for the interference between two plane waves.

This is the expression of a periodic pattern in x (lines along the z-axis) of periodicity p given by:

$$p = \lambda/(2n\sin\theta) \qquad (A21)$$

Thus has the well known pitch equation for holographic gratings been reestablished.

APPENDIX 2

```
C HOLOGRAM USES STREAM 3 AS INPUT FILE
C STREAM 4 AS OUTPUT FILE
C STREAM 6 AS DATA TRANSFERT FILE FOR SAMPLE
C STREAM 8 AS COMMANDS TRANSFERT FILE FOR SAMPLE
C
C COMMON REFRACTIVE INDEX (RINDX) COMPLEX
      COMMON/INDEX/RINDX(4)
C COMMON OF EXPOSURE CARACTERISTICS
C EXPINT=EXPOSURE INTENSITY
C EXPTIM=EXPOSURE TIME
C EXPOS=ARRAY CONTAINING THE ENERGY PROFILE
C FOR A SYMETRIC HOLOGRAPHIC ARRANGEMENT.
      COMMON/EXPOS/EXPINT,EXPTIM,EXPOS(21)
C COMMON CONTPOLING THE INPUT SUBROUTINE
C FOR MORE COMMENTS SEE INPUTS AT THE END
      COMMON/FLAG/IFLAG(6)
C INTENSITY COMMON, VERTIN=VERTICAL INTENSITY
C HORENS=HORIZONTAL ENERGY AT EVERY POINT.
      COMMON/INTENS/VERTIN(51),HORES(50)
C INHIBITOR COMMON, MEMORING SPACE,
C MEN=TABLE OF INHIBITOR VERSUS DEPTH AND ENERGY
      COMMON/INHIB/M(51),MEN(51,21),RMXZ(52,52)
C THICKNESS COMMON, THICK(1) AND 4 ARE NOT
C USED, THEY ARE HERE FOR UNIFORMITY.
      COMMON/THICKN/THICK(4)
C EFFECTIVE INDEX COMMON, INCLUDES THE OBLIQUE INCIDENCE.
C EFRDX=INDEX OF EACH RESIST SUBDIVISION
C SIERDX=INDEX OF THE INTERMEDIATE LAYER.
      COMMON/EFINDX/EFRDX(51),SIERDX
C SUBSTRATE+INTERMEDIATE LAYER CONSTANTS COMMON
C SIAMAT=MATRIX OF SYSTEM, PHSFT=PHASE SHIFT
C RCOEF=REFLECTION COEFFICIENT.
      COMMON/MITSIL/SIAMAT(2,2),PHSFT,RCOEF
C SIMULATION PARAMETERS COMMON,
C DELTZ=THICKNESS OF A RESIST SUBLAYER,
C DELTX=DISTANCE BETWEEN TWO HORIZONTAL POINTS,
C DOSDEC=ENERGY STEP, ON WHICH DEPENDS THE ACCURACY,
      COMMON/SIMUL/DELTZ,DOSDEC,DELTX
C CONSTANTS COMMON, WAVEL=WAVELENGTH, PI=3.14...,
C RND=AIR REAL INDEX, THETA=ANGLE OF INCIDENCE IN RADS.
      COMMON/CSTES/WAVEL,PI,RND,THETA
C RESIST COEFFICIENTS A,B,C.
      COMMON/RESIST/AP,BP,CP
      COMPLEX RINDX,EFRDX,SIERDX
      COMPLEX SIAMAT,PRMAT(2,2)
      REAL M,MEN
      PI=4.*ATAN(1.)
C INPUT DATA
      DO 1 I=1,6
      IFLAG(I)=1
    1 CONTINUE
      CALL INPUT3
C COMPUTE INHIBITOR VERSUS DEPTH AND ENERGIE UP TO 2*DOSE
    2 CALL MAPVEN
C COMPUTES INHIBITOR VERSUS X AND Z
      CALL MAPVXZ
C OUTPUT RMXZ IN PLOTFL TO BE PASSED INTO SAMPLE
      WRITE(6)DELTX
      WRITE(6)DELTZ
      WRITE(6) RMXZ
      WRITE(8,*)'TRIAL 10'
      WRITE(8,*)'RUN 4'
C READ INPUT STRUCTURE
      READ(3,*)IFLAG
C INPUT NEW DATA AS REQUIRED
      WRITE(4,*)'END OF THE PREVIOUS SET OF DATA.'
      CALL INPUT3
C CONTROL THE FLOW OF THE MAINPROGRAM, IF 1 COMPUTE AGAIN
C WITH NEW DATA, IF 0 STOP.
      READ(3,*) IALLOW
      IF(IALLOW.EQ.1) GOTO 2
      STOP
      END
```

```
C
C
C
      SUBROUTINE MAPVXZ
      COMMON/EXPOS/EXPINT,EXPTIM,EXPOS(21)
      COMMON/INTENS/VENTIN(51),MOREN(50)
      COMMON/INHIB/M(51),MEN(51,21),RMXZ(52,52)
      COMMON/SIMUL/DELTZ,DOSDEC,DELTX
      COMMON/CSTES/MAVEL,PI,RND,THETA
      REAL M,MEN
C COMPUTES PERIODICITY
      MINDO=MAVEL/2/RND/SIN(THETA)
      DELTX=MINDO/49.
      WRITE(4,*)'PERIODICITY',MINDO
C COMPUTES EXPOS TABLE (TABLE OF ENERGIES FOR WHICH
C INHIBITOR HAS BEEN COMPUTED)
      DUM=EXPINT*EXPTIM/10.
      DO 2 I=1,21
      EXPOS(I)=(I-1)*DUM
    2 CONTINUE
C COMPUTES THE INCIDENT ENERGY TABLE FOR A HOLOGRAM
      DO 3 I=1,50
      MOREN(I)=(1+COS(DELTX*(I-1)*2*PI/MINDO-PI))*EXPTIM*EXPINT
    3 CONTINUE
C RESET FLAG STATING THAT INHIBITOR IS LESS THAN 0.4.
      IFLG=0
C FOR EACH X
      DO 40 I=1,50
C FIND OUT THE CLOSEST VALUE OF ENERGY OUT OF EXPOS
      IEN=2
   10 IF(EXPOS(IEN).GT.MOREN(I)) GOTO 20
      IEN=IEN+1
      IF(IEN.EQ.21) GOTO 20
      GOTO 10
C NOW INCIDENT ENERGY (MOREN) AT X LIES BETWEEN
C EXPOS(IEN-1) AND EXPOS(IEN)
C
C A SIMPLE LINEAR INTERPOLATION PROVIDES THE INHIBITOR
C VALUE FOR X AND EVERY Z.
   20 FRAC=(MOREN(I)-EXPOS(IEN-1))/(EXPOS(IEN)-EXPOS(IEN-1))
      DO 30 J=2,51
      RMXZ(I+1,J)=MEN(J,IEN-1)+FRAC*(MEN(J,IEN)-MEN(J,IEN-1))
      IF(RMXZ(I+1,J).LT..4) IFLG=1
   30 CONTINUE
   40 CONTINUE
C FILL UP EXTRA ROWS AND COLUMNS AS CLMXZ OF SAMPLE DOES
      DO 60 I=2,51
      RMXZ(I,1)=RMXZ(I,2)+RMXZ(I,2)-RMXZ(I,3)
      IF(RMXZ(I,1).GT.1.) RMXZ(I,1)=1.
      RMXZ(I,52)=RMXZ(I,51)+RMXZ(I,51)-RMXZ(I,50)
      IF(RMXZ(I,52).GT.1.) RMXZ(I,52)=1.
   60 CONTINUE
      DO 70 I=1,52
      RMXZ(1,I)=RMXZ(2,I)+RMXZ(2,I)-RMXZ(3,I)
      IF(RMXZ(1,I).GT.1.) RMXZ(1,I)=1.
      RMXZ(52,I)=RMXZ(51,I)+RMXZ(51,I)-RMXZ(50,I)
      IF(RMXZ(52,I).GT.1.) RMXZ(52,I)=1.
   70 CONTINUE
C NOW, RMXZ IS EXACTLY WHAT SAMPLE DEVELOPPING
C MACHINE EXPECTS.
C
C OUTPUT A MESSAGE IN CASE THE INHIBITOR FRACTION
C IS LESS THAN .4 AT SOME POINTS IN THE RESIST.
      IF(IFLG.EQ.0) RETURN
      WRITE(4,1000)
      WRITE(4,80)
      RETURN
 1000 FORMAT(///,20X,'----------SYSTEM MESSAGE(HOLOG)----------',/)
   80 FORMAT(10X,44HM IS SMALLER THAN .4 AT POINTS IN THE RESIST)
      END
```

```
C
C
C
C
      SUBROUTINE MAPVEN
      COMMON/INDEX/RINDX(4)
      COMMON/THICKN/THICK(4)
      COMMON/EXPOS/EXPINT,EXPTIM,EXPOS(21)
      COMMON/FLAG/IFLAG(6)
      COMMON/INHIB/M(51),MEN(51,21),RMXZ(52,52)
      COMMON/EFINDX/EFRDX(51),SIERDX
      COMMON/NITSIL/SINMAT(2,2),PHSFT,RCOEF
      COMMON/SIMUL/DELTZ,DOSDEC,DELTX
      COMMON/CSTES/WAVEL,PI,RNO,THETA
      COMPLEX EFRDX,SIERDX,EFIDX,W2
      COMPLEX SINMAT,WRKMAT(2,2),RINDX
      REAL M,MEN
C DETERMINE THE ENTRY POINT ACCORDING TO THE FLAGS
      IF(IFLAG(1).EQ.1.OR.IFLAG(2).EQ.1.OR.IFLAG(3).EQ.1) GOTO 10
      IF(IFLAG(4).EQ.1) GOTO 20
      IF(IFLAG(5).EQ.1) GOTO 30
      IF(IFLAG(6).EQ.1) GOTO 40
      WRITE(4,*) 'NOTHING CHANGED'
      RETURN
C COMPUTES SIERDX,EFRDX(1)
   10 SIERDX=EFIDX(RINDX(3))
      EFRDX(1)=EFIDX(RINDX(1))
C COMPUTES SINMAT
      W2=EFIDX(RINDX(4))
      CALL PASMAT(W2,SIERDX,SINMAT)
   20 DELTZ=THICK(3)
      CALL TRAMAT(SIERDX,WRKMAT)
      CALL MULMAT(WRKMAT,SINMAT,SINMAT)
C COMPUTES REFLECTION COEFF
      RCOEF=CABS(SINMAT(2,1)/SINMAT(1,1))
      IF (RCOEF.EQ.0.) GOTO 30
      PHSFT=AIMAG(CLOG(SINMAT(2,1)/SINMAT(1,1)))
      PHSFT=PHSFT*180./PI
      WRITE(4,*) 'REFLECTION COEF',RCOEF,PHSFT
C INITIALIZATION OF DELTA Z (DELTZ)
   30 DELTZ=THICK(2)/50
C INITIALIZATION OF M ARRAY
   40 DO 1 I=1,51
      M(I)=1.
      MEN(I,1)=M(I)
    1 CONTINUE
C GET A MAP OF INHIBITOR FRACTION, MEN(51,21),
C VERSUS Z(I) AND EXPOSURE DOSE.
      DO 2 I=2,21
      DOS=DOSDEC
      DOSE=EXPTIM*EXPINT/10.
C SET DOS IN CASE DOSE IS LESS THAN DOSDEC
   50 IF(DOSE.LE.DOSDEC) DOS=DOSE
C GET A NEW MAP OF INDEX WITH THE PREVIOUS INHIBITOR MAP
      CALL INHIND
C GET AN INTENSITY MAP ACCORDING TO THE INDEX MAP
C NORMALIZATION ACCORDING TO AN INCIDENT DOSE OF DOSDEC
      CALL INDINT
C GET THE NEW INHIBITOR MAP ACCORDING TO THE INTENSITY
C PATTERN
      CALL INTINH
C COUNTDOWN WITH DOSE
      DOSE=DOSE-DOS
C NEW CYCLE IF REQUIRED
      IF(DOSE.GT.0.) GOTO 50
      DO 3 J=1,51
      MEN(J,I)=M(J)
    3 CONTINUE
    2 CONTINUE
      RETURN
      END
```

```
C
C
C
      SUBROUTINE INDINT
      COMPLEX RINDX,SIERDX,EFRDX,SINMAT
      COMMON/INTENS/VERTIN(51),HOREN(50)
      COMMON/SIMUL/DELTZ,DOSDEC,DELTX
      COMMON/INDEX/RINDX(4)
      COMMON/EFINDX/EFRDX(51),SIERDX
      COMMON/NITSIL/SINMAT(2,2),PHSFT,RCOEF
      COMPLEX *RKMAT(2,2),P(2,2)
C
C GIVEN SINMAT(MATRIX OF SI+SIN),EFRDX(TABLE OF EFRDX OF RESIST)
C SIERDX(EFRDX OF SILICON NITRIDE), THIS SUBROUTINE COMPUTES
C THE INTENSITY PATTERN IN PHOTORESIST (VERTIN(51)),
C FOR AN INCIDENT DOSE OF DOSDEC MILLIJOULES
C
C COMPUTES FIRST THE MATRIX OF THE SYSTEM AND
C THE INTENSITY MAP.
      REFRAC=REAL(RINDX(2))
      CALL PASMAT(SIERDX,EFRDX(51),P)
      CALL MULMAT(P,SINMAT,*RKMAT)
      VERTIN(51)=REFRAC*CABS(*RKMAT(1,1)+*RKMAT(2,1))**2
      DO 1 J=1,50
      CALL TRAMAT(EFRDX(52-J),P)
      CALL MULMAT(P,*RKMAT,*RKMAT)
      CALL PASMAT(EFRDX(52-J),EFRDX(51-J),P)
      CALL MULMAT(P,*RKMAT,*RKMAT)
      IF(J.EQ.50) REFRAC=REAL(RINDX(1))
      VERTIN(51-J)=REFRAC*CABS(*RKMAT(1,1)+*RKMAT(2,1))**2
    1 CONTINUE
C NORMALIZATION ACCORDING TO DOSDEC
      CNORM=CABS(*RKMAT(1,1))**2/DOSDEC
      DO 2 I=1,51
      VERTIN(I)=VERTIN(I)/CNORM
    2 CONTINUE
      RETURN
      END
C
C
C
      SUBROUTINE INHIND
      COMMON/EFINDX/EFRDX(51),SIERDX
      COMMON/INDEX/RINDX(4)
      COMMON/CSTES/*AVEL,PI,RND,THETA
      COMMON/RESIST/AP,BP,CP
      COMMON/INHIB/M(51),MEN(51,21),RMXZ(52,52)
      REAL M,MEN
      COMPLEX EFIDX,EFRDX,RINDX,SIERDX
C
C COMPUTES THE EFFECTIVE INDEX MAP KNOWING THE
C INHIBITOR MAP.
C
      DO 1 I=2,51
      EFRDX(I)=CMPLX(REAL(RINDX(2)),-*AVEL/4/PI*(AP*M(I)+BP))
      EFRDX(I)=EFIDX(EFRDX(I))
    1 CONTINUE
      RETURN
      END
```

```
C
C
C
      SUBROUTINE INTINH
      COMMON/INTENS/VERTIN(51),HOREN(50)
      COMMON/INHIB/M(51),MEN(51,21),RMXZ(52,52)
      COMMON/RESIST/AP,BP,CP
      REAL M,MEN
C
C  COMPUTES THE NEW MAP OF INHIBITOR FRACTION
C  ACCORDING TO THE INTENSITY MAP.
C
      DO 1 I=2,51
      M(I)=M(I)*EXP(-VERTIN(I)*CP)
    1 CONTINUE
      RETURN
      END
C
C
C
      SUBROUTINE PASMAT(RDX2,RDX1,MAT)
      COMPLEX RDX1,RDX2,MAT(2,2)
C
C  COMPUTES THE MATRIX WHEN THE BOUNDARY 2/1 IS CROSSED TOWARDS 1
C
      MAT(1,1)=(1+RDX2/RDX1)/2
      MAT(2,2)=MAT(1,1)
      MAT(1,2)=(1-RDX2/RDX1)/2
      MAT(2,1)=MAT(1,2)
      RETURN
      END
C
C
C
      SUBROUTINE MULMAT(A,B,C)
      COMPLEX A(2,2),B(2,2),C(2,2),T(2,2)
C
C  PRODUCT A*B, RESULT IN C
C
      DO 1 I=1,2
      DO 1 J=1,2
      T(I,J)=(0.,0.)
      DO 1 K=1,2
      T(I,J)=T(I,J)+A(I,K)*B(K,J)
    1 CONTINUE
      DO 2 I=1,2
      DO 2 J=1,2
      C(I,J)=T(I,J)
    2 CONTINUE
      RETURN
      END
C
C
C
      SUBROUTINE TRAMAT(RDX,MAT)
      COMPLEX RDX,MAT(2,2)
      COMMON/SIMUL/DELTZ,DOSDEC,DELTX
      COMMON/CSTES/WAVEL,PI,RNO,THETA
C
C  COMPUTES MATRIX AS YOU MOVE FROM THE BOTTOM TO
C  THE TOP OF ONE OF THE PHOTORESIST LAYERS.
C
      MAT(1,1)=CEXP((0.,1.)*2*PI/WAVEL*RDX*DELTZ)
      MAT(2,2)=1./MAT(1,1)
      MAT(1,2)=(0.,0.)
      MAT(2,1)=MAT(1,2)
      RETURN
      END
```

```
C
C
C
      COMPLEX FUNCTION STHA(RINDX)
      COMPLEX RINDX
      COMMON/CSTES/WAVEL,PI,RNO,THETA
      STHA=RNO*SIN(THETA)/RINDX
      RETURN
      END
C
C
C
      COMPLEX FUNCTION CTHA(RINDX)
      COMPLEX RINDX,STHA
      CTHA=CSQRT((1.0,0.0)-STHA(RINDX)**2)
      RETURN
      END
C
C
C
      COMPLEX FUNCTION EFIDX(RINDX)
      COMPLEX RINDX,CTHA
      EFIDX=RINDX*CTHA(RINDX)
      RETURN
      END
C
      SUBROUTINE INPUT1
      COMMON/FLAG/IFLAG(6)
      COMMON/INDEX/RINDX(4)
      COMMON/THICKN/THICK(4)
      COMMON/RESIST/AP,BP,CP
      COMMON/CSTES/WAVEL,PI,RNO,THETA
      COMMON/EXPOS/EXPINT,EXPTIM,EXPOS(21)
      COMMON/SIMUL/DELTZ,DOSDEC,DELTX
      COMPLEX RINDX
C
C INPUT ROUTINE, INPUT DATAS ACCORDING TO IFLAG AS FOLLOWS
C IFLAG(1)=1 INPUT WAVELENGTH AND REFRACTIVE INDEX
C IFLAG(2)=1    INPUT RESIST BLEACHING CONSTANTS A,B,C
C IFLAG(3)=1    INPUT ANGLE OF INCIDENCE
C IFLAG(4)=1    INPUT THICKNESS(3)
C IFLAG(5)=1    INPUT THICKNESS(2)
C IFLAG(6)=1    INPUT EXPOSURE INTENSITY AND TIME AS WELL AS
C DOSE DECREMENT ON WHICH DEPENDS THE ACCURACY OF WEN( , ).
C
      IF (IFLAG(1).EQ.0) GOTO 10
      DO 1 I=1,4
      WRITE(2,*)'RINDX',I
      READ(1,*)RR,RI
      RINDX(I)=CMPLX(RR,-RI)
    1 CONTINUE
      RNO=REAL(RINDX(1))
      WRITE(2,*)'WAVELENGTH'
      READ(1,*)WAVEL
   10 IF (IFLAG(2).EQ.0) GOTO 20
      WRITE(2,*)'A,B,C'
      READ(1,*)AP,BP,CP
   20 IF (IFLAG(3).EQ.0) GOTO 30
      WRITE(2,*)'INCIDENCE'
      READ(1,*)THETAD
      THETA=THETAD*PI/180.
   30 IF (IFLAG(4).EQ.0) GOTO 40
      WRITE(2,*)'THICK 3'
      READ(1,*)THICK(3)
   40 IF (IFLAG(5).EQ.0) GOTO 50
      WRITE(2,*) 'THICK 2'
      READ(1,*) THICK(2)
   50 IF (IFLAG(6).EQ.0) GOTO 60
      WRITE(2,*)'EXP INTENS'
      READ(1,*)EXPINT
      WRITE(2,*)'EXP TIME'
      READ(1,*)EXPTIM
      WRITE(2,*)'DOSE DECREMENT'
      READ(1,*) DOSDEC
   60 RETURN
      END
```

```
C
C
C
      SUBROUTINE INPUT3
      COMMON/FLAG/IFLAG(6)
      COMMON/INDEX/RINDX(4)
      COMMON/THICKN/THICK(4)
      COMMON/RESIST/AP,BP,CP
      COMMON/CSTES/WAVEL,PI,RNO,THETA
      COMMON/EXPOS/EXPINT,EXPTIM,EXPOS(21)
      COMMON/SIMUL/DELTZ,DOSDEC,DELTX
      COMPLEX RINDX
C
C INPUT ROUTINE, INPUT DATAS ACCORDING TO IFLAG AS FOLLOWS
C IFLAG(1)=1 INPUT WAVELENGTH AND REFRACTIVE INDEX
C IFLAG(2)=1   INPUT RESIST BLEACHING CONSTANTS A,B,C
C IFLAG(3)=1   INPUT ANGLE OF INCIDENCE
C IFLAG(4)=1   INPUT THICKNESS(3)
C IFLAG(5)=1   INPUT THICKNESS(2)
C IFLAG(6)=1   INPUT EXPOSURE INTENSITY AND TIME AS WELL AS
C DOSE DECREMENT ON WHICH DEPENDS THE ACCURACY OF MEN( , ).
C
      IF (IFLAG(1).EQ.0) GOTO 10
      DO 1 I=1,4
      READ(3,*)RR,RI
      RINDX(I)=CMPLX(RR,-RI)
      WRITE(4,*)'RINDX',I,RINDX(I)
    1 CONTINUE
      RNO=REAL(RINDX(1))
      READ(3,*)WAVEL
      WRITE(4,*)'WAVELENGTH',WAVEL
   10 IF (IFLAG(2).EQ.0) GOTO 20
      READ(3,*)AP,BP,CP
      WRITE(4,*)'A,B,C',AP,BP,CP
   20 IF (IFLAG(3).EQ.0) GOTO 30
      READ(3,*)THETAD
      WRITE(4,*)'INCIDENCE',THETAD
      THETA=THETAD*PI/180.
   30 IF (IFLAG(4).EQ.0) GOTO 40
      READ(3,*)THICK(3)
      WRITE(4,*)'THICK 3',THICK(3)
   40 IF (IFLAG(5).EQ.0) GOTO 50
      READ(3,*) THICK(2)
      WRITE(4,*) 'THICK 2',THICK(2)
   50 IF (IFLAG(6).EQ.0) GOTO 60
      READ(3,*)EXPINT
      WRITE(4,*)'EXP INTENS',EXPINT
      READ(3,*)EXPTIM
      WRITE(4,*)'EXP TIME',EXPTIM
      READ(3,*) DOSDEC
      WRITE(4,*)'DOSE DECREMENT',DOSDEC
   60 RETURN
      END
C
C
C
```

REFERENCES

Ref.1 : Zh.I.ALFEROV, E.L.PORTNOY
"AlGaAs heterostructures in integrated optics."
Japan. Journ. Appl. Phys., Vol.16(1977), Suppl.16-1, p.289-296

Ref.2 : I.HAYASHI
"OEIC: Its concept and prospects."
IOOC TOKYO 1983 (28B2-4)

Ref.3 : A.YARIV, S.MARGALIT
"Monolithic optoelectronic integration in III-V semiconductors."
IOOC TOKYO 1983 (28B4-1)

Ref.4 : RICHARD SHUBERT
"Theory of optical waveguide distributed lasers with nonuniform gain and coupling."
Journ. of Appl. Phys.Vol.45, n°1, Jan.1974, p.209

Ref.5 : H.KOGELNIK, C.V.SHANK
"Stimulated emission in a periodic structure."
Applied Phys. letters Vol.18, n°4, Feb.1971, p.152

Ref.6 : SHYH WANG
"Proposal of periodic layered waveguide structures for distributed lasers."
Journ. of Appl. Phys.Vol.44, n°2, Feb.1973, p.767

Ref.7 : SHYH WANG
"Principles of distributed feedback and distributed Bragg reflector lasers."
IEEE Journ. Quant. Elect., Vol.QE10, n°4, Apr.1974, p.413

Ref.8 : H.OKUDA, J.KINOSHITA, Y.UEMATSU
"Monolithically integrated GaInAsP/InP DFB lasers."
IOOC TOKYO 1983 (28B1-4)

Ref.9 : T.INOGUCHI, S.YANO, T.HIJIKATA, T.WADA
"Visible semiconductor lasers."
IOOC TOKYO 1983 (27B2-2)

Ref.10 : L.D.WESTBROOK, A.W.NELSON, C.DIX
"High quality InP surface corrugation for 1.55 micron InGaAsP DFB lasers fabricated using electron beam lithography."
Electronics letters, Vol.18, n°20, Sept.1982, p.863

Ref.11 : L.D.WESTBROOK, A.W.NELSON, P.J.FIDDYMENT
"New diffraction grating profiles in InP for DFB lasers and integrated optics."
Electronics letters, Vol.19, n°25/26, Dec.1983, p.1076

Ref.12 : H.NISHIHARA, T.SUHARA
"Applications of electron beam written gratings to special IC."
IOOC TOKYO 1983 (29A1-5)

Ref.13 : DIETRICH MARCUSE
"Mode conversion caused by surface imperfections of a dielectric slab waveguide."
Bell Syst. Technical Journ., Dec.1969, p.3187

Ref.14 : P.K.TIEN
"Integrated optics and new wave phenomena in optical waveguides."
Rev. of Modern Phys., Vol.49, n°2, Apr.1977, p.361

Ref.15 : M.L.DAKSS, L.KUHN, P.F.HEIDRICH & B.A.SCOTT
"Grating coupler for efficient excitation of optical guided waves in thin films."
Applied Phys. letters Vol.16, n°12, Jun.1970, p.523

Ref.16 : J.H.HARRIS, R.K.WINN, D.G.DALGOUTTE
"Theory and design of periodic couplers."
Appl. Optics Vol.11, n°10, Oct.1972, p.2234

Ref.17 : K.OGAWA, W.S.C CHANG, B.L.SOPORI, F.J.ROSENBAUM
"A theoretical analysis of etched grating couplers for integrated optics."
IEEE Journ. Quant. Elect., Vol.QE9, n°1, Jan.1973, p.29

Ref.18 : D.G.DALGOUTTE, C.D.W.WILKINSON
"Thin grating couplers for integrated optics: an experimental and theoretical study."
Appl. Optics Vol.14, n°12, Dec.1975, p.2983

Ref.19 : H.KOGELNIK, C.V.SHANK
"Coupled wave theory of distributed feddback lasers."
Journ. of Appl. Phys. Vol.43, n°5, May 1972, p.2327

Ref.20 : M.NEVIERE, R.PETIT, M.CADILHAC
"About the theory of optical waveguide systems."
Optics communications, n°8, 1973, p.113

Ref.21 : YOSHIHISHA YAMAMOTO, T.KAMIYA, H.YANAI
"Improved coupled mode analysis of corrugated waveguides and lasers."
IEEE Journ. Quant. Elect., Vol.QE 14, n°4, Apr.1978, p.245

Ref.22 : M.NEVIERE, P.VINCENT, R.PETIT, M.CADILHAC
"Systematic study of resonances of holographic thin couplers."
Optics communications, Vol.9, n°1, sept.1973, p.48

Ref.23 : M.NEVIERE
"Determination of the computing coefficient of a holographic thin film coupler."
Optics communications Vol.9, n°3, Nov.1973, p.240

Ref.24 : T.TAMIR, H.C.WANG, A.A.OLINER
"Wave propagation in sinusoidally stratified dielectric media."
IEEE Trans. on Micro. Theo. Tech., May 1964, p.323

Ref.25 : RUEY-SHI-CHU, THEODOR TAMIR
"Guided wave theory of light diffraction by acoustic microwaves."
IEEE Trans. on Micro. Theo. Tech.Vol.MTT17,n°11,Nov.69, p.1002-20

Ref.26 : LAWRENCE R.LEWIS, ALEXANDER HESSEL
"Propagation characteristics of periodic arrays of dielectric slabs."
IEEE Trans. on Micro. Theo. Tech.Vol.MTT19,n°3,Mar.71, p.276

Ref.27 : CHARLES ELACHI
"Waves in active and passive periodic structures: a review."
Proceed. of the IEEE, Vol.64, n°12, Dec.1976, p.1666

Ref.28 : HERWIG KOGELNIK
"Coupled wave theory for thick hologram grating."
Bell Syst. Technical Journ. Vol.48, n°9, Nov.1969, p.2909

Ref.29 : AMNON YARIV
"Coupled mode theory for guided wave optics."
IEEE Journ. Quant. Elect., Vol.QE9, n°9, Sep.1973, p.919

Ref.30 : A.YARIV, A.GOVER
"Equivalence of the coupled mode and Floquet-Bloch formalisms in periodic optical waveguides."
Applied Phys. letters Vol.26, n°9, May 1975, p.537

Ref.31 : D.L.JAGGARD, C.ELACHI
"Floquet and coupled waves analysis of higher order Bragg coupling in a periodic medium."
Journ. Opt. Soc. Amer.Vol66, n°7, Jul.1976, p.674

Ref.32 : W.STREIFER, D.R.SCIFRES, R.D.BURNHAM
"Coupling coefficients for distributed feedback single and double heterostructure diode lasers."

Ref.33 : W.STREIFER, D.R.SCIFRES, R.D.BURNHAM
"Analysis of grating coupled radiation in GaAs:GaAlAs lasers and waveguides."
IEEE Journ. Quant. Elect., Vol.QE12, n°7, Jul.1976, p.422

Ref.34 : W.STREIFER, D.R.SCIFRES, R.D.BURNHAM
"Analysis of grating coupled radiation in GaAs:GaAlAs lasers and waveguides: II Blazing effects.
IEEE Journ. Quant. Elect., Vol.QE12, n°8, Aug.1976, p.494

Ref.35 : COSSLET & NIXON
"X-ray microscopy."
ACADEMIC PRESS 1960, p.372-402

Ref.36 : B.L.HENKE, R.L.ELGIN
"X-ray absorption tables for the 2 to 200 angstrom region."
Preprint

Ref.37 : B.L.HENKE, E.S.EBISU
"Low energy X-ray and electron absorption within solids."
Advan. X-ray Anal.17, 150 et seq, 1973, Plenum Press NY

Ref.38 : KURT F.J.HEINRICH
"X-ray absorption uncertainty."
SYMPOSIUM on ELECTRON MICROPROBE Washington DC, Oct.64, p.296-377

Ref.39 : EUGENE McGUIRE
"Photo-ionisation cross-sections of the elements Helium to Neon."
Physical Review, Vol.175, n°1, Nov.1968, p.20

Ref.40 : ROBERT STERN & FRANCESCO PARESCE
"Mass absorption coefficients of parylene N at sof X-ray and vacuum ultraviolet wavelengths."
Journ. Opt. Soc. Amer., Vol.65, n°12, Dec.1975, p.1514

Ref.41 : H.ARITOME, S.MATSUI, K.MORIWAKI, S.NAMBA
"X-ray lithography by synchrotron radiation of the SOR-RING storage ring."
Journ. Vac. Sci. Tech. Vol.16, n°6, Nov/Dec 1979, p.1939

Ref.42 : E.SPILLER, R.FEDER, J.TOPALIAN, W.GUDAT, D.EASTMAN
"X-ray lithography with synchrotron radiation."
Electron & ion beam Sci.& Tech. 7th intern. confer. 1976

Ref.43 : E.SPILLER, D.E.EASTMAN, R.FEDER, W.D.GROBMAN, W.GUDAT, J.TOPALIAN
"Application of synchrotron radiation to X-ray lithography."
Journ. of Appl. Phys.Vol.47, n°12, Dec.1976, p.5450

Ref.44 : R.A.McCORKLE, H.J.VOLLMER
"Physical properties of an electron beam sliding-spark device."
Rev. Sci. Instrum., Vol.48, n°8, Aug.1977, p.1055

Ref.45 : C.M.DOZIER, P.G.BURKHALTER, B.M.KLEIN, D.J.NAGEL, R.R.WHITLOCK
"X-ray emission from laser produced plasmas."
NAVAL RESEARCH LABORATORY, WASHINGTON D.C. 20375

Ref.46 : DAVID J.JOHNSON
"Study of the X-ray production mechanism of a dense plasma focus."
Journ. of Appl. Phys.Vol.45, n°3, Mar.1974, p.1147

Ref.47 : C.E.DICK, A.C.LUCAS, J.M.MOTZ, R.C.PLACIOUS, J.H.SPARROW
"Large angle L X-ray production by electrons."
Journ. of Appl. Phys.Vol.44, n°2, Feb.1973, p.815

Ref.48 : L.H.FONG, S.G.TOMLIN
"Absolute intensities of some L & M characteristic X-ray from solid targets."
Austr. Journ. Phys. n°23, 1970, p.17-21

Ref.49 : M.GREEN, V.E.COSSLETT
"Measurements of K, L, M shell X-ray production efficiencies."
Brit. Journ. Appl. Phys.Vol.1, Ser.2, 1968, p.425

Ref.50 : N.A.DYSON
"The continuous X-ray spectrum from electron opaque targets."
CAVENDISH LABORATORIES, CAMBRIDGE Dec.1958

Ref.51 : J.R.MALDONADO, M.E.POULSEN, T.E.SAUNDERS, F.VRATNY, A.ZACHARIAS
"X-ray lithography source using a stationary solid Pd target."
Journ. Vac. Sci. Techn.Vol.16, n°6, Nov/Dec 1979, p.1942

Ref.52 : D.B.WITTRY, R.S.MESSENGER, T.S.RAO-SAHIB, A.B.JONES, J.P.REEKSTIN
"Novel "heat-pipe" rotating anode for X-ray lithography."
Journ. Vac. Sci. Tech. Vol.16, n°6, Nov/Dec 1979, p.1946

Ref.53 : WARREN D.GROBMAN
"Synchrotron radiation X-ray lithography."
Preprint

Ref.54 : ANDREW NEUREUTHER
"Microlithography with soft X-rays."
Synchrotron radiation research, Ed. Winnick H. & Doniach S.
Plenum NY 1980, p.223-268

Ref.55 : K.SUZUKI, J.MATSUI
"SiN membrane masks for X-ray lithography."
Journ. Vac. Sci. Tech. Vol.20, n°2, Feb.1982, p.191

Ref.56 : P.PARRENS, E.TABOURET, M.C.TACUSSEL
"Preparation of X-ray lithography masks with 0.1 micron structures."
Journ. Vac. Sci. Tech. Vol.16, n°6, Nov/Dec 1979, p.1965

Ref.57 : D.C.FLANDERS, H.I.SMITH
"Polyimide membrane X-ray lithography masks-Fabrication and distortion measurements."
Journ. Vac. Sci. Tech. Vol.15, n°3, May/Jun 1978, p.995

Ref.58 : K.SUZUKI, J.MATSUI, T.KADOKA, T.ONO
"Preparation of X-ray lithography masks with large area sandwich structure membrane."
Japan. Journ. Appl. Phys. Vol.17, n°8, 1978, p.1447

Ref.59 : C.J.SCHMIDT, P.I.LENZO, E.G.SPENCER
"Preparation of thin windows in silicon masks for X-ray lithography."
Journ. of Appl. Phys.Vol.46, n°9, Sept.1975, p.4080

Ref.60 : WILLIAM STUART MACKIE
"Techniques and applications of very high resolution electron beam lithography."
Ph.D. THESIS at GLASGOW UNIVERSITY (1984).

Ref.61 : R.FEDER, E.SPILLER, J.TOPALIAN, M.HATZAKIS
"High resolution X-ray lithography with Carbon K_α radiation."
Electron & ion beam Sci. & Tech. 7th inter. confer. 1976

Ref.62 : D.A.NELSON, Jr & A. L.RUOFF
"Diamond: an efficient source of soft X-rays for high resolution X-ray lithography."
Journ. of Appl. Phys.Vol.49, n°11, Nov.1978, p.5365

Ref.63 : E.SPILLER, R.FEDER, J.TOPALIAN, D.EASTMAN, W.GUDAT, D.SAYRE
"X-ray microscopy of biological objects with carbon K_α and with synchrotron radiation."
SCIENCE, 19 March 1976, Vol.191, p.1172

Ref.64 : E.HUNDT, P.TISCHER
"Influence of photoelectrons on the exposure of resists by X-rays."
Journ. Vac. Sci. Tech. Vol.15, n°3, May/Jun 1978, p.1009

Ref.65 : JAMES S.GREENEICH
"X-ray lithography:
Part I : Design criteria for optimising resist energy absorption.
Part II: Pattern replication with polymer masks."
IEEE Trans. on Electron. Dev.Vol.ED22, n°7, Jul.1975, p.434

Ref.66 : "Handbook of chemistry and physics"
CRC PRESS

Ref.67 : N.N.EFREMOW, N.P.ECONOMOU, K.BEZIJIAN, S.S.DIANA, H.I.SMITH
"A simple technique for modifying the profile of resist exposed by holographic lithography."
Journ. Vac. Sci. Tech. Vol.19, n°4, Nov/Dec 1981, p.1234

Ref.68 : Y.ABE, K.KISHINO, Y.SUEMATSU, S.ARAI
"GaInAsP/InP integrated laser with butt-jointed built-in distributed Bragg-reflection waveguide."
Electronics letters, Vol.17, n°25, Dec.1981

Ref.69 : T.TANBUN-EK, S.ARAI, F.KOYAMA, K.KISHINO, S.YOSHIZAWA, T.WATANABE
"Low threshold current cw operation of GaInAsP/InP buried heterostructure distributed Bragg-reflector integrated twin guide laser emitting at 1.5-1.6 micron."
Electronics letters, Vol.17, n°25, Dec.1981, p.967

Ref.70 : K.UTAKA, S.AKIBA, K.SAKAI, Y.MATSUSHIMA
"Room-temperature cw operation of distributed feedback buried heterostructure InGaAsP/InP lasers emitting at 1.57 micron."
Electronics letters, Vol.17, n°25, Dec.1981, p.961

Ref.71 : K.KOBAYASHI, K.UTAKA, Y.ABE, Y.SUEMATSU
"Cw operation of 1.5-1.6 micron wavelength GaInAsP/InP buried heterostructure integrated twin guide laser with distributed Bragg reflector."
Electronics letters, Vol.17, n°11, May.1981, p.366

Ref.72 : F.KOYAMA, A.ARAI, Y.SUEMATSU, K.KISHINO
"Dynamic spectral width of rapidly modulated 1.58 micron GaInAsP/InP buried heterostructure distributed Bragg reflector integrated twin guide lasers."
Electronics letters, Vol.17, n°25, Dec.1981, p.938

Ref.73 : K.UTAKA, K.KOBAYASHI, F.KOYAMA, Y.ABE, Y.SUEMATSU
"Single wavelength operation of 1.53 micron GaInAsP/InP buried heterostructure integrated twin guide laser with distributed Bragg reflector under direct modulation up to 1 Ghz."
Electronics letters, Vol.17, n°11, May.1981, p.368

Ref.74 : W.STREIFER, R.D.BURNHAM, D.R.SCIFRES
"Current status of (GaAl)As diode lasers."
SPIE Vol.269, Integrated optics (1981), p.2

Ref.75 : K.AIKI, M.NAKAMURA, J.UMEDA, A.YARIV, A.KATZIR, H.W.YEN
"GaAS-GaAlAs distributed feedback diode lasers with separate optical and carrier confinement."
Applied Phys. letters, Vol.27, n°3, Aug.1975, p.145

Ref.76 : H.C.CASEY, Jr.S.SOMEKH, M.ILEGEMS
"Room-temperature operation of a low threshold separate confinement heterostructure injection laser with distributed feedback."
Applied Phys. letters, Vol.27, n°3, Aug.1975, p.142

Ref.77 : F.K.REINHART, R.A.LOGAN
"GaAs-$Al_xGa_{1-x}As$ injection lasers with distributed Bragg reflectors."
Applied Phys. letters, Vol.27, n°1, Jul.1975, p.45

Ref.78 : S.AKIBA, K.UTAKA, K.SAKAI, Y.MATSUSHIMA
"Low-threshold current distributed feedback InGaAsP/InP cw lasers."
Electronics letters, Vol.18, n°2, Jan.1982, p.77

Ref.79 : Y.ABE, K.KISHINO, T.TANBUN-EK, S.ARAI, F.KOYAMA, K.MATSUMOTO, T.WATANABE, Y.SUEMATSU
"Room temperature cw operation of 1.6 micron GaInAsP/InP buried heterostructure integrated laser with butt-jointed built-in distributed Bragg reflection waveguide."
Electronics letters, Vol.18, n°10, May.1982, p.410

Ref.80 : I.SUEMUNE, M.KOHNO, M.YAMANISHI
"Room-temperature operation of a transverse distributed feedback cavity laser."
Electronics letters, Vol.18, n°17, Aug.1982, p.745

Ref.81 : Y.UEMATSU, H.OKUDA, J.KINOSHITA
"Room-temperature cw operation of 1.3 micron distributed feedback GaInAsP/InP lasers."
Electronics letters, Vol.18, n°20, Sept.1982, p.857

Ref.82 : Y.IMAYA, T.MATSUOKA, Y.NAKANO, Y.SUZUKI, K.KUROIWA, T.IKEGAMI
"New 1.5 micron wavelength GaInAsP/InP distributed feedback laser."
Electronics letters, Vol.18, n°23, Nov.1982, p.1006

Ref.83 : H.OKUDA, J.KINOSHITA, Y.HIRAYAMA, Y.UEMATSU
"Longitudinal mode characteristics for 1.3 micron GaInAsP/InP DFB lasers just below the threshold current."
Electronics letters, Vol.19, n°10, May.1983, p.362

Ref.84 : H.ASAHI, Y.KAWAMURA, Y.NOGUCHI, T.MATSUOKA, H.NAGAI
"Hybrid LPE/MBE grown InGaAsP/InP DFB lasers."
Electronics letters, Vol.19, n°14, Jul.1983, p.507

Ref.85 : Y.TOHMORI, Y.SUEMATSU, H.TSUSHIMA, S.ARAI
"Wavelength tuning of GaInAsP/InP integrated laser with butt-jointed built-in distributed Bragg reflector."
Electronics letters, Vol.19, n°17, Aug.1983, p.656

Ref.86 : H.OKUDA, Y.HIRAYAMA, J.KINOSHITA, H.FURUYAMA, Y.UEMATSU
"High quality 1.3 micron GaInAsP/InP BH-DFB lasers with first order grating."
Electronics letters, Vol.19, n°22, Oct.1983, p.941

Ref.87 : K.UOMI, M.YAMANISHI, I.SUEMUNE
"Two-dimensionally collimated output beam from GaAlAs diode lasers with two-dimensional distributed Bragg reflectors."
IOOC TOKYO 1983 (29A5-5)

Ref.88 : Y.ITAYA, T.MATSUOKA, K.KUROIWA, T.IKEGAMI
"Longitudinal mode spectra of 1.5 micron GaInAsP/InP DFB lasers."
IOOC TOKYO 1983 (28B1-1)

Ref.89 : Y.TOHMORI, Y.SUEMATSU, H.TSUSHIMA
"Wavelength tuning of GaInAsP/InP integrated laser with butt jointed built-in distributed Bragg-reflector."
IOOC TOKYO 1983 (29B5-3)

Ref.90 : K.TADA, Y.NAKANO, A.USHIROKAWA
"Proposal of a distributed feedback laser with non-uniform stripe width for complete single-mode oscillation."
Electronics letters, Vol.20, n°2, Jan.1984, p.82

Ref.91 : K.SEKARTEDJO, N.EDA, K.FURUYA, Y.SUEMATSU, F.KOYAMA, T.TANBUN-EK
"1.5 micron phase-shifted DFB lasers for single-mode operation."
Electronics letters, Vol.20, n°2, Jan.1984, p.80

Ref.92 : M.YAMAGUCHI, M.KITAMURA, I.MITO, S.MURATA, K.KOBAYASHI
"Highly efficient single-longitudinal mode operation od antireflection coated 1.3 micron DFB DC PBH LD."
Electronics letters, Vol.20, n°6, Mar.1984, p.233

Ref.93 : L.D.WESTBROOK, A.W.NELSON, P.J.FIDDYMENT, J.S.EVANS
"Continuous wave operation of 1.5 micron distributed feedback ridge waveguide lasers."
Electronics letters, Vol.20, n°6, Mar.1984, p.225

Ref.94 : F.KOYAMA, Y.SUEMATSU, K.KOJIMA, K.FURUYA
"1.5 micron phase adjusted active distributed reflector laser for complete dynamic single-mode operation."
Electronics letters, Vol.20, n°10, May.1984, p.391

Ref.95 : P.BESOMI, R.B.WILSON, R.L.BROWN, N.K.DUTTA, P.D.WRIGHT, R.J.NELSON
"High temperature operation of 1.55 micron InGaAsP double-channel buried heterostructure lasers grown by LPE."
Electronics letters, Vol.20, n°10, May.1984, p.417

Ref.96 : D.B.ANDERSON, R.R.AUGUST, J.E.COKER
"Distributed feedback double heterostructure GaAs injection laser with fundamental grating."
Appl. Optics, Vol.13, n°12, Dec. 1974, p.2742

Ref.97 : A.W.NELSON, L.D.WESTBROOK, P.J.FIDDYMENT
"Design and fabrication of 1.5 micron ridge waveguide distributed feedback lasers."
IEE PROCEEDINGS, Vol.132, PtJ, n°1, Feb.1985, p.12

Ref.98 : K.UTAKA, S.AKIBA, K.SAKAI, Y.MATSUSHIMA
"Analysis of quarter-wave shifted DFB laser."
Electronics letters, Vol.20, n°8, Apr.1984, p.326

Ref.99 : K.SEKARTEDJO, N.EDA, K.FURUYA, Y.SUEMATSU, F.KOYAMA, T.TANBUN-EK
"1.5 micron phase-shifted DFB lasers for single-mode operation."
Electronics letters, Vol.20, n°2, Jan.1984, p.80

Ref.100 : ALFREDO YI-YAN
"Frequency selective grating filters for integrated optics."
Ph.D. THESIS at GLASGOW UNIVERSITY (1978).

Ref.101 : DAVID G.DALGOUTTE
"Periodic couplers for the excitation of optical guided waves in thin films."
Ph.D. THESIS at GLASGOW UNIVERSITY (1973).

Ref.102 : EDWIN Y.B.PUN
"Thin film Bragg deflection gratings for integrated optics."
Ph.D. THESIS at GLASGOW UNIVERSITY (1983).

Ref.103 : R.CAPONI, C.DEBERNARDI
"A precise versatile set-up for holographic grating generation."
CSELT Rapporti tecnici, Vol.XI, n°6, Dec.1983, p.413

Ref.104 : ANDRZEJ MALAG
"Simple interference method of diffraction grating generation for integrated optics by the use of a Fresnel mirror."
Optics communications, Vol.32, n°1, Jan.1980, p.54

Ref.105 : C.V.SHANK, R.V.SCHMIDT
"Optical technique for producing 0.1 micron periodic surface structures."
Applied Phys. letters, Vol.23, n°3, Aug.1973, p.154

Ref.106 : WON-TIEN TSANG, SHYH WANG
"Simultaneous exposure and development technique for making gratings on positive photoresist."
Applied Phys. letters, Vol.24, n°4, Feb.1974, p.196

Ref.107 : L.F.JOHNSON, G.W.KAMMLOTT, K.A.INGERSOLL
"Generation of periodic surface corrugations."
Appl. Optics, Vol.17, n°8, Apr.1978, p.1165

Ref.108 : AMNON YARIV
"Introduction to optical electronics."
2nd edition, Holt Rinehart Winston editors, 1976

Ref.109 : DIETRICH MARCUSE
"Light transmission optics."
VAN NOSTRAND REINHOLD COMPANY 1972

Ref.110 : SPECTRA-PHYSICS argon ion laser instruction manual

Ref.111 : C.J.TRANTER
"Bessel functions with some physical applications."
The ENGLISH UNIVERSITIES PRESS LTD. 1968

Ref.112 : I.N.SNEDDON
"Special functions of mathematical physics and chemistry."
LONGMAN 1980

Ref.113 : YUDELL L.L.LUKE
"Integrals of Bessel functions."
McGRAW-HILL BOOK COMPANY, INC 1962

Ref.114 : MAX BORN AND EMIL WOLF
"Electromagnetic theory of propagation, interference and diffraction of light."
PERGAMON PRESS 1964

Ref.115 : PETER H.BERNING
"Theory and calculations of optical thin films."
Physics of thin films, Ed. GEORG HASS, Vol.1, 1963
ACADEMIC PRESS, p.69-121

Ref.116 : F.H.DILL, W.P.HORNBERGER, P.S.HAUGE, J.M.SHAW
"Characterisation of positive photoresist."
IEEE Trans. on Electron. Dev.Vol.ED22, n°7, Jul.1975, p.445-52

Ref.117 :"Simulation And Modelling of Profiles in Lithography and Etching. (S.A.M.P.L.E.)"
Electronics research laboratory
Dep^{t} of electrical engineering and computer science
University of California, BERKELEY CALIFORNIA 94720

Ref.118 : F.H.DILL, A.R.NEUREUTHER, J.A.TUTTLE, E.J.WALKER
"Modelling projection printing of positive photoresists."
IEEE Trans. on Electron. Dev.Vol.ED22, n°7, Jul.1975, p.456-64

Ref.119 : M.A.LIND, E.F.ZALEWSKI
"Silicon photodetector instabilities in the UV."
Appl. Optics, Voll5, n°6, Jun.1976, p.1377

Ref.120 : R.J.ARCHER
"Determination of the properties of films on silicon by the method of ellipsometry."
Journ. Opt. Soc. Amer., Vol.52, n°9, Sep.1962, p.970

Ref.121 : H.R.PHILIPP, E.A.TAFT
"Optical constants of silicon in the region 1 to 10 eV."
Physical review, Vol.120, n°1, Oct.1960, p.37-8.

Ref.122 : W.STUTIUS, W.STREIFER
"Silicon nitride films on silicon for optical waveguides."
Appl. Optics, Vol.16, n°12, Dec.1977, p.3218

Ref.123 : LESLIE HOLLAND
"Thin film electronics. The preparation and properties of components and circuit arrays."
CHAPMAN and HALL, LONDON, 1965

Ref.124 : E.KAPON, A.KATZIR
"Photoresist gratings on reflecting surfaces."
Journ. of Appl. Phys., Vol.53, n°3, march 1982, p.1387

Publication: R.H.M. DUMAS and Prof. P.J.R. LAYBOURN
"Computer simulation of holographic grating exposure"
IEE Proceedings, Vol.132, Pt.J, n°6, dec. 1985, p.331